

Spectral and magnetic properties of two-dimensional Dirac systems and thermal spin-charge coupling in electronic systems



Dissertation

zur Erlangung des Doktorgrades
der Naturwissenschaften (Dr. rer. nat.)
der Fakultät für Physik
der Universität Regensburg

vorgelegt von
Benedikt Scharf
aus Schwarzhofen
2012

Promotionsgesuch eingereicht am: 27. Juni 2012
Die Arbeit wurde angeleitet von: Prof. Dr. Jaroslav Fabian

Vorsitzender: Prof. Dr. Christoph Strunk
1. Gutachter: Prof. Dr. Jaroslav Fabian
2. Gutachter: Prof. Dr. Thomas Niehaus
weiterer Prüfer: Prof. Dr. Ingo Morgenstern

Contents

1. Introduction	1
2. Magnetic properties of HgTe quantum wells	3
2.1. Quantum spin Hall effect and HgTe quantum wells	3
2.1.1. The quantum spin Hall effect	3
2.1.2. HgTe quantum wells and effective model Hamiltonian	6
2.1.3. Model Hamiltonian in a perpendicular magnetic field	9
2.2. Magnetic edge states	10
2.2.1. Analytical solution	10
2.2.2. Numerical finite-difference solution	15
2.2.3. Comparison between the analytical and numerical solutions . .	16
2.2.4. Results	17
2.3. Magnetic oscillations	24
2.3.1. General formalism	24
2.3.2. Results	27
2.4. Magneto-optical conductivity	30
2.4.1. General formalism	30
2.4.2. Results	34
2.5. Conclusions	37
3. Optical conductivity of graphene	39
3.1. Graphene	39
3.2. Model	41
3.2.1. Hamiltonian and electron Green's function	41
3.2.2. Kubo formula for the optical conductivity	46
3.3. Results	48
3.4. Conclusions and outlook	54
4. Theory of thermal spin-charge coupling in electronic systems	57
4.1. Introduction	57

Contents

4.2. Spin-polarized transport in the presence of thermal fluctuations . . .	61
4.2.1. Spin-unpolarized transport equations	61
4.2.2. Spin-polarized transport equations	64
4.2.3. Spin-diffusion equation and its general solution	67
4.2.4. Contact properties	68
4.3. Ferromagnet placed in a thermal gradient	69
4.4. F/N junctions	72
4.4.1. F/N junctions placed in thermal gradients	72
4.4.2. Interplay between thermal gradients and simultaneous charge currents	77
4.4.3. Peltier effects in F/N junctions	79
4.5. F/N/F junctions	85
4.5.1. F/N/F junctions placed in thermal gradients	85
4.5.2. Peltier effects in F/N/F junctions	91
4.6. Conclusion	95
 5. Outlook	 97
 A. Finite-difference method	 99
 B. Landau levels	 103
 C. Ground-state magnetization	 105
 D. Magnetization: Simplified model	 107
 E. Current densities	 111
 Acknowledgments	 123

1. Introduction

The Dirac equation is often considered as one of the great triumphs of theoretical physics, combining quantum mechanics with special relativity. Not only did it explain the spin as a consequence of merging quantum mechanics and special relativity, but it also allowed one to predict the existence of positrons as antiparticles of electrons. As the equation at the center of quantum electrodynamics, the Dirac equation describes relativistic spin-1/2 particles and is one of the fundamental equations in particle physics.

During the last decade, however, the Dirac equation has also increasingly attracted the attention of solid-state physicists. There has, in particular, been a growing interest in the physics of solid-state systems whose low-energy excitations can be treated as Dirac fermions, that is, fermions described by the Dirac equation. Nowadays, the prime examples for such systems are graphene, whose band structure can be approximated by a two-dimensional (2D) Dirac-like Hamiltonian in the vicinity of the K and K' points [1, 2], and topological insulators, which possess edge states with a linear, one-dimensional (1D) spectrum in the case of 2D systems and surface states described by a single Dirac cone in the case of three-dimensional (3D) topological insulators [3, 4]. One of the main reasons for the enormous interest in these materials is that they offer the possibility to study quantum electrodynamical phenomena in solid-state systems. Meanwhile, condensed-matter systems are increasingly considered as promising alternatives to observe other phenomena commonly associated only with high-energy physics, with the appearance of Majorana fermions being the most notable recent example of this trend [5, 6].

Another topic of recent interest in solid-state physics is the field of spin caloritronics [7]. Whereas conventional spintronics [8, 9] is mainly about utilizing the coupling between the electron charge and spin, spin caloritronics focuses on the coupling between spin and heat. Since several spin caloritronic phenomena also exist at room temperature, there might be some technological applications of those effects, especially with respect to utilizing waste heat or offering new functionalities in devices [7]. In this thesis, we investigate several different topics related to the aforementioned fields. We study magnetic properties of 2D topological insulators and the optical conductivity of graphene. Another part of this thesis is devoted to a discussion of thermoelectric effects in electronic systems. The thesis itself, therefore, consists of three independent parts and is organized as follows: In Chap. 2, we discuss several properties of HgTe/CdTe-based quantum wells subject to perpendicular magnetic fields, namely magnetic edge states, the magnetization, and the magneto-optical

1. Introduction

conductivity. Continuing with the investigation of another optical response, we study the optical conductivity in graphene and the effect of electron-phonon coupling on it in Chap. 3. Finally, a phenomenological model in the spirit of the standard model of electrical spin injection to describe the electronic mechanism coupling charge, spin, and heat transport is formulated in Chap. 4 and employed to analyze several different geometries containing ferromagnetic and nonmagnetic regions.¹

¹Major parts of Secs. 2.1.1, 2.2, 2.3, and 2.5 are based on B. Scharf, A. Matos-Abiague, and J. Fabian, *Magnetic properties of HgTe quantum wells*, Phys. Rev. B 86, 075418 (2012), while Chap. 4 is based on B. Scharf, A. Matos-Abiague, I. Žutić, and J. Fabian, *Theory of thermal spin-charge coupling in electronic systems*, Phys. Rev. B 85, 085208 (2012).

2. Magnetic properties of HgTe quantum wells

2.1. Quantum spin Hall effect and HgTe quantum wells

2.1.1. The quantum spin Hall effect

In recent years, much attention has been devoted to the field of topological insulators, which are materials insulating in the bulk, but which possess dissipationless conducting states at their edge (2D topological insulators) or surface (3D topological insulators) [3, 4]. Since the introduction of the concept of 2D topological insulators—often referred to as quantum spin Hall (QSH) insulators—and their first prediction in graphene [10, 11], several other systems have been proposed theoretically to exhibit QSH states, such as inverted HgTe/CdTe quantum-well structures [12], GaAs under shear strain [13], 2D bismuth [14], or inverted InAs/GaSb/AlSb Type-II semiconductor quantum wells [15]. Experimentally, the QSH state has first been observed in inverted HgTe quantum wells [16, 17, 18, 19], where one can tune the band structure by fabricating quantum wells with different thicknesses.

Similarly to the quantum Hall (QH) state, which can be characterized by Chern numbers [20, 21], the QSH state can also be described by a topological invariant, in this case the Z_2 invariant [10]. This invariant describes whether one deals with a trivial insulator, that is, an insulator without edge states protected by time-reversal symmetry, or a QSH insulator. One of the most prominent features of QSH insulators is the existence of dissipationless helical edge states, that is, edge states whose spin orientation is determined by the direction of the electron momentum and are protected from backscattering [22, 23]. Thus, at a given edge, one can find a pair of counterpropagating, spin-polarized edge states (see Fig. 2.1), a fact whose experimental verification has only very recently been reported [19]. Since those counterpropagating, spin-polarized edge states are robust against time-reversal invariant perturbations such as scattering by nonmagnetic impurities (see Fig. 2.2), they are promising for applications within the field of spintronics [8, 9], the central theme of which is the generation and control of nonequilibrium electron spin in solids.

At the center of the QSH state are relativistic corrections, which can—if strong enough—lead to band inversion (see Fig. 2.3), that is, a situation where the normal

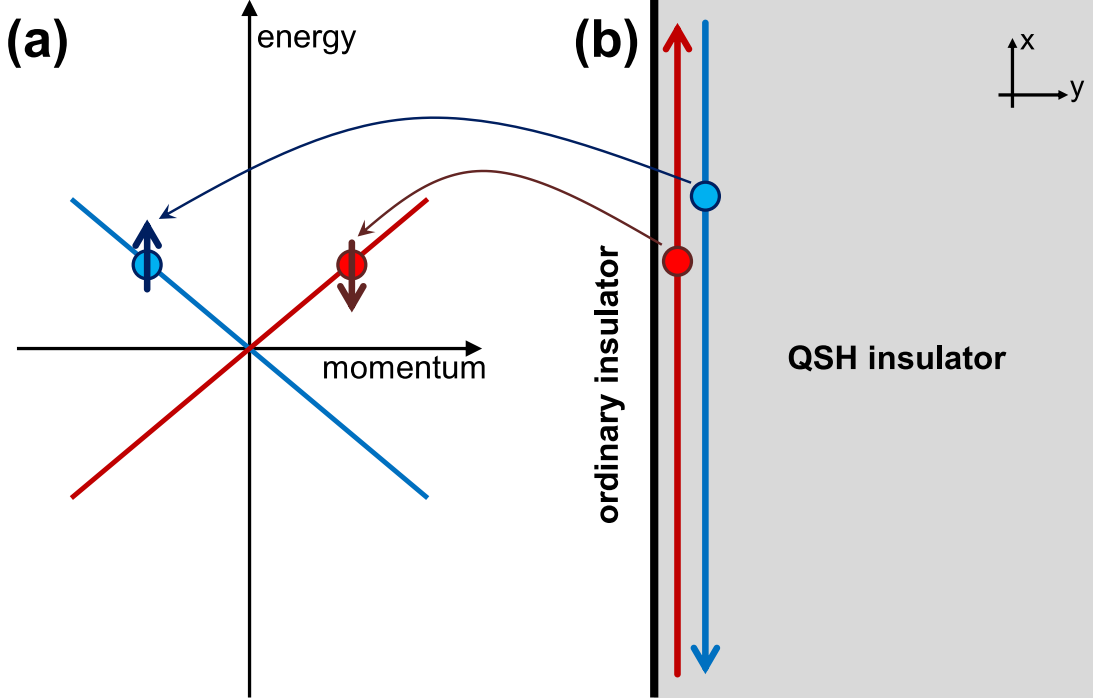


Figure 2.1.: (a) Energy spectrum and (b) schematic illustration of the QSH state [42]. At the boundary between an ordinary insulator and a QSH insulator, spin-polarized, counterpropagating edge states arise in the QSH insulator.

order of the conduction and valence bands is inverted [24, 25]. By fabricating HgTe quantum wells with a thickness larger than the critical thickness $d_c \approx 6.3$ nm, such an inverted band structure can be created in HgTe/CdTe quantum-well structures. In fact, materials with band inversion have been studied for some time [27] and another interesting prediction—different from the QSH state—has been that the combination of two materials with mutually inverted band structures can lead to the formation of interface states which, depending on the material parameters, can possess a linear 2D spectrum [28, 29].

Following the observation of the QSH state in HgTe-based quantum wells, much effort has been invested in the theoretical investigation of the properties of 2D topological insulators, their edge states, and possible applications. Examples include the extension of the low-energy Hamiltonian introduced in Ref. 12 to account for additional spin-orbit terms due to out-of-plane inversion breaking in HgTe quantum wells [30] as well as studies on how helical edge states and bulk states interact in 2D topological insulators [31]. The effect of magnetic fields on transport in inverted HgTe quantum wells has been treated in Refs. 32-34. Moreover, the effect of finite sizes on the QSH edge states in HgTe quantum wells has been investigated and it has been shown that for small widths the edge states of opposite sides in a finite system can overlap and

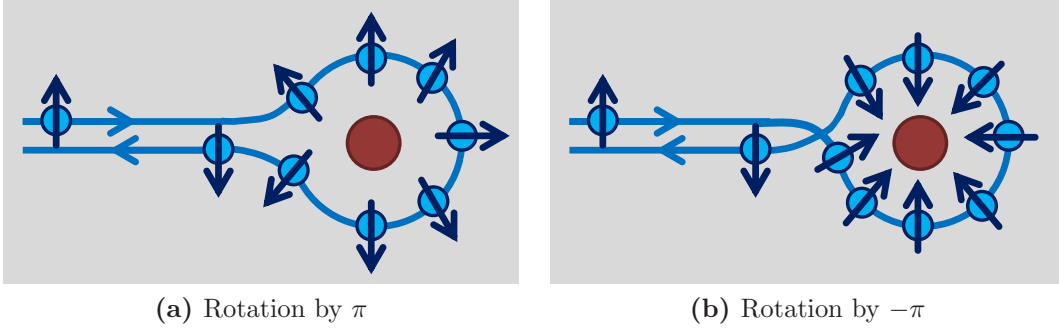


Figure 2.2.: Semiclassical picture of the suppression of backscattering in QSH insulators [4, 43]: When scattered by a nonmagnetic impurity, there are two possible paths allowed by time-reversal symmetry that an electron in the QSH state can take: It can (a) either go clockwise or (b) counterclockwise around the impurity, which means its spin rotates by π or $-\pi$, respectively. Consequently, the two paths differ by a rotation of the electron spin by 2π from each other. Since the wave functions of spin-1/2 particles just change their sign under rotation of their spin by 2π , the two paths interfere destructively, effectively suppressing any backscattering. Note that this picture holds true only if there is an odd number of QSH states at a given edge. Otherwise, there are additional paths an electron can take to flip its spin, which do not necessarily interfere destructively and backscattering is therefore not suppressed in this case.

produce a gap in the spectrum [38]. Based on this coupling of the wave functions from opposite edges, a spin transistor based on a constriction made of HgTe has been proposed [39]. Finite-size effects in topological insulators have not only been studied for HgTe, but also in three-dimensional topological insulators, in particular the crossover to QSH insulators in thin films [35, 36, 37].

Our purpose is to present a systematic study of the effect a perpendicular magnetic field has on the energy spectrum and magnetic edge states of HgTe/CdTe quantum wells (as described by the Hamiltonian introduced in Ref. 12) in the normal as well as in the inverted regime. In particular, we present an analytical solution for the magnetic edge states confined by a hard-wall potential in the spirit of Refs. 40, 41, where the problems of spin edge states and magnetic spin edge states in 2D electron gases with hard walls and spin-orbit coupling have been solved analytically. Complementary to this procedure, we also make use of a numerical scheme based on the method of finite differences. Furthermore, the magnetic properties of HgTe quantum wells are investigated within this model, again for both the normal and inverted regimes.

This chapter is organized as follows: Section 2.1.1 gives a short introduction and overview of the effective model used to describe HgTe/CdTe quantum wells. In Sec. 2.2, following the presentation of two methods to calculate the energy spectrum

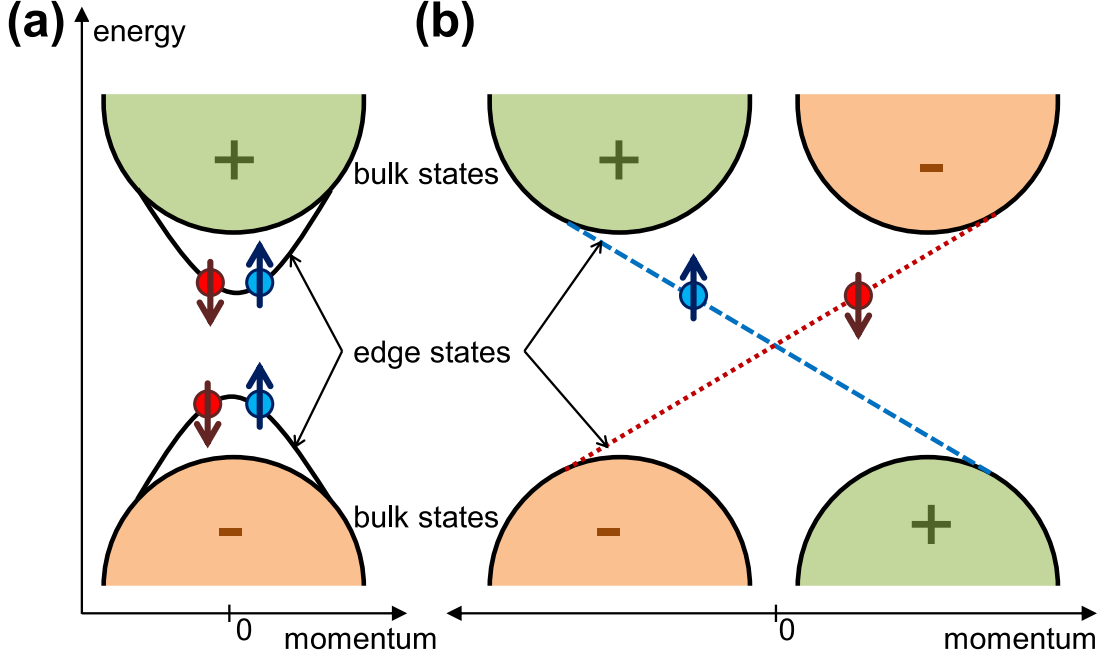


Figure 2.3.: Band inversion and edge/surface states [44]: (a) In a typical band structure, the conduction and valence bands are symmetric (+) and antisymmetric (-), respectively, and spin-up and spin-down states possess the same energy. (b) Combining two mutually inverted band structures gives rise to edge/surface bands that cross at the boundary. In the case of the QSH state (shown here), those edge states are spin-polarized and counterpropagate.

and eigenstates, an analytical and a finite-differences method, the evolution of QSH and QH states with increasing magnetic fields is discussed. The second and third parts of this chapter, Secs. 2.3 and 2.4, are devoted to the discussion of magnetic properties of this system: In Sec. 2.3, the magnetization and the susceptibility of HgTe quantum wells are discussed, while the magneto-optical conductivity is discussed in Sec. 2.4. Finally, the chapter is concluded by a brief summary.

2.1.2. HgTe quantum wells and effective model Hamiltonian

The system investigated in this chapter is a HgTe/CdTe quantum-well structure, which consists of a HgTe slab sandwiched between two slabs of CdTe (see Fig. 2.4 B). Using $\mathbf{k} \cdot \mathbf{p}$ theory, both bulk HgTe and bulk CdTe can be described by an 8-band Kane model near the Γ point [12, 17], which is shown in Fig. 2.4 A. Within the Kane model, there is one spin-degenerate pair of s -type bands (denoted by Γ_6 , a notation which originates from group theory), two pairs—heavy hole-like and light hole-like bands—of p -type bands with total angular momentum $J = 3/2$ (denoted by Γ_8), as well as one spin-degenerate pair of p -type bands with total angular momentum

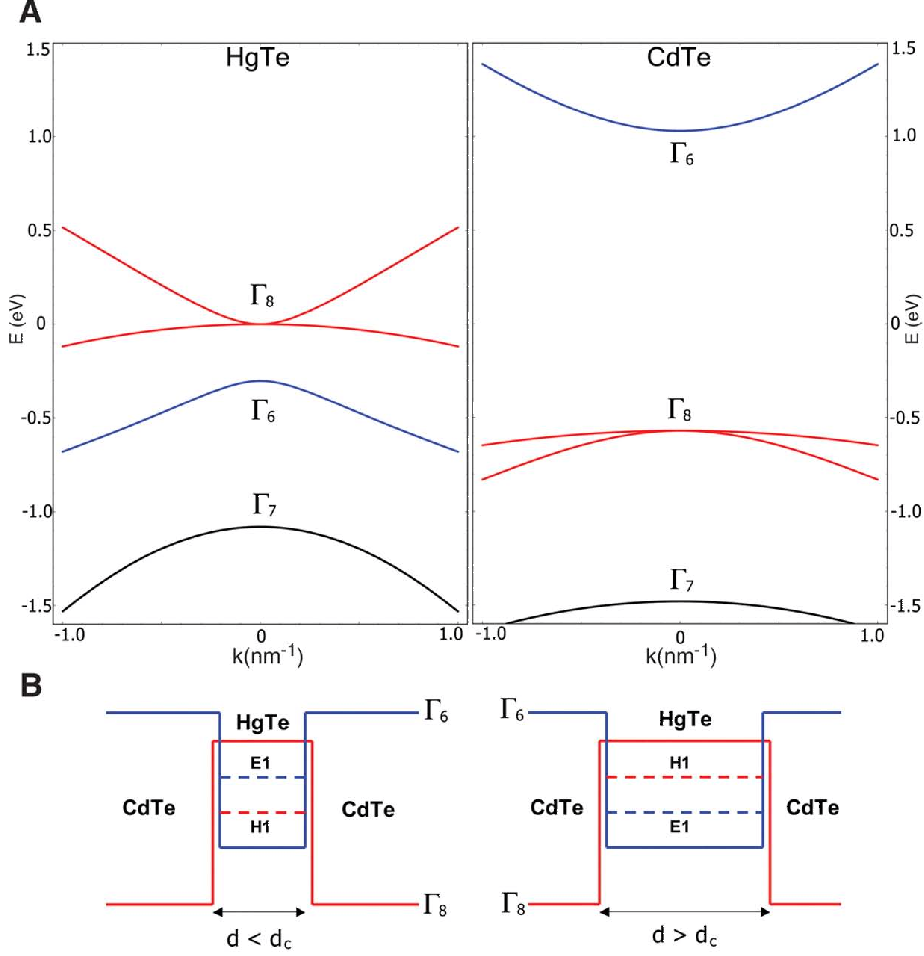


Figure 2.4.: (A) Bulk band structure of HgTe and CdTe near the Γ point and (B) a HgTe/CdTe quantum-well structure in the normal (left) and inverted (right) regimes. From Ref. 12.

$J = 1/2$ (denoted by Γ_7), which is split-off by the spin-orbit coupling [9]. Whereas the band structure in CdTe is normal, that is, the conduction bands are described by the s -like Γ_6 bands and the valence bands by the p -like Γ_7 and Γ_8 bands, the conduction band in bulk HgTe is given by the light hole-like Γ_8 bands and the remaining Γ_6 , Γ_7 , and Γ_8 bands describe valence bands. Hence, the band structure in HgTe is inverted. During the fabrication of a HgTe/CdTe heterostructure similar to the one shown in Fig. 2.4 B, one can tune the band structure of the 2D electronic system localized inside the HgTe quantum well: If the thickness d of the quantum well is below the critical thickness $d_c \approx 6.3$ nm, the band structure of the quantum well is normal, while the band structure is inverted if the thickness exceeds d_c . A simple, descriptive explanation for this behavior of the quantum-well band structure can be given

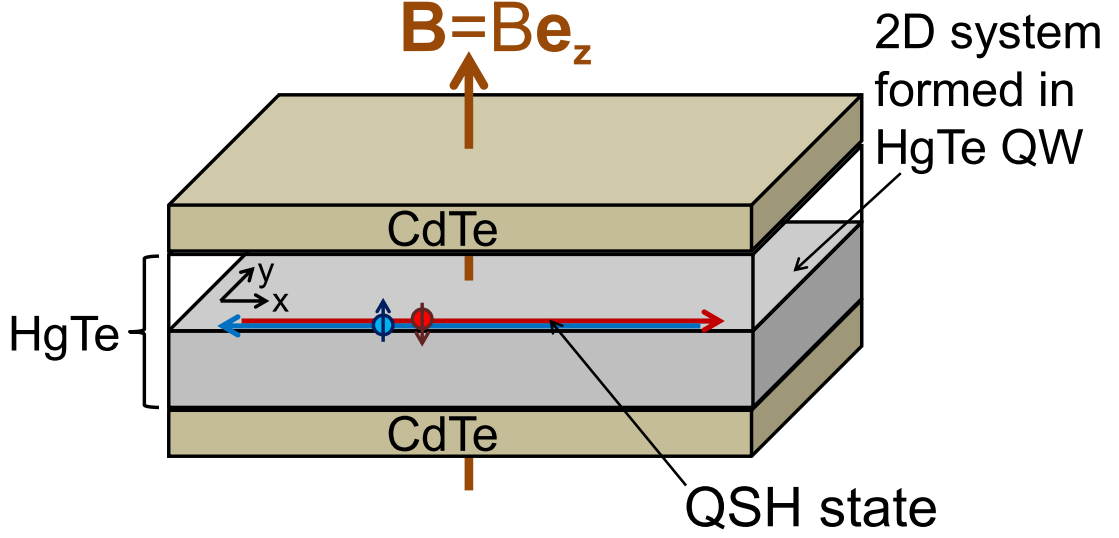


Figure 2.5.: A schematic illustration of the HgTe/CdTe quantum-well structure in the presence of a perpendicular magnetic field $\mathbf{B} = B\mathbf{e}_z$. The coordinate system is chosen such that the 2D electronic system is confined to the xy -plane ($z = 0$).

by noting that for a small thickness d of HgTe, the band structure of the entire heterostructure should be similar to CdTe, whereas the band structure should be similar to HgTe for large thicknesses of the HgTe slab [17].

The states and subbands of the heterostructure in Fig. 2.4 B are given by linear combinations of the bulk states of HgTe and CdTe and a more detailed calculation is necessary to obtain the exact form of those linear combinations. As shown in Refs. 12 and 17, one can neglect the split-off Γ_7 bands and essentially use this reduced 6-band model to calculate the subbands of the quantum well near the Γ point. Then, one obtains three categories of quantum-well subbands, electron-like subbands (E_1 , E_2 , ...) as well as heavy- (H_1 , H_2 , ...) and light hole-like (L_1 , L_2 , ...) subbands. The relevant subbands that capture the essential physical properties of the quantum-well structure at low energies are the electron-like E_1 and heavy hole-like H_1 subbands. Here, the E_1 states are formed from the Γ_6 and light hole-like Γ_8 states of the bulk, while the H_1 states are essentially formed from the heavy hole-like Γ_8 states [12, 17]. Both, the E_1 and the H_1 subbands are Kramers-degenerate due to time-reversal symmetry and therefore the effective low-energy Hamiltonian consists of four subbands: the electron-like states $|E \uparrow\rangle$ and $|E \downarrow\rangle$, that is, the E_1 subbands, and the (heavy-)hole-like states $|H \uparrow\rangle$ and $|H \downarrow\rangle$, that is, the H_1 subbands. Depending on the thickness d , the electron-like states are above the hole-like states and the band structure is normal or the electron-like states are below the hole-like states and the band structure is inverted (see Fig. 2.4 B).

If the coordinate system is chosen such that the growth direction of the heterostructure is along the z axis and that the 2D electronic system is confined to the xy -plane

2.1. Quantum spin Hall effect and HgTe quantum wells

(see Fig. 2.5 without the magnetic field), the effective Hamiltonian as introduced by Bernevig *et al.* [12] reads as

$$\hat{H}_0 = \left[\mathcal{C} - \frac{\mathcal{D}}{\hbar^2} (\hat{p}_x^2 + \hat{p}_y^2) \right] \mathbf{1} + \left[\mathcal{M} - \frac{\mathcal{B}}{\hbar^2} (\hat{p}_x^2 + \hat{p}_y^2) \right] \Gamma_5 + \frac{\mathcal{A}\hat{p}_x}{\hbar} \Gamma_1 + \frac{\mathcal{A}\hat{p}_y}{\hbar} \Gamma_2, \quad (2.1)$$

with the momentum operators \hat{p}_x and \hat{p}_y , the system parameters \mathcal{A} , \mathcal{B} , \mathcal{C} , \mathcal{D} , and \mathcal{M} (see below), and the 4×4 unity matrix $\mathbf{1}$. For the basis order $|E \uparrow\rangle$, $|H \uparrow\rangle$, $|E \downarrow\rangle$, $|H \downarrow\rangle$, the remaining 4×4 matrices are given by

$$\Gamma_1 = \begin{pmatrix} \sigma_x & 0 \\ 0 & -\sigma_x \end{pmatrix}, \Gamma_2 = \begin{pmatrix} -\sigma_y & 0 \\ 0 & -\sigma_y \end{pmatrix}, \Gamma_5 = \begin{pmatrix} \sigma_z & 0 \\ 0 & \sigma_z \end{pmatrix}, \quad (2.2)$$

where σ_x , σ_y , and σ_z denote the Pauli matrices.

The material parameters introduced above, \mathcal{A} , \mathcal{B} , \mathcal{C} , \mathcal{D} , and \mathcal{M} , are expansion parameters that depend on the quantum-well thickness d [12, 17]. Here, \mathcal{A} describes the coupling between the electron-like and hole-like bands, which can mix away from the Γ point, \mathcal{C} and \mathcal{D} describe a standard parabolic dispersion of all bands, whereas \mathcal{M} and \mathcal{B} determine whether the band structure is inverted or not: If the thickness of the quantum well is smaller than the critical thickness, $d_c \approx 6.3$ nm, the band structure is normal and $\mathcal{M}/\mathcal{B} < 0$, while, for a quantum-well thickness above d_c , the band structure is inverted and $\mathcal{M}/\mathcal{B} > 0$ [17]. As a final remark, we note that, in writing down the Hamiltonian (2.1), the bulk-inversion asymmetry, which is very small in this structure, has been ignored [17].

2.1.3. Model Hamiltonian in a perpendicular magnetic field

Since the focus of this chapter is on the magnetic properties of HgTe quantum wells, the magnetic field needs to be introduced in the Hamiltonian 2.1. The effect of a magnetic field $\mathbf{B}(\mathbf{r})$ can be included in this model by adding a Zeeman term [18] and replacing the momentum operator $\hat{\pi}_i$, where i denotes the in-plane coordinates x or y of the quantum well, with the kinetic momentum operator $\hat{\pi}_i = \hat{p}_i + eA_i(\mathbf{r})$, where $\mathbf{A}(\mathbf{r})$ is the magnetic vector potential and $e = |e|$ the elementary charge.

In our model, we consider a constant magnetic field perpendicular to the quantum well (see Fig. 2.5), that is, $\mathbf{B} = B\mathbf{e}_z$ with $B > 0$ (throughout this manuscript). Since hard walls will be added in Secs. 2.2.1 and 2.2.2 to confine the system in the y -direction, it is convenient to choose the gauge

$$\mathbf{A}(\mathbf{r}) = -By\mathbf{e}_x, \quad (2.3)$$

for which the effective Hamiltonian (2.1) becomes

$$\begin{aligned} \hat{H} = & \mathcal{C}\mathbf{1} + \mathcal{M}\Gamma_5 - \frac{\mathcal{D}\mathbf{1} + \mathcal{B}\Gamma_5}{\hbar^2} \left[\left(\hat{p}_x - \frac{\hbar y}{l_B^2} \right)^2 + \hat{p}_y^2 \right] \\ & + \frac{\mathcal{A}\Gamma_1}{\hbar} \left(\hat{p}_x - \frac{\hbar y}{l_B^2} \right) + \frac{\mathcal{A}\Gamma_2}{\hbar} \hat{p}_y + \frac{\mu_B B \Gamma_g^z}{2}, \end{aligned} \quad (2.4)$$

2. Magnetic properties of HgTe quantum wells

with the system parameters \mathcal{A} , \mathcal{B} , \mathcal{C} , \mathcal{D} , and \mathcal{M} as introduced above, the magnetic length $l_B = \sqrt{\hbar/e|B|} = \sqrt{\hbar/eB}$, and the Bohr magneton μ_B . For the basis order $|E \uparrow\rangle$, $|H \uparrow\rangle$, $|E \downarrow\rangle$, $|H \downarrow\rangle$, the 4×4 matrix Γ_g^z reads as

$$\Gamma_g^z = \begin{pmatrix} \sigma_g & 0 \\ 0 & -\sigma_g \end{pmatrix} \quad (2.5)$$

where $\sigma_g = \text{diag}(g_e, g_h)$ contains the effective (out-of-plane) g-factors g_e and g_h of the electron- and hole-like bands, respectively. Like \mathcal{A} , \mathcal{B} , \mathcal{C} , \mathcal{D} , and \mathcal{M} , g_e and g_h depend on the quantum-well thickness d [17].

In some cases, a reduced form of Eq. (2.4) can be used. For relatively strong magnetic fields, the terms quadratic with the kinetic momentum in Eq. (2.4) are small near the Γ point and can be omitted, as can the contribution from the Zeeman term, that is, $\mathcal{B} = \mathcal{D} = 0$ and $g_{e/h} = 0$ [32, 45].

2.2. Magnetic edge states

2.2.1. Analytical solution

In this section, we discuss the analytical solution—which in many ways resembles the calculation of the spin edge states in two-dimensional electron gases with spin-orbit coupling [40]—of the model system described by Eq. (2.4) for several different geometries: (i) bulk, that is, an infinite system, (ii) a semi-infinite system confined to $y > 0$, and (iii) a finite strip with the width w in y -direction. For all these cases, we apply periodic boundary conditions in x -direction. The confinement can be described by adding the infinite hard-wall potentials

$$V(y) = \begin{cases} 0 & \text{for } y > 0 \\ \infty & \text{elsewhere} \end{cases} \quad (2.6)$$

in (ii) and

$$V(y) = \begin{cases} 0 & \text{for } |y| < w/2 \\ \infty & \text{elsewhere} \end{cases} \quad (2.7)$$

in (iii).

In order to determine the solutions for cases (i)-(iii), we first need to find the general solution to the differential equation given by the free Schrödinger equation

$$\hat{H}\Psi(x, y) = E\Psi(x, y), \quad (2.8)$$

where $\Psi(x, y)$ is a four-component spinor. By imposing the appropriate boundary conditions along the y -direction on this general solution, we can obtain the solutions for each of the cases considered. Since translational invariance along the x -direction

as well as the spin direction are preserved by \hat{H} and $\hat{H} + V(y)\mathbf{1}$, respectively, the wave vector in x -direction, k , and the spin orientation, $s = \uparrow / \downarrow$, are good quantum numbers in each of the three cases, which naturally suggests the ansatz

$$\Psi_k^\uparrow(x, y) = \frac{e^{ikx}}{\sqrt{L}} \begin{pmatrix} f_\uparrow(\xi) \\ g_\uparrow(\xi) \\ 0 \\ 0 \end{pmatrix}, \quad \Psi_k^\downarrow(x, y) = \frac{e^{ikx}}{\sqrt{L}} \begin{pmatrix} 0 \\ 0 \\ f_\downarrow(\xi) \\ g_\downarrow(\xi) \end{pmatrix}, \quad (2.9)$$

where L is the length of the strip in x -direction and where, for convenience, we have introduced the transformation $\xi = \xi(y) = \sqrt{2}(y - l_B^2 k) / l_B$.

Inserting the ansatz (2.9) for spin-up electrons into Eq. (2.8), we obtain the following system of differential equations:

$$\begin{aligned} \left[\mathcal{C} - E - \frac{2\mathcal{D}}{l_B^2} \left(\frac{\xi^2}{4} - \partial_\xi^2 \right) \right] \begin{pmatrix} f_\uparrow(\xi) \\ g_\uparrow(\xi) \end{pmatrix} + \left[\mathcal{M} - \frac{2\mathcal{B}}{l_B^2} \left(\frac{\xi^2}{4} - \partial_\xi^2 \right) \right] \begin{pmatrix} f_\uparrow(\xi) \\ -g_\uparrow(\xi) \end{pmatrix} \\ - \frac{\sqrt{2}\mathcal{A}}{l_B} \begin{pmatrix} \left(\frac{\xi}{2} - \partial_\xi \right) g_\uparrow(\xi) \\ \left(\frac{\xi}{2} + \partial_\xi \right) f_\uparrow(\xi) \end{pmatrix} + \frac{\mu_B B}{2} \begin{pmatrix} g_e f_\uparrow(\xi) \\ g_h g_\uparrow(\xi) \end{pmatrix} = 0. \end{aligned} \quad (2.10)$$

Due to the specific form of Eq. (2.10), its solution can be conveniently written in terms of the parabolic cylindrical functions $D_\nu(\xi)$, which satisfy the following recurrence relations [46]:

$$\left(\frac{\xi}{2} \pm \partial_\xi \right) D_\nu(\xi) = \begin{cases} \nu D_{\nu-1}(\xi) \\ D_{\nu+1}(\xi) \end{cases}, \quad (2.11)$$

$$\left(\frac{\xi^2}{4} - \partial_\xi^2 \right) D_\nu(\xi) = \left(\nu + \frac{1}{2} \right) D_\nu(\xi). \quad (2.12)$$

With the heavy hole-like component $g_\uparrow(\xi)$ coupled to the electron-like component $f_\uparrow(\xi)$ by the raising operator and the opposite coupling described by the lowering operator, one type of solution is of the form

$$f_\uparrow(\xi) = v_1 D_\nu(\xi) \quad \text{and} \quad g_\uparrow(\xi) = v_2 D_{\nu-1}(\xi), \quad (2.13)$$

where v_1 and v_2 are complex numbers, which are to be determined by solving the system of linear equations obtained from inserting this ansatz into Eq. (2.10). This system has non-trivial solutions for

$$\nu = \nu_\pm^\uparrow = \frac{l_B^2}{2} \left[F(1) \pm \sqrt{F^2(1) + \frac{G_e(1)G_h(1)}{\mathcal{B}^2 - \mathcal{D}^2}} \right], \quad (2.14)$$

where

$$F(s) = s \frac{\mu_B B}{4} \left(\frac{g_e}{\mathcal{D} + \mathcal{B}} + \frac{g_h}{\mathcal{D} - \mathcal{B}} \right) - \frac{\mathcal{A}^2 - 2[\mathcal{M}\mathcal{B} + \mathcal{D}(E - \mathcal{C})]}{2(\mathcal{B}^2 - \mathcal{D}^2)} \quad (2.15)$$

2. Magnetic properties of HgTe quantum wells

and

$$G_{e/h}(s) = s \left(\frac{g_{e/h}\mu_B B}{2} - \frac{\mathcal{B} \pm \mathcal{D}}{l_B^2} \right) - (E - \mathcal{C}) \pm \mathcal{M}. \quad (2.16)$$

By determining those non-trivial solutions, for $\mathcal{A} \neq 0$ we find two (non-normalized) solutions

$$\chi_{\pm}^{\uparrow}(\xi) = \left(\sqrt{2}\mathcal{A}D_{\nu_{\pm}^{\uparrow}}(\xi)/l_B, c_{\pm}^{\uparrow}D_{\nu_{\pm}^{\uparrow}-1}(\xi) \right)^T \quad (2.17)$$

to Eq. (2.10) with

$$c_{\pm}^{\uparrow} = \mathcal{M} - (E - \mathcal{C}) - \frac{2(\mathcal{B} + \mathcal{D})}{l_B^2} \left(\nu_{\pm}^{\uparrow} + \frac{1}{2} \right) + \frac{g_e}{2}\mu_B B. \quad (2.18)$$

However, there is a second set of—in general—independent solutions to Eq. (2.10) that can be obtained from the ansatz

$$f_{\uparrow}(\xi) = u_1 D_{\nu}(-\xi) \quad \text{and} \quad g_{\uparrow}(\xi) = u_2 D_{\nu-1}(-\xi), \quad (2.19)$$

where u_1 and u_2 are complex numbers as before. With this ansatz yielding two further solutions,

$$\eta_{\pm}^{\uparrow}(\xi) = \left(\sqrt{2}\mathcal{A}D_{\nu_{\pm}^{\uparrow}}(-\xi)/l_B, -c_{\pm}^{\uparrow}D_{\nu_{\pm}^{\uparrow}-1}(-\xi) \right)^T, \quad (2.20)$$

the general solution to Eq. (2.10)—if $\mathcal{A} \neq 0$ —is given by

$$\begin{pmatrix} f_{\uparrow}(\xi) \\ g_{\uparrow}(\xi) \end{pmatrix} = \alpha \chi_{+}^{\uparrow}(\xi) + \beta \chi_{-}^{\uparrow}(\xi) + \gamma \eta_{+}^{\uparrow}(\xi) + \delta \eta_{-}^{\uparrow}(\xi), \quad (2.21)$$

where the coefficients α , β , γ , and δ are complex numbers to be determined by the boundary conditions of the problem.

A procedure similar to the one above can also be applied for the spin-down electrons in Eq. (2.9). Then, we find

$$\begin{pmatrix} f_{\downarrow}(\xi) \\ g_{\downarrow}(\xi) \end{pmatrix} = \tilde{\alpha} \chi_{+}^{\downarrow}(\xi) + \tilde{\beta} \chi_{-}^{\downarrow}(\xi) + \tilde{\gamma} \eta_{+}^{\downarrow}(\xi) + \tilde{\delta} \eta_{-}^{\downarrow}(\xi), \quad (2.22)$$

where we have introduced the vectors

$$\chi_{\pm}^{\downarrow}(\xi) = \left(c_{\pm}^{\downarrow}D_{\nu_{\pm}^{\downarrow}-1}(\xi), \sqrt{2}\mathcal{A}D_{\nu_{\pm}^{\downarrow}}(\xi)/l_B \right)^T \quad (2.23)$$

and

$$\eta_{\pm}^{\downarrow}(\xi) = \left(-c_{\pm}^{\downarrow}D_{\nu_{\pm}^{\downarrow}-1}(-\xi), \sqrt{2}\mathcal{A}D_{\nu_{\pm}^{\downarrow}}(-\xi)/l_B \right)^T, \quad (2.24)$$

with

$$\nu_{\pm}^{\downarrow} = \frac{l_B^2}{2} \left[F(-1) \pm \sqrt{F^2(-1) + \frac{G_e(-1)G_h(-1)}{\mathcal{B}^2 - \mathcal{D}^2}} \right] \quad (2.25)$$

and

$$c_{\pm}^{\downarrow} = \mathcal{M} + (E - \mathcal{C}) - \frac{2(\mathcal{B} - \mathcal{D})}{l_B^2} \left(\nu_{\pm}^{\downarrow} + \frac{1}{2} \right) + \frac{g_h}{2} \mu_B B. \quad (2.26)$$

As in the case of spin-up electrons, the coefficients $\tilde{\alpha}$, $\tilde{\beta}$, $\tilde{\gamma}$, and $\tilde{\delta}$ need to be fixed by boundary conditions. In the following, we will use the general solutions given by Eqs. (2.21) and (2.22) to determine the energy spectrum and wave functions for several different geometries.

(i) Bulk

If there is no confining potential $V(y)$, that is, if we consider an infinite system, where Eq. (2.10) holds for any $\xi \in \mathbb{R}$, we only have to require the wave function to be normalizable and accordingly we impose the boundary conditions $\lim_{\xi \rightarrow \pm\infty} f_{\uparrow}(\xi) = \lim_{\xi \rightarrow \pm\infty} g_{\uparrow}(\xi) = 0$. These requirements can only be satisfied if ν is a non-negative integer n in Eq. (2.13). In this case, $D_n(\xi) = 2^{-n/2} e^{-\xi^2/4} H_n(\xi/\sqrt{2})$ can be expressed by Hermite polynomials $H_n(\xi)$ [46], and both Eqs. (2.13) and (2.19) lead to the same solution. If $n \geq 1$, the ansatz from Eq. (2.13) leads to an eigenvalue problem for E from which the following Landau levels for spin-up electrons can be determined:

$$E_{\pm}^{\uparrow}(n) = \mathcal{C} - \frac{2\mathcal{D}n + \mathcal{B}}{l_B^2} + \frac{g_e + g_h}{4} \mu_B B \pm \sqrt{\frac{2n\mathcal{A}^2}{l_B^2} + \left(\mathcal{M} - \frac{2\mathcal{B}n + \mathcal{D}}{l_B^2} + \frac{g_e - g_h}{4} \mu_B B \right)^2}. \quad (2.27)$$

For $n = 0$, on the other hand, Eqs. (2.13) and (2.19) reduce to the ansatz $f_{\uparrow}(\xi) = v_1 D_0(\xi)$ and $g_{\uparrow}(\xi) = 0$ and we obtain the Landau level

$$E^{\uparrow}(0) = \mathcal{C} + \mathcal{M} - \frac{\mathcal{D} + \mathcal{B}}{l_B^2} + \frac{g_e}{2} \mu_B B. \quad (2.28)$$

By requiring $\lim_{\xi \rightarrow \pm\infty} f_{\downarrow}(\xi) = \lim_{\xi \rightarrow \pm\infty} g_{\downarrow}(\xi) = 0$, the Landau levels for spin-down electrons can be calculated similarly as

$$E_{\pm}^{\downarrow}(n) = \mathcal{C} - \frac{2\mathcal{D}n - \mathcal{B}}{l_B^2} - \frac{g_e + g_h}{4} \mu_B B \pm \sqrt{\frac{2n\mathcal{A}^2}{l_B^2} + \left(\mathcal{M} - \frac{2\mathcal{B}n - \mathcal{D}}{l_B^2} - \frac{g_e - g_h}{4} \mu_B B \right)^2} \quad (2.29)$$

and

$$E^{\downarrow}(0) = \mathcal{C} - \mathcal{M} - \frac{\mathcal{D} - \mathcal{B}}{l_B^2} - \frac{g_h}{2} \mu_B B. \quad (2.30)$$

2. Magnetic properties of HgTe quantum wells

With Eqs. (2.27)-(2.30), we have recovered the Landau levels found in Ref. 18. The corresponding eigenstates are given in the Appendix B.

In writing down Eqs. (2.27)-(2.30), we have adopted the convention that $B > 0$, that is, the magnetic field points in the z -direction. The formulas of the Landau levels for $B < 0$ can be obtained from Eqs. (2.27)-(2.30) via the relations $E^s(0, B) = E^{-s}(0, -B)$ and $E_{\pm}^s(n, B) = E_{\pm}^{-s}(n, -B)$ [note that the magnetic length in Eqs. (2.27)-(2.30) is given by $l_B = \sqrt{\hbar/e|B|}$].

(ii) Semi-infinite system

In the presence of the confining potential given by Eq. (2.6), the wave function is required to vanish at the boundary $y = 0$ as well as at $y \rightarrow \infty$. Thus, we invoke the boundary conditions $\lim_{\xi \rightarrow \infty} f_{\uparrow/\downarrow}(\xi) = \lim_{\xi \rightarrow \infty} g_{\uparrow/\downarrow}(\xi) = 0$ and $f_{\uparrow/\downarrow}(\xi_0) = g_{\uparrow/\downarrow}(\xi_0) = 0$ for spin-up as well as spin-down electrons, where $\xi_0 = -\sqrt{2}l_B k$. The condition for $\xi \rightarrow \infty$ can only be satisfied for $\gamma = \delta = 0$ and $\tilde{\gamma} = \tilde{\delta} = 0$, respectively. Then, each remaining pair of coefficients, α and β as well as $\tilde{\alpha}$ and $\tilde{\beta}$, from Eqs. (2.21) and (2.22) has to be calculated from the condition at $y = 0$, that is, at ξ_0 . The resulting linear systems of equations have non-trivial solutions if

$$c_{-}^{\uparrow/\downarrow} D_{\nu_{-}^{\uparrow/\downarrow}-1}(\xi_0) D_{\nu_{+}^{\uparrow/\downarrow}}(\xi_0) - c_{+}^{\uparrow/\downarrow} D_{\nu_{+}^{\uparrow/\downarrow}-1}(\xi_0) D_{\nu_{-}^{\uparrow/\downarrow}}(\xi_0) = 0. \quad (2.31)$$

This transcendental equation enables us to calculate the electron dispersion for spin-up [$s = \uparrow$ in Eq. (2.31)] as well as for spin-down electrons [$s = \downarrow$ in Eq. (2.31)]. The corresponding eigenstates can be determined by explicitly calculating the coefficients α , β and $\tilde{\alpha}$, $\tilde{\beta}$, respectively.

(iii) Finite-strip geometry

In the finite-strip geometry described by Eq. (2.7), the wave function has to vanish at the potential boundaries, that is, Eqs. (2.21) and (2.22) have to vanish at $\xi_{1/2} = \sqrt{2}(\mp w/2 - l_B^2 k)/l_B$. The corresponding linear systems of equations defined by this condition have non-trivial solutions if

$$\det \begin{pmatrix} \chi_{+}^{\uparrow/\downarrow}(\xi_1) & \chi_{-}^{\uparrow/\downarrow}(\xi_1) & \eta_{+}^{\uparrow/\downarrow}(\xi_1) & \eta_{-}^{\uparrow/\downarrow}(\xi_1) \\ \chi_{+}^{\uparrow/\downarrow}(\xi_2) & \chi_{-}^{\uparrow/\downarrow}(\xi_2) & \eta_{+}^{\uparrow/\downarrow}(\xi_2) & \eta_{-}^{\uparrow/\downarrow}(\xi_2) \end{pmatrix} = 0 \quad (2.32)$$

for spin-up ($s = \uparrow$) and spin-down ($s = \downarrow$) electrons, respectively. Similarly to (ii), the transcendental Eq. (2.32) represents exact expressions from which the dispersion of the electrons can be calculated. The corresponding eigenstates can be determined by explicitly calculating the coefficients α , β , γ , and δ for spin-up electrons and $\tilde{\alpha}$, $\tilde{\beta}$, $\tilde{\gamma}$, and $\tilde{\delta}$ for spin-down electrons, respectively.

Having derived transcendental equations from which the electronic dispersion (and indirectly the eigenstates) can be determined for semi-infinite as well as finite-strip systems, we will also introduce an alternative method to calculate the spectrum and eigenstates of a finite strip.

2.2.2. Numerical finite-difference solution

In addition to solving the exact expression (2.32), we calculate the eigenspectrum and eigenstates also by using a finite-difference scheme to express Eq. (2.4) [47]. We discretize Eq. (2.4) for $B = 0$ and account for the magnetic field by introducing the Peierls' phase [48] to describe the vector potential given by Eq. (2.3) and an additional on-site term to describe the Zeeman term. If only nearest neighbors are considered and there is no magnetic field, this procedure leads to the Hamiltonian introduced in Ref. 17.

For reasons of improving the convergence of our calculation, we go beyond the nearest-neighbor approximation and include the next-nearest neighbors. Due to translational invariance along the x -direction, the x -coordinate can be Fourier transformed to the reciprocal space and we obtain the Hamiltonian

$$\hat{H}_{\text{FD}} = \sum_{k,n,n'} \sum_{\alpha\beta} \mathcal{H}_{\alpha\beta}(k; n, n') \hat{c}_{kn\alpha}^\dagger \hat{c}_{kn'\beta}, \quad (2.33)$$

where k is the momentum along the x -direction, n and $n' \in \mathbb{Z}$ are discrete y -coordinates, α and β denote the basis states $|E \uparrow\rangle$, $|H \uparrow\rangle$, $|E \downarrow\rangle$, $|H \downarrow\rangle$, and $\hat{c}_{kn\alpha}^\dagger$ ($\hat{c}_{kn\alpha}$) is the creation (annihilation) operator of those states. Furthermore, we have introduced the matrix

$$\begin{aligned} \mathcal{H}_{\alpha\beta}(k; n, n') = & \left[\mathcal{C}(\mathbf{1})_{\alpha\beta} + \mathcal{M}(\Gamma_5)_{\alpha\beta} - \frac{\mathcal{D}(\mathbf{1})_{\alpha\beta} + \mathcal{B}(\Gamma_5)_{\alpha\beta}}{a^2} \mathcal{F}(k, B, n) \right. \\ & + \frac{\mathcal{A}}{a} (\Gamma_1)_{\alpha\beta} \mathcal{G}(k, B, n) + \frac{\mu_B B}{2} (\Gamma_g)_{\alpha\beta} \left. \right] \delta_{nn'} \\ & + \left\{ \frac{4 [\mathcal{D}(\mathbf{1})_{\alpha\beta} + \mathcal{B}(\Gamma_5)_{\alpha\beta}]}{3a^2} + \frac{2i\mathcal{A}(n-n')}{3a} (\Gamma_2)_{\alpha\beta} \right\} \\ & \times (\delta_{n,n'+1} + \delta_{n,n'-1}) \\ & - \left[\frac{\mathcal{D}(\mathbf{1})_{\alpha\beta} + \mathcal{B}(\Gamma_5)_{\alpha\beta}}{12a^2} + \frac{i\mathcal{A}(n-n')}{24a} (\Gamma_2)_{\alpha\beta} \right] (\delta_{n,n'+2} + \delta_{n,n'-2}), \end{aligned} \quad (2.34)$$

where

$$\mathcal{F}(k, B, n) = 5 - \frac{8 \cos(ka - a^2 n / l_B^2)}{3} + \frac{\cos(2ka - 2a^2 n / l_B^2)}{6}, \quad (2.35)$$

$$\mathcal{G}(k, B, n) = \frac{4 \sin(ka - a^2 n / l_B^2)}{3} - \frac{\sin(2ka - 2a^2 n / l_B^2)}{6}, \quad (2.36)$$

2. Magnetic properties of HgTe quantum wells

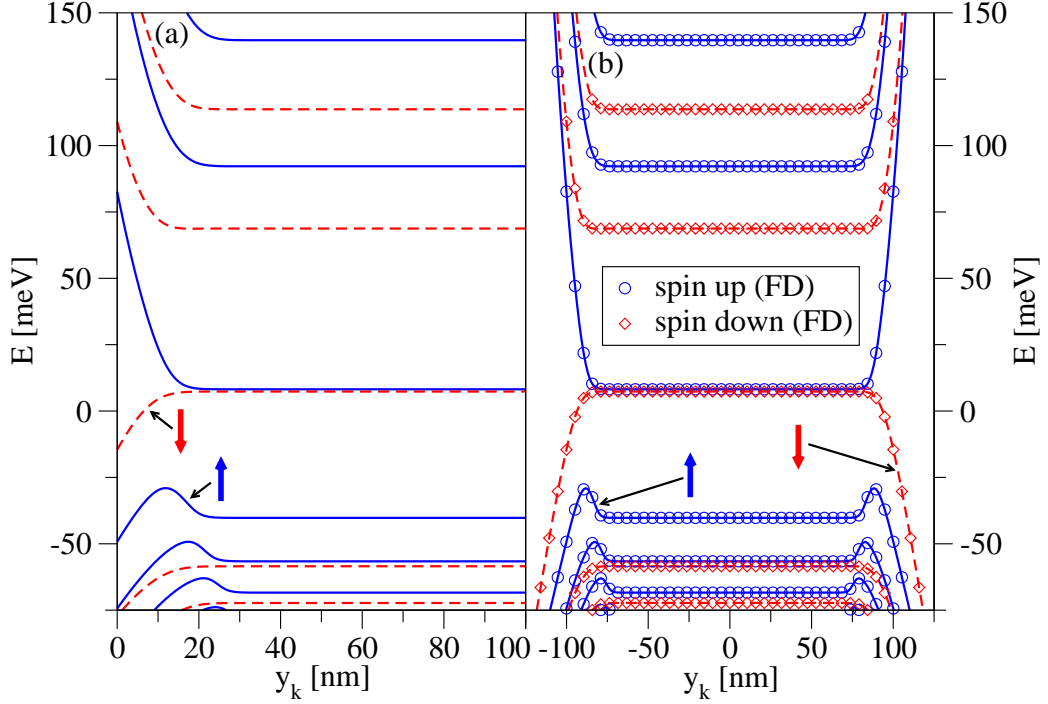


Figure 2.6.: Calculated energy spectra of (a) a semi-infinite system and (b) a finite strip of width $w = 200$ nm for $B = 10$ T, $\mathcal{A} = 364.5$ meV nm, $\mathcal{B} = -686.0$ meV nm², $\mathcal{C} = 0$, $\mathcal{D} = -512.0$ meV nm², $\mathcal{M} = -10.0$ meV, and $g_e = g_h = 0$. Here, the energy spectra are plotted versus $y_k = l_B^2 k$. The solid and dashed lines represent $s = \uparrow$ and $s = \downarrow$ states, respectively, which have been calculated using the analytical methods from Sec. 2.2.1 [case (ii) for Fig. (a) and case (iii) for Fig. (b)]. Results obtained by the finite-difference method from Sec. 2.2.2 are represented by circles (spin up) and diamonds (spin down) in Fig. (b).

and a denotes the distance between two lattice points in y -direction (see also Appendix A). However, in the finite-strip geometry considered here, the matrix given by Eq. (2.34) has to be modified at the edges along the y -direction, where only nearest neighbors can be used for the approximation of the derivatives with respect to y . Following these modifications, the eigenspectrum and the eigenstates of the system in a finite-strip geometry can be determined numerically.

2.2.3. Comparison between the analytical and numerical solutions

We compare the results obtained by the analytical procedures described in Sec. 2.2.1 with those of the finite-difference method introduced in Sec. 2.2.2. For illustration, Fig. 2.6 shows the energy spectra of a semi-infinite system [Fig. 2.6 (a)] and a finite

strip of width $w = 200$ nm [Fig. 2.6 (b)]. Here, we have chosen the magnetic field $B = 10$ T and the parameters $\mathcal{A} = 364.5$ meV nm, $\mathcal{B} = -686.0$ meV nm², $\mathcal{C} = 0$, $\mathcal{D} = -512.0$ meV nm², $\mathcal{M} = -10.0$ meV, and $g_e = g_h = 0$, which (apart from the vanishing g-factors) correspond to the thickness of $d = 7.0$ nm [17, 4]. Whereas the energy spectrum of a semi-infinite system is calculated using the transcendental Eq. (2.31), both procedures described above, solving the transcendental Eq. (2.32) or diagonalizing the finite-difference Hamiltonian (2.33), can be used to calculate the eigenspectrum of the Hamiltonian (2.4) in a finite-strip geometry. The finite-difference calculations for Fig. 2.6 (b) have been conducted for 201 lattice sites along the y -direction, for which we get a relative error of 10^{-6} - 10^{-5} . Figure 2.6 (b) also clearly illustrates the nearly perfect agreement between the analytical and numerical solutions. As can be expected if the magnetic length l_B is small compared to the width of the sample w , the energy spectra near the edge as well as the energy spectra in the bulk are almost identical for the semi-infinite and finite systems as shown in Figs. 2.6 (a) and 2.6 (b). The bulk Landau levels are perfectly characterized by Eqs. (2.27)-(2.30).

2.2.4. Results

In this section, we investigate the magnetic field dependence of the energy spectrum and its corresponding eigenstates in a finite-strip geometry with the width $w = 200$ nm. The graphs shown in this section have been calculated using the finite-difference scheme from Sec. 2.2.2 with 201 lattice sites along the y -direction (see also Sec. 2.2.3).

Ordinary insulator regime

First, we examine the quantum-well spectrum in the ordinary insulator regime, that is, for a thickness $d < d_c$, where the band structure is normal and there are no QSH states (at zero magnetic field). Figure 2.7 shows the energy spectrum and (selected) eigenstates at different magnetic fields for the material parameters $\mathcal{A} = 387$ meV nm, $\mathcal{B} = -480.0$ meV nm², $\mathcal{C} = 0$, $\mathcal{D} = -306.0$ meV nm², and $\mathcal{M} = 9.0$ meV, which correspond to a quantum-well thickness of $d = 5.5$ nm [4]. As illustrated by Fig. 2.7 (a) (i), which shows the spectrum for $B = 0$, only bulk states, but no edge states can be found [see Figs. 2.7 (a) (ii) and (iii)], a situation which changes little if small magnetic fields are applied [see Fig. 2.7 (b)]. Only if the magnetic field is increased further, do Landau levels [given by Eqs. (2.27)-(2.30)] and corresponding QH edge states begin to form as can be seen in Figs. 2.7 (c) and (d). Comparing Figs. 2.7 (c) and (d), one can also discern that with increasing magnetic field the QH edge states become more localized.

2. Magnetic properties of HgTe quantum wells

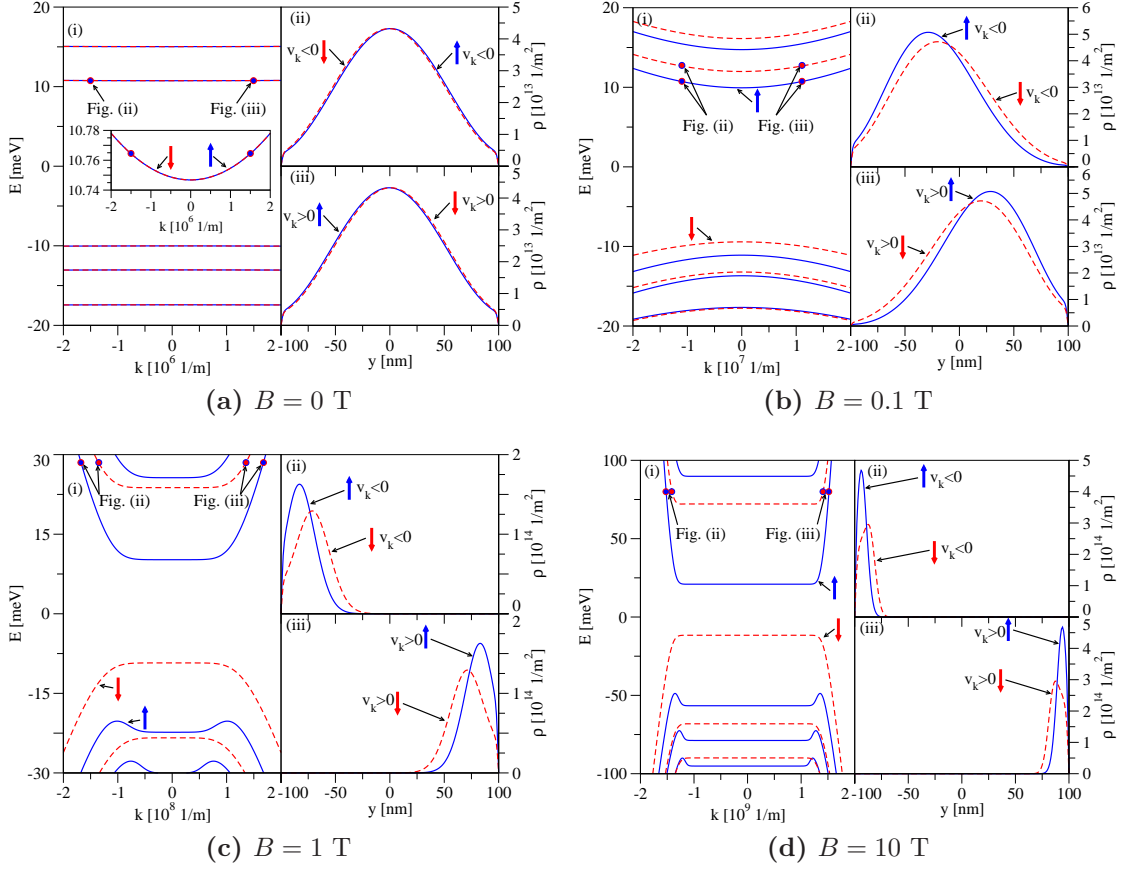


Figure 2.7.: (i) Calculated energy spectrum and (ii), (iii) probability densities $\rho(x, y) = |\Psi(x, y)|^2$ of selected states for $d = 5.5$ nm, $w = 200$ nm, and different magnetic fields. Here, solid and dashed lines represent $s = \uparrow$ and $s = \downarrow$ states, respectively. For each magnetic field, the states shown in panels (ii) and (iii) are marked in the energy spectrum, panel (i), by dots. The velocity with which the states propagate along the x -direction is given by $v_k = [\partial E(k)/\partial k]/\hbar$.

QSH regime

In Fig. 2.8, by contrast, the energy spectrum and (selected) eigenstates of a strip with the width $w = 200$ nm are presented for the material parameters $\mathcal{A} = 364.5$ meV nm, $\mathcal{B} = -686.0$ meV nm², $\mathcal{C} = 0$, $\mathcal{D} = -512.0$ meV nm², $\mathcal{M} = -10.0$ meV, $g_e = 22.7$, and $g_h = -1.21$, corresponding to a quantum-well thickness $d = 7.0$ nm [4, 17], that is, for parameters in the QSH regime (at $B = 0$), and several strengths of the perpendicular magnetic field. The spectra and states in Fig. 2.8 illustrate the evolution of QSH and QH states in HgTe.

Figure 2.8 (a) (i) shows the spectrum at zero magnetic field. At this magnetic field, one can observe the QSH state inside the bulk gap, that is, two degenerate

2.2. Magnetic edge states

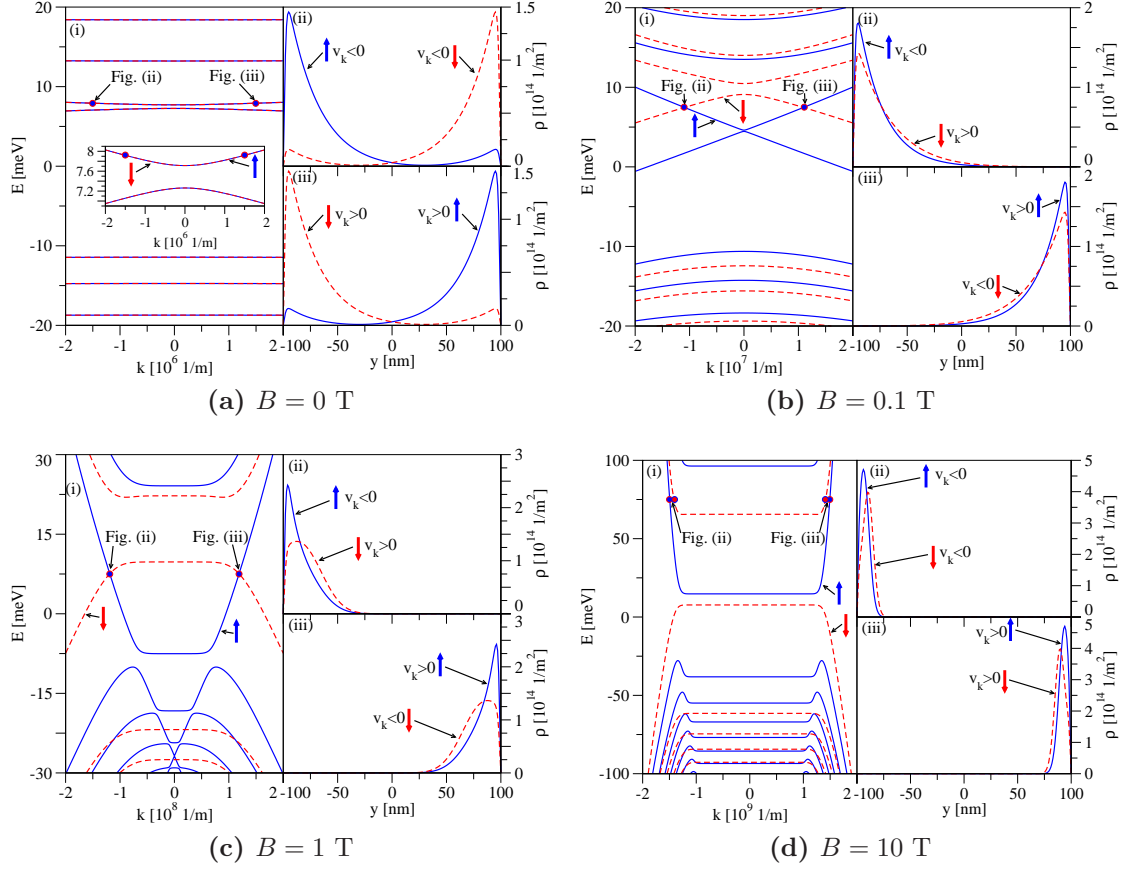


Figure 2.8.: (i) Calculated energy spectrum and (ii), (iii) probability densities $\rho(x, y) = |\Psi(x, y)|^2$ of selected states for $d = 7.0$ nm, $w = 200$ nm, and different magnetic fields. Here, solid and dashed lines represent $s = \uparrow$ and $s = \downarrow$ states, respectively. For each magnetic field, the states shown in panels (ii) and (iii) are marked in the energy spectrum, panel (i), by dots. The velocity with which the states propagate along the x -direction is given by $v_k = [\partial E(k)/\partial k]/\hbar$.

pairs of counterpropagating, spin-polarized edge states, one pair at each edge [see Figs. 2.8 (a) (ii) and (iii)]. As found in Ref. 38, at $k = 0$ the wave functions of QSH edge states with the same spin, but at opposite edges overlap thereby opening up a gap [see the inset in Fig. 2.8 (a) (i)]. By increasing the width of the strip, the overlap of the edge-state wave functions with the same spin is diminished and one can remove this finite-size effect.

For small magnetic fields [Fig. 2.8 (b)], apart from the splitting of spin-up and down states, the situation is at first glance quite comparable to the one in Fig. 2.8 (a). Most importantly, one can still find pairs of counterpropagating, spin-polarized states in the vicinity of each neutrality point [for example, the states shown in Figs. 2.8 (b) (ii) and (iii)], that is, the crossovers between the lowest (hole-like) conduction band and

2. Magnetic properties of HgTe quantum wells

uppermost (electron-like) valence band [marked by dots in Fig. 2.8 (b) (i)]. However, we stress that these counterpropagating, spin-polarized states which can be found (at a given edge) if the Fermi level is close to the neutrality points, are not connected with each other by time-reversal symmetry and are therefore not topologically protected (for example, against spin-orbit coupling).

Going to $B = 1$ T [Fig. 2.8 (c)], we can still find counterpropagating, spin-polarized states near and at the crossovers between the lowest (hole-like) conduction and uppermost (electron-like) valence bands, which (in the bulk) have evolved into the $E^\uparrow(0)$ and $E^\downarrow(0)$ Landau levels. As the center of the orbital motion is given by $\sqrt{2}l_B k$, one can see that those states are now no longer as localized as before at the edges [see Figs. 2.8 (c) (ii) and (iii)]. Meanwhile, the bulk states from Fig. 2.8 (a) have also evolved into Landau levels given by Eqs. (2.27) and (2.29) with localized QH edge as well as bulk states. From Fig. 2.8 (c), one can also discern another feature of the energy spectrum and eigenstates that develops with an increasing magnetic field, namely the appearance of 'bumps' [see the spin-up valence bands in Fig. 2.8 (c) (i)]. If the Fermi level crosses those 'bumps', one finds states which are localized near the same edge and carry the same spin, but counterpropagate. This has also been observed in Ref. 34, where those states gave rise to exotic plateaus in the longitudinal and Hall resistances. As can be seen in Figs. 2.7 (c) and (d) [as well as later in Figs. 2.8 (d), 2.11 (c), and 2.11 (d)], this behavior can also be found for other quantum well parameters.

The situation described so far changes for high magnetic fields [Fig. 2.8 (d)], when the electron-like band described by $E^\uparrow(0)$ (in the bulk) is above the hole-like $E^\downarrow(0)$ band. Then, there is no longer any crossover between the dispersions of electron- and hole-like bands and one consequently cannot find counterpropagating, spin-polarized states anymore, just QH edge states propagating in the same direction [for example, the states shown in Figs. 2.8 (d) (ii) and (iii)].

As has been known for a long time, the uppermost (electron-like) valence and the lowest (hole-like) conduction Landau levels cross at a finite magnetic field B_c in inverted HgTe/CdTe quantum wells [49, 50, 51]. The transition between the two situations, the one where counterpropagating, spin-polarized states exist and the one where they do not, happens exactly at this crossover point: As long as the hole-like band is above the electron-like band, that is, as long as the band structure remains inverted, one can find counterpropagating, spin-polarized states in addition to the QH states. Otherwise, there are only QH states.

This crossover point can be easily calculated from the Landau levels via the condition $E^\uparrow(0) = E^\downarrow(0)$, from which we get

$$B_c = \frac{\mathcal{M}}{2\pi\mathcal{B}/\Phi_0 - (g_e + g_h)\mu_B/4} \quad (2.37)$$

for the magnetic field at which the transition happens (valid only for $B_c > 0$). Here, $\Phi_0 = 2\pi\hbar/e$ denotes the magnetic flux quantum. The validity of the result given by

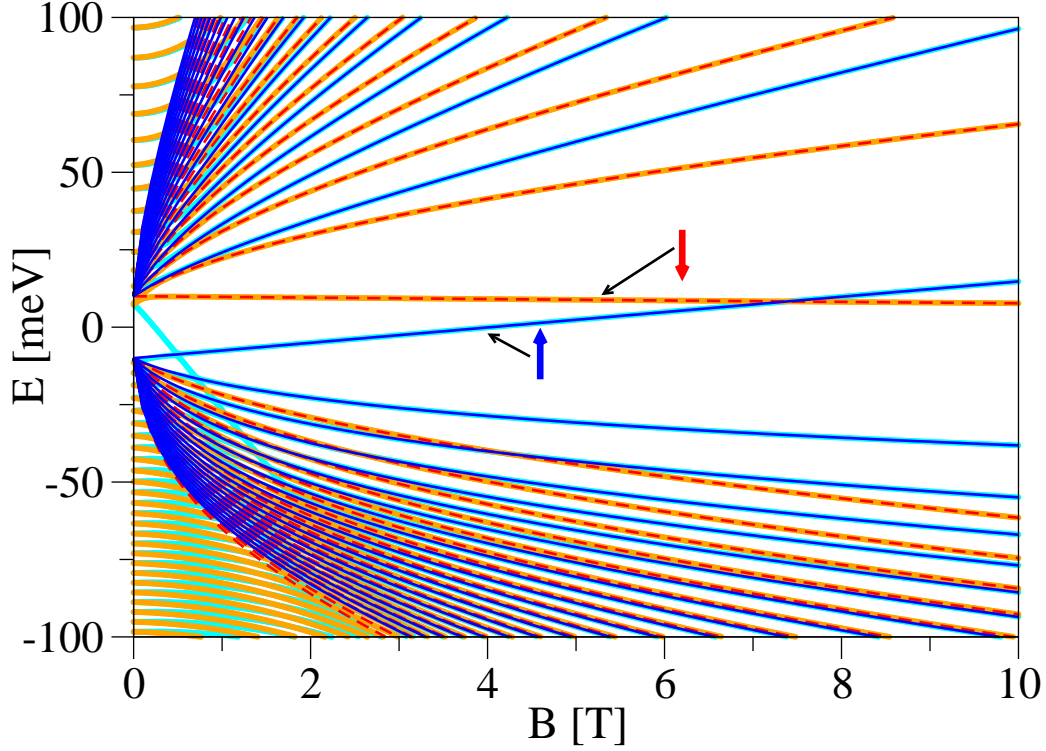


Figure 2.9.: Magnetic field dependence of the states at $k = 0$ in a finite strip of width $w = 200$ nm compared to the bulk Landau levels given by Eqs. (2.27)-(2.30). The thinner solid and dashed lines represent bulk Landau levels for $s = \uparrow$ and $s = \downarrow$, respectively. The levels of the finite-strip geometry are displayed by thick lines. All levels displayed here have been calculated for band parameters corresponding to $d = 7.0$ nm.

Eq. (2.37) is also illustrated by Fig. 2.9, which shows the magnetic field dependence of the energies of the finite strip with width $w = 200$ nm at $k = 0$ and of the bulk Landau levels for the same band parameters as above. As can be expected, the energies at $k = 0$ are given by the Landau levels (2.27)-(2.30) at high magnetic fields. Most importantly, the crossover between the electron-like $E^\uparrow(0)$ and the hole-like $E^\downarrow(0)$ bands happens in the region, where the B -dependence of the energy levels at $k = 0$ is already described extremely well by those Landau levels and from Eq. (2.37) we find $B_c \approx 7.4$ T, consistent with the numerical result that can be extracted from Fig. 2.9. Furthermore, one can see how the $E^\uparrow(0)$ band is below the $E^\downarrow(0)$ band for $B < B_c$, and how the situation is reversed for $B > B_c$.

Therefore, we find that if the magnetic field is not too high, the counterpropagating, spin-polarized states persist at finite magnetic fields, consistent with the conclusions in Refs. 32 and 33, where the reduced model (mentioned in Sec. 2.1.3) for HgTe has been used, and Ref. 34. Only for high magnetic fields, the band structure becomes

2. Magnetic properties of HgTe quantum wells

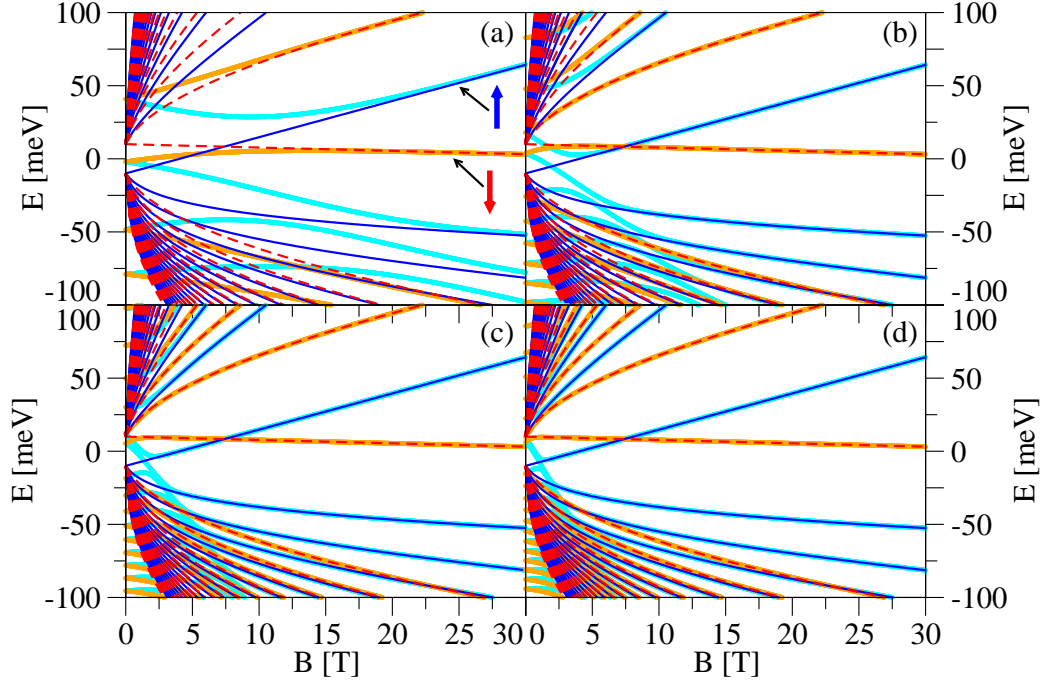


Figure 2.10.: Magnetic field dependence of the states at $k = 0$ in finite strips with the widths (a) $w = 25$ nm, (b) $w = 50$ nm, (c) $w = 75$ nm, and (d) $w = 100$ nm compared to the bulk Landau levels given by Eqs. (2.27)-(2.30). The thinner solid and dashed lines represent bulk Landau levels for $s = \uparrow$ and $s = \downarrow$, respectively. The levels of the finite-strip geometry are displayed by thick lines. All levels displayed here have been calculated for band parameters corresponding to $d = 7.0$ nm.

normal and one enters the ordinary insulator regime, in which no counterpropagating, spin-polarized states can be found (see also Ref. 34). We remark that the description presented in this section also bears out if other widths $w \gtrsim 100$ nm of the finite strip are investigated. For larger widths, the formation of Landau levels sets in already at lower magnetic fields, whereas higher fields are needed to observe Landau levels in more narrow strips. If very small samples ($w \lesssim 50$ nm) are investigated, however, we find that there is no crossover between the electron-like $E^\uparrow(0)$ and the hole-like $E^\downarrow(0)$ bands, as illustrated by Fig. 2.10, which shows a comparison between the bulk Landau levels and the states calculated at $k = 0$ for band parameters corresponding to $d = 7.0$ nm and several small widths w . Only if $w \gtrsim 50$ nm, the gap due to the finite size of the sample at $B = 0$ is reduced far enough and one can observe a crossover of the $E^\uparrow(0)$ and $E^\downarrow(0)$ bands at $B = B_c$ which is then given by Eq. (2.37).

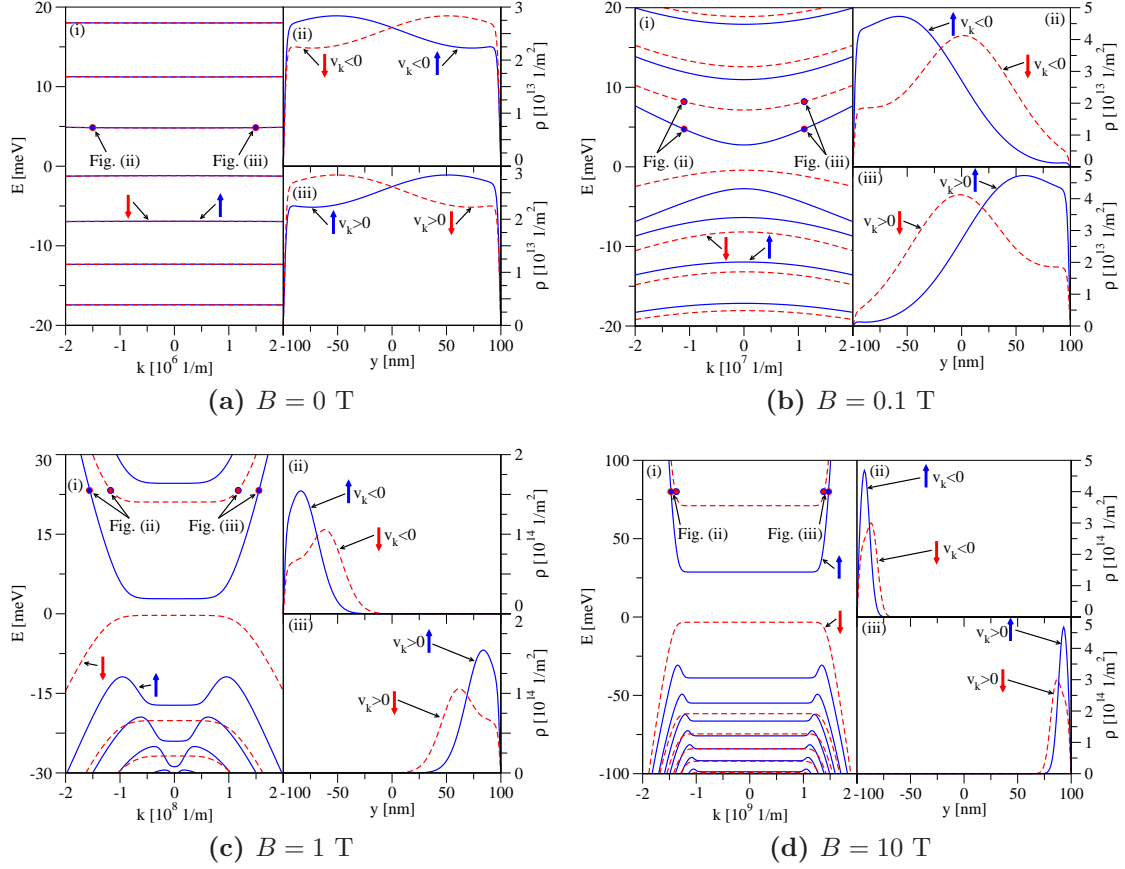


Figure 2.11.: (i) Calculated energy spectrum and (ii), (iii) probability densities $\rho(x, y) = |\Psi(x, y)|^2$ of selected states for $d = 6.3$ nm, $w = 200$ nm, and different magnetic fields. Here, solid and dashed lines represent $s = \uparrow$ and $s = \downarrow$ states, respectively. For each magnetic field, the states shown in panels (ii) and (iii) are marked in the energy spectrum, panel (i), by dots. The velocity with which the states propagate along the x -direction is given by $v_k = [\partial E(k)/\partial k]/\hbar$.

Critical regime

Finally, for the purpose of comparison to the discussion above, Fig. 2.11 shows the energy spectrum and (selected) eigenstates at different magnetic fields for a strip with the width $w = 200$ nm and the material parameters $\mathcal{A} = 373.5$ meV nm, $\mathcal{B} = -857.0$ meV nm², $\mathcal{C} = 0$, $\mathcal{D} = -682.0$ meV nm², $\mathcal{M} = -0.035$ meV, $g_e = 18.5$, and $g_h = 2.4$, which correspond to the critical regime at a quantum-well thickness of $d = d_c = 6.3$ nm [4, 18]. For $B = 0$, instead of edge states, we find states whose probability densities are spread over the entire width of the strip with a slight preponderance near one of the edges [see Fig. 2.11 (a)]. with increasing magnetic field the states become more localized [see Figs. 2.11 (b) and 2.11 (c)] and, finally, one can find QH

edge states [see Fig. 2.11 (d)].

2.3. Magnetic oscillations

2.3.1. General formalism

In this section, we discuss the magnetization and magnetic oscillations in HgTe quantum wells. Our starting point is the grand potential

$$\Omega(T, \mu, B) = -\frac{S}{\beta} \int d\epsilon \rho(\epsilon) \ln \{1 + \exp[-\beta(\epsilon - \mu)]\}, \quad (2.38)$$

where $\beta = 1/(k_B T)$ and T denotes the temperature, k_B the Boltzmann constant, μ the chemical potential, $\rho(\epsilon)$ the density of states per unit area, and S is the surface area.

We make the electron-hole transformation and divide the spectrum in the electron and hole contributions, $\rho_e(\epsilon) = \rho(\epsilon)\Theta(\epsilon - E_n)$ and $\rho_h(\epsilon) = \rho(\epsilon)\Theta(E_n - \epsilon)$, where $E_n = E_n(B)$ denotes the neutrality point. Then, we can rewrite $\Omega(T, \mu, B)$ as

$$\Omega(T, \mu, B) = \Omega_e(T, \mu, B) + \Omega_h(T, \mu, B) + S \int d\epsilon \rho_h(\epsilon) (\epsilon - \mu), \quad (2.39)$$

where

$$\Omega_e(T, \mu, B) = -\frac{S}{\beta} \int d\epsilon \rho_e(\epsilon) \ln \{1 + \exp[-\beta(\epsilon - \mu)]\} \quad (2.40)$$

and

$$\Omega_h(T, \mu, B) = -\frac{S}{\beta} \int d\epsilon \rho_h(\epsilon) \ln \{1 + \exp[\beta(\epsilon - \mu)]\} \quad (2.41)$$

denote the grand potentials of electrons and holes, respectively. The total particle number in the system is given by $N_{\text{tot}} = -[\partial\Omega(T, \mu, B)/\partial\mu]$. However, it is more convenient to distinguish between electrons and holes and to work with the carrier imbalance $N = N_e - N_h$ (with $N_{e/h}$ denoting the number of electrons and holes, respectively). Following Ref. 52, we redefine the grand potential and use

$$\begin{aligned} \Omega'(T, \mu, B) &= \Omega(T, \mu, B) + S\mu \int d\epsilon \rho_h(\epsilon) \\ &= \Omega_e(T, \mu, B) + \Omega_h(T, \mu, B) + \Omega_0(B), \end{aligned} \quad (2.42)$$

where

$$\Omega_0(B) = S \int d\epsilon \rho_h(\epsilon) \epsilon \quad (2.43)$$

is the ground-state/vacuum energy. The carrier imbalance is then given by $N = -[\partial\Omega'(T, \mu, B)/\partial\mu]$.

The magnetization (as a function of the chemical potential, the temperature, and the magnetic field) can be extracted from $\Omega'(T, \mu, B)$ via

$$\begin{aligned} M_{\text{tot}}(T, \mu, B) &= -\frac{1}{S} \frac{\partial \Omega'(T, \mu, B)}{\partial B} \\ &= M_0(B) + M(T, \mu, B), \end{aligned} \quad (2.44)$$

where we have split the magnetization in the vacuum part

$$M_0(B) = -\frac{1}{S} \frac{\partial \Omega_0(B)}{\partial B} \quad (2.45)$$

and the non-vacuum part

$$M(T, \mu, B) = -\frac{1}{S} \left[\frac{\partial \Omega_e(T, \mu, B)}{\partial B} + \frac{\partial \Omega_h(T, \mu, B)}{\partial B} \right]. \quad (2.46)$$

At zero temperature, the magnetization of an undoped system is given by $M_0(B)$, whereas at finite temperatures or in doped systems an additional contribution arises, namely $M(T, \mu, B)$. The magnetization as a function of the carrier imbalance density $n_d = N/S$ ($n_d > 0$: n -doped, $n_d < 0$: p -doped) is given by $M[T, \mu(T, n_d, B), B]$, where the chemical potential is determined by

$$n_d = -\frac{1}{S} \left[\frac{\partial \Omega'(T, \mu, B)}{\partial \mu} \right] \bigg|_{\mu=\mu(T, n_d, B)}. \quad (2.47)$$

Finally, we remark that the magnetic susceptibility $\chi_{\text{tot}}(T, \mu, B) = \chi_0(B) + \chi(T, \mu, B)$ can also be split in the vacuum part

$$\chi_0(B) = \frac{\partial M_0(B)}{\partial B} = -\frac{1}{S} \frac{\partial^2 \Omega_0(B)}{\partial B^2} \quad (2.48)$$

and the non-vacuum part

$$\begin{aligned} \chi(T, \mu, B) &= \frac{\partial M_e(T, \mu, B)}{\partial B} + \frac{\partial M_h(T, \mu, B)}{\partial B} \\ &= -\frac{1}{S} \left[\frac{\partial^2 \Omega_e(T, \mu, B)}{\partial B^2} + \frac{\partial^2 \Omega_h(T, \mu, B)}{\partial B^2} \right]. \end{aligned} \quad (2.49)$$

For the (bulk) Landau levels (and typical parameters of HgTe quantum wells), the different contributions to the grand potential read as

$$\begin{aligned} \Omega_e(T, \mu, B) &= -\frac{SB}{\beta \Phi_0} \left\{ \ln \left[1 + e^{-\beta(E^\uparrow(0) - \mu)} \right] \Theta[E^\uparrow(0) - E^\downarrow(0)] \right. \\ &\quad + \ln \left[1 + e^{-\beta(E^\downarrow(0) - \mu)} \right] \Theta[E^\downarrow(0) - E^\uparrow(0)] \\ &\quad \left. + \sum_{n=1}^{\infty} \sum_{s=\uparrow, \downarrow} \ln \left[1 + e^{-\beta(E_+^s(n) - \mu)} \right] \right\}, \end{aligned} \quad (2.50)$$

2. Magnetic properties of HgTe quantum wells

$$\begin{aligned} \Omega_h(T, \mu, B) = & -\frac{SB}{\beta\Phi_0} \left\{ \ln \left[1 + e^{\beta(E^\downarrow(0) - \mu)} \right] \Theta[E^\uparrow(0) - E^\downarrow(0)] \right. \\ & + \ln \left[1 + e^{\beta(E^\uparrow(0) - \mu)} \right] \Theta[E^\downarrow(0) - E^\uparrow(0)] \\ & \left. + \sum_{n=1}^{\infty} \sum_{s=\uparrow, \downarrow} \ln \left[1 + e^{\beta(E^s_-(n) - \mu)} \right] \right\}, \end{aligned} \quad (2.51)$$

and

$$\Omega_0(B) = \Omega_{\text{dis}}(B) + \tilde{\Omega}_0(B), \quad (2.52)$$

where the energies are given by Eqs. (2.27)-(2.30) and $\Phi_0 = 2\pi\hbar/e$ is the magnetic flux quantum. In Eq. (2.52), we have split the ground-state potential into a contribution from the uppermost valence band [which may not be continuously differentiable if there is a crossover between the hole-like $E^\downarrow(0)$ and the electron-like $E^\uparrow(0)$ bands like at the transition point in Fig. 2.9],

$$\Omega_{\text{dis}}(B) = E^\downarrow(0)\Theta[E^\uparrow(0) - E^\downarrow(0)] + E^\uparrow(0)\Theta[E^\downarrow(0) - E^\uparrow(0)], \quad (2.53)$$

and a contribution from the remaining valence bands,

$$\tilde{\Omega}_0(B) = \sum_{n=1}^{\infty} \sum_{s=\uparrow, \downarrow} E^s_-(n). \quad (2.54)$$

Since the energies in Eq. (2.54) are not bounded from below (for typical parameters of HgTe quantum wells), the sum is divergent; following Refs. 53-55, we introduce a smooth cutoff function which results in a smooth $\tilde{\Omega}_0(B)$ (we refer to the Appendix C for more details). If there is no crossover between the electron-like $E^\uparrow(0)$ band and the hole-like $E^\downarrow(0)$ band, that is, if one deals with an ordinary insulator, then the total ground-state magnetization $M_0(B)$ is continuous. Due to $\Omega_{\text{dis}}(B)$, which is not continuously differentiable if the $E^\uparrow(0)$ and $E^\downarrow(0)$ bands cross (see Fig. 2.9), the ground-state magnetization is not continuous at the crossover point in this case. For bulk Landau levels, we find the jumps

$$\Delta M_0 = \lim_{\delta B \rightarrow 0} [M_0(B_c + \delta B) - M_0(B_c - \delta B)] = -\frac{2\mathcal{M}}{\Phi_0} \quad (2.55)$$

at the crossover point B_c , where there is a transition from the inverted [$E^\uparrow(0) < E^\downarrow(0)$] to the normal regime [$E^\downarrow(0) < E^\uparrow(0)$].

However, at finite temperatures or doping, the total magnetization is given by the sum of the ground-state magnetization $M_0(B)$ and the contribution from the electrons and holes, $M(T, \mu, B)$. Analyzing this contribution for the case of a transition from the inverted to the normal band structure, one finds that $M(T, \mu, B)$ vanishes for zero temperature and zero doping, but otherwise always contains a discontinuity at

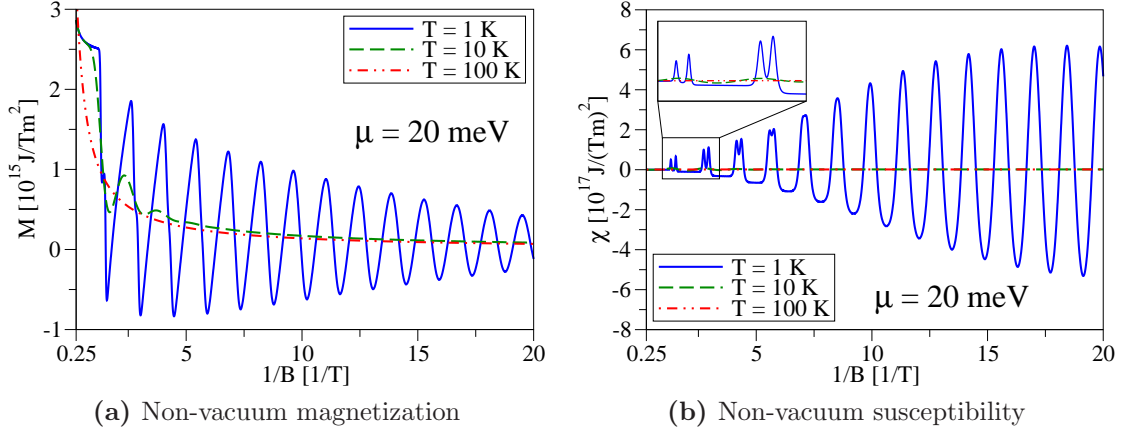


Figure 2.12.: The non-vacuum (a) magnetization $M(T, \mu, B)$ and (b) susceptibility $\chi(T, \mu, B)$ corresponding to a quantum-well thickness of $d = 7.0$ nm plotted versus $1/B$ for a fixed chemical potential $\mu = 20$ meV and different temperatures ($T = 1, 10, 100$ K).

B_c which exactly cancels the discontinuity of the intrinsic magnetization. Thus, the total magnetization is a continuous function. If there is no transition between the normal and inverted band structures, the non-vacuum contribution and therefore the total magnetization are also continuous. For a given quantum-well thickness d , the vacuum contribution $M_0(B)$ constitutes the same background for every set of thermodynamic variables (μ, T) or (n_d, T) of the system. Thus, the quantity of interest which allows one to compare different doping levels, chemical potentials or temperatures of the system is the non-vacuum contribution $M(T, \mu, B)$.

Equations (2.45)-(2.52) allow us to calculate the (bulk) magnetization and susceptibility of HgTe quantum wells, the results of which are discussed in the following section.

2.3.2. Results

In this section, we apply the formalism introduced above to calculate the bulk magnetization of HgTe for the parameter set corresponding to a quantum-well thickness of $d = 7.0$ nm (nominally the QSH regime; see above), that is, a situation where there is a crossover between the $E^\uparrow(0)$ and $E^\downarrow(0)$ bands. Figure 2.12 shows the magnetic field dependence of the non-vacuum contributions, that is, the contribution arising from electrons and holes, to the magnetization and the susceptibility for a fixed chemical potential, several different temperatures, and magnetic fields well below the crossover point $B_c \approx 7.4$ T (compare to Sec. 2.2.4). As different Landau levels cross the Fermi level with increasing magnetic field, one can observe the de Haas-van Alphen oscillations in the magnetization as well as in the susceptibility

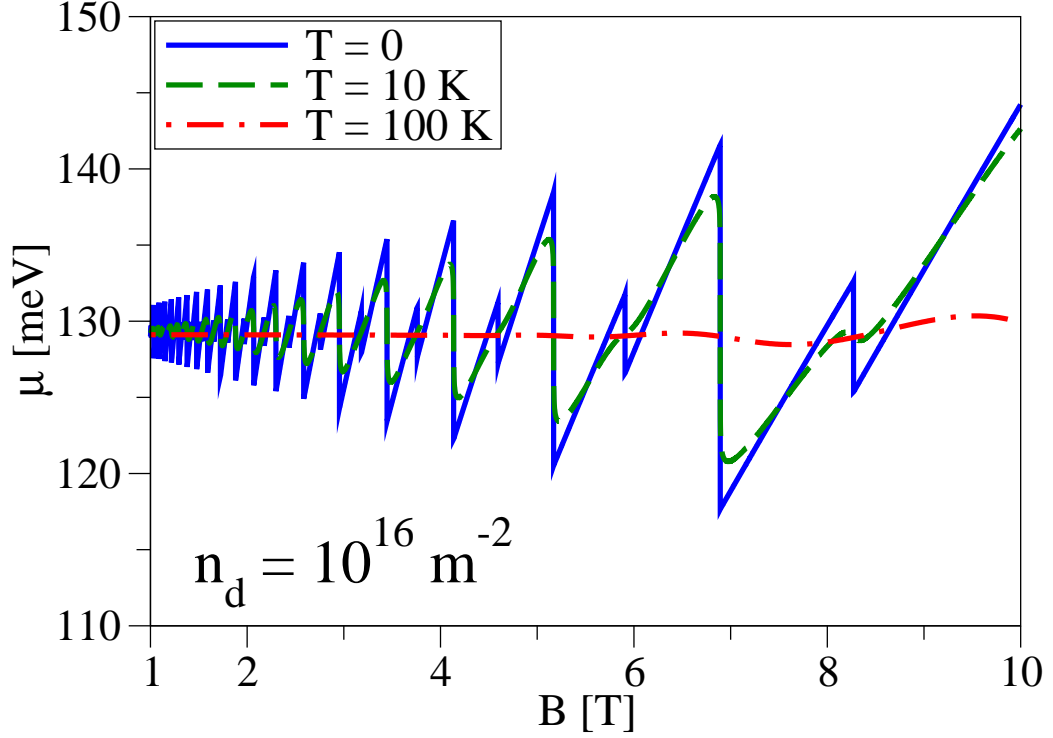


Figure 2.13.: Magnetic field dependence of the chemical potential $\mu(T, n_d, B)$ (corresponding to a quantum-well thickness of $d = 7.0$ nm) for $n_d = 10^{16}$ $1/\text{m}^2$ and different temperatures ($T = 0, 10, 100$ K).

whose amplitude decreases with increasing temperature. For high magnetic fields [see the inset in Fig. 2.12 (b)], the spacing between the energies of spin-up and spin-down Landau levels (with the same quantum number n) is large enough compared to thermal broadening to observe spin-resolved peaks in the susceptibility. Fitting the oscillations of the magnetization to a periodic function, we find that the periodicity of those oscillations is given by $\Delta(1/B) \approx 1.43$ $1/\text{T}$ [see also the Appendix D, where Eq. (D.17) yields a period of $\Delta(1/B) \approx 1.35$ $1/\text{T}$ for the main contribution to the oscillations in the reduced model].

Next, we consider a fixed carrier density $n_d > 0$. The corresponding chemical potential as a function of the magnetic field is calculated via Eq. (2.47) and is displayed in Fig. 2.13 for the density $n_d = 10^{16}$ $1/\text{m}^2$ and different temperatures. With varying magnetic field, the Fermi energy $\mu(0, n_d, B)$ shows oscillations consisting of a pair of spin-resolved peaks, where each of those oscillations corresponds to a crossing of a Landau level with the Fermi level. Higher temperatures result in a smoothening of the oscillations and a diminution of their amplitudes. Moreover, thermal broadening leads to a removal of the spin-resolution at small magnetic fields.

Figure 2.14 shows the chemical potential and the combined contribution $M_{\text{dis}}(B) +$

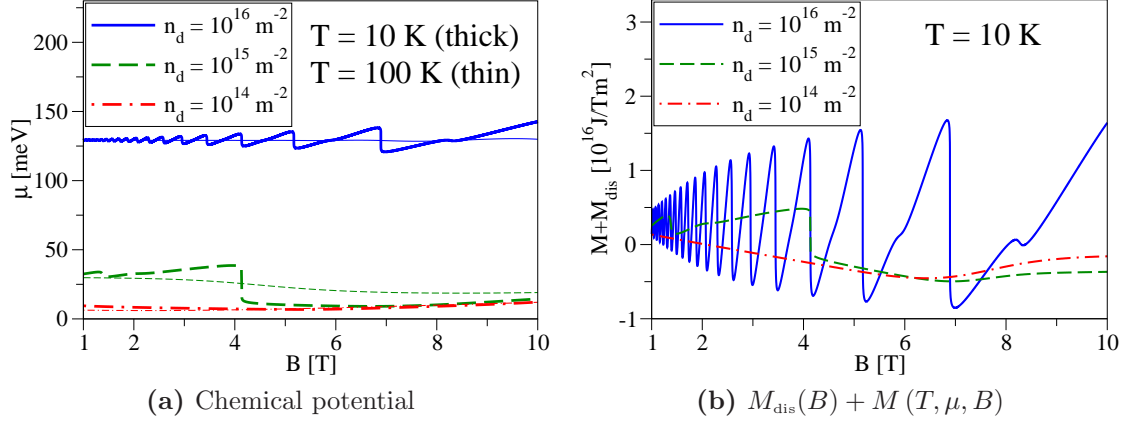


Figure 2.14.: Magnetic field dependence of the (a) chemical potential $\mu(T, n_d, B)$ and of (b) the contribution $M_{\text{dis}}(B) + M(T, \mu, B)$ to the magnetization corresponding to a quantum-well thickness of $d = 7.0$ nm for $T = 10$ K and different densities ($n_d = 10^{14}, 10^{15}, 10^{16} \text{ 1/m}^2$).

$M(T, \mu, B)$ to magnetization as functions of the magnetic field for $T = 10$ K and different carrier densities n_d .¹ As above, one can see the de Haas-van Alphen oscillations in the magnetization [see Fig. 2.14 (b)], which—for fixed carrier densities—follow the oscillations in the chemical potential [see Fig. 2.14 (a)]. At low densities, on the other hand, only the lowest conduction Landau level is occupied and the chemical potential roughly follows this level and there are consequently no oscillations.

For the sake of comparison to the situation in the inverted regime discussed so far, Fig. 2.15 show the magnetic field dependence of the non-vacuum contributions to the magnetization and the susceptibility in the normal regime (corresponding to the parameters for a quantum-well thickness of $d = 5.5$ nm as in Sec. 2.2.4) for a fixed chemical potential and several different temperatures. As in Fig. 2.12, one can observe the de Haas-van Alphen oscillations. No discernible features are seen when comparing the inverted and normal regimes in the bulk.

In limiting cases, compact analytical formulas to describe some of the main features of the magnetization and the susceptibility shown above can be given for the reduced model and are presented in the Appendix D.

¹Here, we have added the discontinuous contribution from the ground-state magnetization, $M_{\text{dis}}(B) = -(1/S)[\partial\Omega_{\text{dis}}(B)/\partial B]$, to the non-vacuum magnetization in order that the discontinuity at $B = B_c$ be canceled.

2. Magnetic properties of HgTe quantum wells

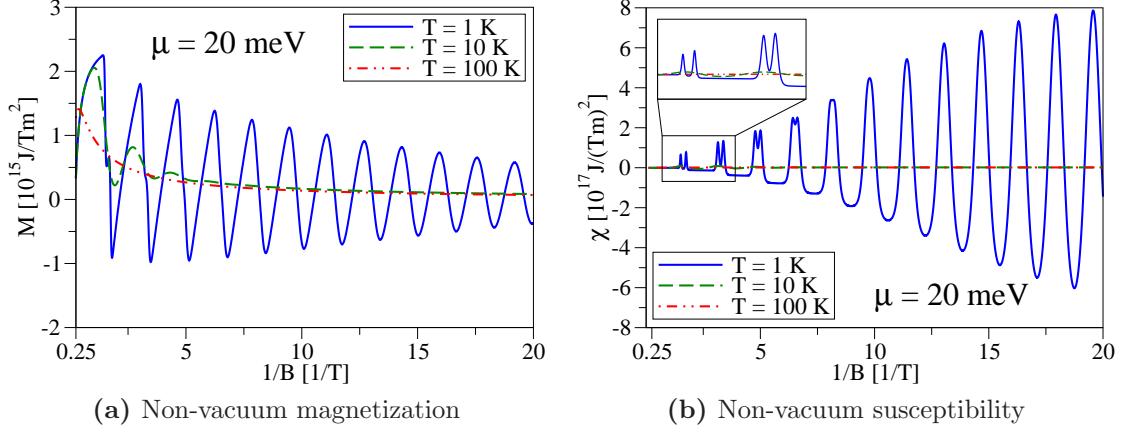


Figure 2.15.: The non-vacuum (a) magnetization $M(T, \mu, B)$ and (b) susceptibility $\chi(T, \mu, B)$ corresponding to a quantum-well thickness of $d = 5.5$ nm plotted versus $1/B$ for a fixed chemical potential $\mu = 20$ meV and different temperatures ($T = 1, 10, 100$ K).

2.4. Magneto-optical conductivity

2.4.1. General formalism

In this section, we compute the (bulk) magneto-optical conductivity of a HgTe quantum well described by the effective Hamiltonian (2.4), that is, of a 2D system without any confinement (in the xy -plane). As a first step, we calculate the (charge) current

$$\mathbf{I} = -e \int dx dy \mathbf{j}_e(x, y), \quad (2.56)$$

where the current density is given by Eq. (E.5) in the Appendix E.² By promoting the wave functions in Eq. (E.5) to field operators, using the bulk Landau states given in the Appendix B as a basis, and computing the integrals over the position, one can write the current operator as

$$\hat{\mathbf{I}} = -e \sum_{n,k,s\lambda,\lambda'} \mathbf{d}_{\lambda\lambda'}^s(n) \hat{c}_{nk\lambda s}^\dagger \hat{c}_{n+1,k\lambda' s} + \text{h.c.}, \quad (2.57)$$

where n refers to the Landau level, k to the momentum in x -direction, s to the spin quantum number, and λ and λ' to the conduction ($\lambda = +$) or valence bands ($\lambda = -$). Here and in the following, the sum over the Landau levels n and the band labels

²Here, the vector potential $\mathbf{A}(\mathbf{r})$ from Eq. (2.3) has to be inserted into Eq. (E.5) to describe the presence of a static magnetic field perpendicular to the quantum-well plane. Moreover, we have omitted the contribution from the internal current density $\mathbf{j}_i(x, y)$ given by Eq. (E.6), which is small compared to the external current density.

2.4. Magneto-optical conductivity

λ and λ' should be understood in the sense that for $n = 0$, the summation over λ (but not λ') is omitted because for each spin species, there is only one zero mode (see Sec. 2.2.1 and the Appendix B). The components of the dipole-matrix elements $\mathbf{d}_{\lambda\lambda'}^s(n)$ are given by $d_{\lambda\lambda'}^{s,x}(n) = d_{\lambda\lambda'}^s(n)$ and $d_{\lambda\lambda'}^{s,y}(n) = i d_{\lambda\lambda'}^s(n)$, where

$$d_{\lambda\lambda'}^\uparrow(n) = \frac{2(\mathcal{D} + \mathcal{B})}{\hbar l_B} \sqrt{\frac{n+1}{2}} v_{n\lambda}^\uparrow v_{n+1,\lambda'}^\uparrow + \frac{2(\mathcal{D} - \mathcal{B})}{\hbar l_B} \sqrt{\frac{n}{2}} u_{n\lambda}^\uparrow u_{n+1,\lambda'}^\uparrow + \frac{\mathcal{A}}{\hbar} v_{n\lambda}^\uparrow u_{n+1,\lambda'}^\uparrow \quad (2.58)$$

and

$$d_{\lambda\lambda'}^\downarrow(n) = \frac{2(\mathcal{D} + \mathcal{B})}{\hbar l_B} \sqrt{\frac{n}{2}} v_{n\lambda}^\downarrow v_{n+1,\lambda'}^\downarrow + \frac{2(\mathcal{D} - \mathcal{B})}{\hbar l_B} \sqrt{\frac{n+1}{2}} u_{n\lambda}^\downarrow u_{n+1,\lambda'}^\downarrow - \frac{\mathcal{A}}{\hbar} u_{n\lambda}^\downarrow v_{n+1,\lambda'}^\downarrow \quad (2.59)$$

for $n \geq 1$ and

$$d_{\lambda'}^\uparrow(0) = \frac{2(\mathcal{D} + \mathcal{B})}{\hbar l_B} \sqrt{\frac{1}{2}} v_{1\lambda'}^\uparrow + \frac{\mathcal{A}}{\hbar} u_{1\lambda'}^\uparrow \quad (2.60)$$

and

$$d_{\lambda'}^\downarrow(0) = \frac{2(\mathcal{D} - \mathcal{B})}{\hbar l_B} \sqrt{\frac{1}{2}} u_{1\lambda'}^\downarrow - \frac{\mathcal{A}}{\hbar} v_{1\lambda'}^\downarrow \quad (2.61)$$

for $n = 0$. Here, $v_{n\lambda}^\uparrow$, $u_{n\lambda}^\uparrow$, $v_{n\lambda}^\downarrow$, and $u_{n\lambda}^\downarrow$ are given by Eqs. (B.4) and (B.8) in the Appendix B.

Having determined an expression for the (paramagnetic) current operator, we next derive a Kubo formula for the magneto-optical conductivity. If a uniform electric field $\mathbf{E}(t)$ is applied to the system governed by Eq. (2.4), the effect of this external field can be described by including the additional vector potential $\mathbf{A}_{\text{ext}}(t)$ with $\mathbf{E}(t) = -\frac{\partial \mathbf{A}_{\text{ext}}(t)}{\partial t}$. In this situation, the total Hamiltonian of the system can be written as $\hat{H} + \hat{H}_{\text{ext}}(t)$, with \hat{H} being given by Eq. (2.4) and the perturbation by

$$\hat{H}_{\text{ext}}(t) = e \int dx dy \hat{\mathbf{j}}_e(x, y) \cdot \mathbf{A}_{\text{ext}}(t) = -\hat{\mathbf{I}} \cdot \mathbf{A}_{\text{ext}}(t). \quad (2.62)$$

Applying the theory of linear response [56, 57, 58] and conducting a Fourier transformation, we find that the nonequilibrium current density $\delta \langle \hat{I}_\alpha(\omega) \rangle / S$ in the presence of the external perturbation $\hat{H}_{\text{ext}}(t)$ reads as

$$\frac{1}{S} \delta \langle \hat{I}_\alpha(\omega) \rangle = i \sum_\beta \frac{\Pi_{\alpha\beta}^R(\omega)}{S \hbar \omega} E_\beta(\omega), \quad (2.63)$$

where S denotes the surface area of the 2D HgTe system and α and β refer to the x - and y -coordinates. Moreover, we have introduced the retarded current-current correlation function $\Pi_{\alpha\beta}^R(\omega)$, which can be determined from the imaginary-time correlation

2. Magnetic properties of HgTe quantum wells

function

$$\Pi_{\alpha\beta}(i\omega_n) = - \int_0^{\hbar\beta} d\tau \left\langle \mathcal{T} \left[\hat{I}_\alpha(\tau) \hat{I}_\beta(0) \right] \right\rangle e^{i\omega_n \tau} \quad (2.64)$$

via the formula $\Pi_{\alpha\beta}^R(\omega) = \Pi_{\alpha\beta}(\omega + i0^+)$ [56, 57, 58]. Here, $i\omega_n$ denotes a bosonic frequency, τ an imaginary time, \mathcal{T} the imaginary time-ordering operator, $\langle \dots \rangle$ the thermal average, and $\beta = 1/(k_B T)$. The (real part of the) magneto-optical conductivity can be extracted from Eq. (2.63) and reads as³

$$\sigma_{\alpha\beta}(\omega) = \text{Re} \left[\frac{i\Pi_{\alpha\beta}^R(\omega)}{S\hbar\omega} \right] = - \frac{\text{Im} [\Pi_{\alpha\beta}^R(\omega)]}{S\hbar\omega}. \quad (2.65)$$

Hence, we are left with the calculation of the retarded current-current correlation function, which can be determined from Eq. (2.64). In this section, we investigate a simple model: We assume that scattering by impurities can be described by a constant, phenomenological scattering rate Γ_{br}/\hbar and do not consider any other processes such as, for example, electron-phonon coupling. Next, we introduce the spectral function, which in the case considered here is given by

$$\mathcal{A}_{n\lambda s}(\omega) = \frac{2\hbar\Gamma_{\text{br}}}{[\hbar\omega - E_\lambda^s(n) + \mu]^2 + \Gamma_{\text{br}}^2}, \quad (2.66)$$

where the (bulk) Landau levels $E_\lambda^s(n)$ are given by Eqs. (2.27) and (2.29) for $n \geq 1$ and by Eqs. (2.28) and (2.30) for $n = 0$.⁴ Furthermore, we note that Eq. (2.66) does not depend on k because the Landau levels are k -independent, as is Γ_{br} in our model. If we ignore vertex corrections in Eq. (2.64), express the Green's functions in the resulting equation with the help of the spectral function (2.66), and calculate the sum over bosonic frequencies, we obtain the real parts of the magneto-optical conductivity tensor

$$\begin{aligned} \sigma_{xx}(\omega) = \sigma_{yy}(\omega) = \frac{e^2}{8\pi^2\hbar\omega l_B^2} \left\{ \sum_{n,\lambda,\lambda',s} [d_{\lambda\lambda'}^s(n)]^2 \int d\omega' [n_F(\hbar\omega') - n_F(\hbar\omega' + \hbar\omega)] \right. \\ \left. \times [\mathcal{A}_{n\lambda s}(\omega)\mathcal{A}_{n+1,\lambda's}(\omega + \omega') + \mathcal{A}_{n\lambda s}(\omega + \omega')\mathcal{A}_{n+1,\lambda's}(\omega)] \right\} \end{aligned} \quad (2.67)$$

³Strictly speaking, there would also be a diamagnetic contribution to the magneto-optical conductivity, not just the paramagnetic contribution considered here. However, this contribution is purely imaginary and, since we are only interested in the real part of the magneto-optical conductivity, we have omitted the diamagnetic contribution for the sake of brevity.

⁴In the case $n = 0$, there is also no dependence on the band index because there is only one Landau level with $n = 0$ for a given spin.

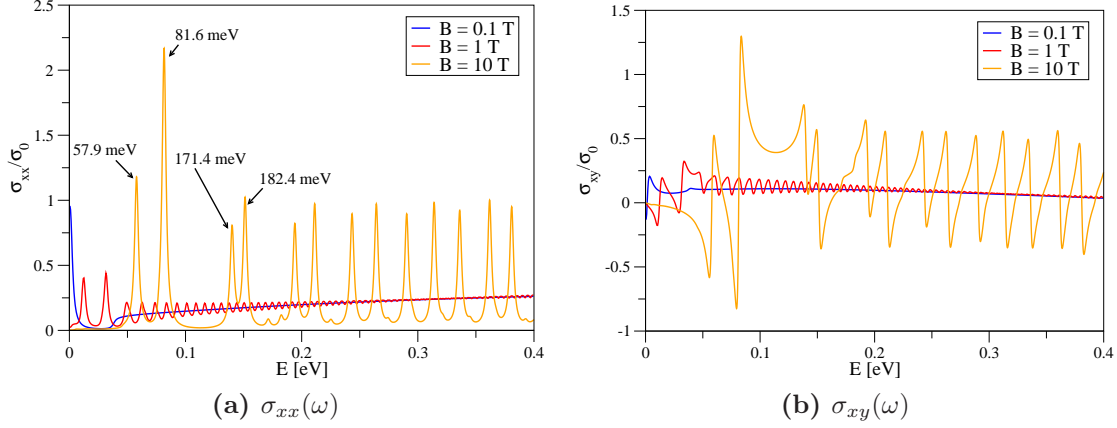


Figure 2.16.: Real parts of the (a) longitudinal magneto-optical and (b) optical Hall conductivities in a HgTe quantum well (corresponding to a quantum-well thickness of $d = 7.0$ nm) plotted versus $E = \hbar\omega$ for a fixed temperature $T = 1$ K, chemical potential $\mu = 20$ meV, broadening $\Gamma_{\text{br}} = 1$ meV, and different magnetic fields ($B = 0.1, 1, 10$ T). The peaks at $\hbar\omega \approx 57.9$ meV and $\hbar\omega \approx 81.6$ meV originate from the transitions $(n = 0, s = \downarrow) \rightarrow (n = 1, s = \downarrow, \lambda = +)$ and $(n = 0, s = \uparrow) \rightarrow (n = 1, s = \uparrow, \lambda = +)$, respectively. The transitions $(n = 2, s = \downarrow, \lambda = -) \rightarrow (n = 1, s = \downarrow, \lambda = +)$ and $(n = 2, s = \uparrow, \lambda = -) \rightarrow (n = 1, s = \uparrow, \lambda = +)$ correspond to the pair of peaks at $\hbar\omega \approx 171.4$ meV and $\hbar\omega \approx 182.4$ meV.

and

$$\begin{aligned} \sigma_{xy}(\omega) = -\sigma_{yx}(\omega) = & \frac{e^2}{8\pi^3 \hbar \omega l_B^2} \left\{ \sum_{n, \lambda, \lambda', s} [d_{\lambda\lambda'}^s(n)]^2 \int d\omega' d\omega'' [n_F(\hbar\omega') - n_F(\hbar\omega'')] \right. \\ & \times \mathcal{A}_{n\lambda s}(\omega') \mathcal{A}_{n+1, \lambda' s}(\omega'') \left[\mathcal{P} \frac{1}{\omega' - \omega'' + \omega} - \mathcal{P} \frac{1}{\omega' - \omega'' - \omega} \right] \Big\}, \end{aligned} \quad (2.68)$$

where $n_F(\epsilon) = 1/[\exp(\beta\epsilon) + 1]$ with $\beta = 1/(k_B T)$ (see Refs. 56, 57, 58 for more details on the derivation of this formulas). The imaginary parts of the magneto-optical conductivity (without the diamagnetic contribution) can be derived either from $\text{Re} [\Pi_{\alpha\beta}^R(\omega)] / (S\hbar\omega)$ or from applying Kramers-Kronig relations on Eqs. (2.67) and (2.68). In fact, in our numerical calculations, $\sigma_{xy}(\omega)$ is calculated by first computing the imaginary part of the off-diagonal component of the magneto-optical conductivity tensor, which is given by an expression very similar to Eq. (2.67), and using a Kramers-Kronig relation subsequently.

Finally, Eqs. (2.67) and (2.68) also make it clear that—in the lowest order—only transitions between neighboring Landau levels, that is, transitions from n to $n \pm 1$, are permitted. Furthermore, the spin has to be preserved during this transition.

2. Magnetic properties of HgTe quantum wells

Hence, transitions are governed by the selection rules⁵

$$(n, s, \lambda) \rightarrow (n \pm 1, s, \lambda'). \quad (2.69)$$

Here, the only restriction on λ and λ' is that, at low temperatures, the transition has to occur from an occupied band, that is, a band below the Fermi level, to an unoccupied band, that is, a band above the Fermi level.

2.4.2. Results

In the following, we briefly discuss results obtained numerically for the magneto-optical conductivities derived in the previous section, Eqs. (2.67) and (2.68), for parameters corresponding to a quantum-well thickness $d = 7.0$ nm, that is, the QSH regime. (Unless explicitly stated otherwise, the parameters for $d = 7.0$ nm are used throughout this section). The integrals over the frequencies have been calculated on a discrete 1D grid with $\Delta(\hbar\omega) = 0.5$ meV.

Figure 2.16 shows the magneto-optical conductivities for different magnetic fields and a fixed temperature $T = 1$ K, chemical potential $\mu = 20$ meV, and broadening $\Gamma_{\text{br}} = 1$ meV as a function of the frequency. (Here and in the following, the magneto-optical conductivity is given in units of $\sigma_0 = e^2/\hbar$.) For the case of $B = 10$ T, one can observe peaks in σ_{xx} [see Fig. 2.16 (a)] that correspond to transitions between occupied and unoccupied Landau levels. At this magnetic field, the first (and most pronounced) pair of peaks originates from the transitions $(n = 0, s = \downarrow) \rightarrow (n = 1, s = \downarrow, \lambda = +)$ and $(n = 0, s = \uparrow) \rightarrow (n = 1, s = \uparrow, \lambda = +)$, respectively. As far as the remaining peaks are concerned, one can distinguish between two different types of peaks: On the one hand, one can find pronounced peaks (such as, for example, the pair of peaks at $\hbar\omega \approx 140.1$ meV and $\hbar\omega \approx 151.3$ meV) which correspond to transitions $(n, s, \lambda = -) \rightarrow (n - 1, s, \lambda = +)$ with $n \geq 2$. Besides those peaks, on the other hand, there are also much less pronounced peaks (such as, for example, the pair of peaks at $\hbar\omega \approx 171.4$ meV and $\hbar\omega \approx 182.4$ meV) which arise due to transitions $(n, s, \lambda = -) \rightarrow (n + 1, s, \lambda = +)$ with $n \geq 1$. The real part of the off-diagonal magneto-optical conductivity σ_{xy} at $B = 10$ T vanishes for zero frequency and exhibits an oscillatory behavior at higher frequencies as can be discerned from Fig. 2.16 (b).

If the strength of the magnetic field is reduced to $B = 1$ T, the peaks in σ_{xx} as well as the amplitudes of the oscillations in σ_{xy} diminish. Moreover, since the spacing between neighboring Landau levels at $B = 1$ T is smaller than that for $B = 10$ T, the resolution of the peaks originating from transitions between the different Landau

⁵In addition to the selection rules for n and s , the momentum in x -direction k has also to be preserved during the transition. Since the bulk Landau levels do not depend on k , this circumstance cannot be seen explicitly in Eqs. (2.67) and (2.68), but can be discerned from looking at the contractions that occur in $\langle \mathcal{T}[\hat{I}_\alpha(\tau)\hat{I}_\beta(0)] \rangle$.

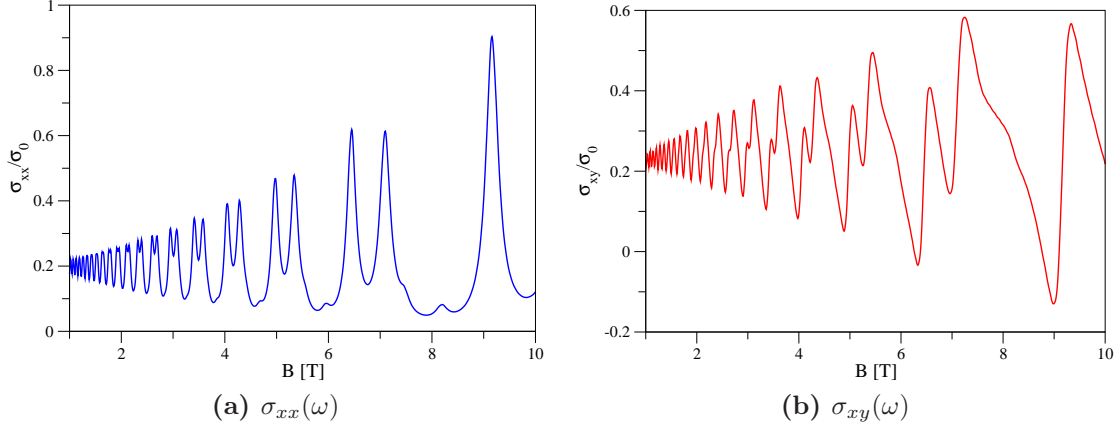


Figure 2.17.: Real parts of the (a) longitudinal magneto-optical and (b) optical Hall conductivities in a HgTe quantum well (corresponding to a quantum-well thickness of $d = 7.0$ nm) plotted versus B for a fixed temperature $T = 1$ K, chemical potential $\mu = 100$ meV, broadening $\Gamma_{\text{br}} = 1$ meV, and $\hbar\omega = 200$ meV.

levels is no longer as sharp as for $B = 10$ T and the behavior of σ_{xx} for higher frequencies ($\hbar\omega \gtrsim 50$ meV) can better be described as oscillating around a residue value determined by the impurity broadening Γ_{br} [see Fig. 2.16 (a)]. At $B = 1$ T, one can also more clearly see that the amplitudes of the oscillations in both σ_{xx} and σ_{xy} decrease with increasing frequencies.

If the magnetic field is eventually reduced further to $B = 0.1$ T, the impurity broadening Γ_{br} is so large compared to the spacing between neighboring Landau levels that—apart from a peak at $\hbar\omega = 0$ —one can no longer observe any peaks or oscillations at finite frequencies in σ_{xx} [see Fig. 2.16 (a)]. The behavior of σ_{xx} at $B = 0.1$ T already exhibits the main properties one can expect of the optical conductivity σ_{xx} at zero magnetic field: There is a Drude peak at zero frequency, after which σ_{xx} tends to zero, and there is a gap of approximately $2|\mu|$ in the absorption spectrum.⁶ The (real parts of the) off-diagonal elements of the magneto-optical conductivity also no longer exhibit any oscillations as can be seen in Fig. 2.16 (b).

Figure 2.17 shows the magneto-optical conductivity as a function of the magnetic field for a fixed frequency $\hbar\omega = 200$ meV as well as for a fixed temperature, chemical potential, and broadening. Similar to their frequency dependence, with varying magnetic field, σ_{xx} and σ_{xy} exhibit pronounced peaks and oscillations, respectively. The height of the peaks in σ_{xx} as well as the amplitude of the oscillations in σ_{xy} increases with increasing magnetic field. While for low magnetic fields, one can only identify the peaks of transitions $(n, s, \lambda = -) \rightarrow (n - 1, s, \lambda = +)$ with $n \geq 2$, for higher

⁶The statement that there is a gap of $2|\mu|$ in the absorption spectrum holds only for $|\mu| > |\mathcal{M}|$. If $|\mu| < |\mathcal{M}|$, the width of the gap in the absorption spectrum would be $2|\mathcal{M}|$ at zero magnetic field.

2. Magnetic properties of HgTe quantum wells

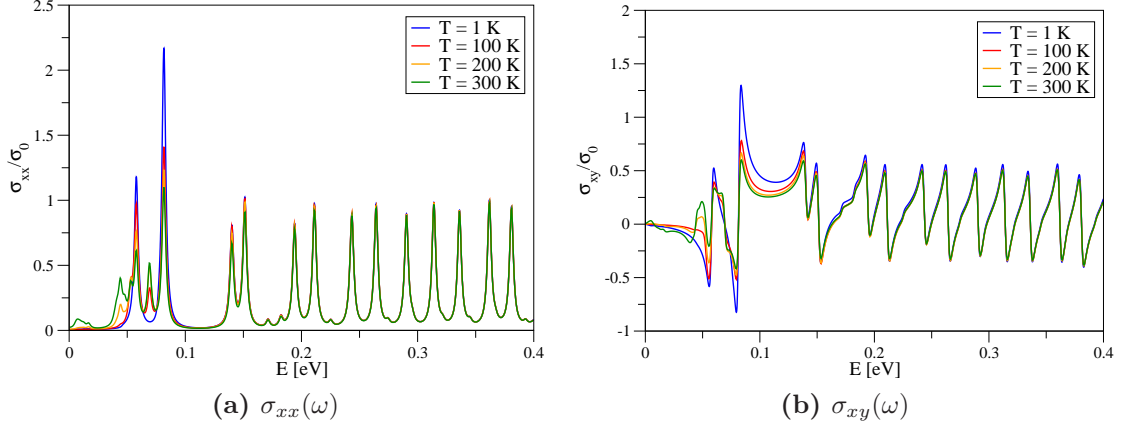


Figure 2.18.: Real parts of the (a) longitudinal magneto-optical and (b) optical Hall conductivities in a HgTe quantum well (corresponding to a quantum-well thickness of $d = 7.0$ nm) plotted versus $E = \hbar\omega$ for a fixed magnetic field $B = 10$ T, chemical potential $\mu = 20$ meV, broadening $\Gamma_{br} = 1$ meV, and different temperatures ($T = 1, 100, 200, 300$ K).

magnetic fields, $B \gtrsim 4$ T, one can also find less pronounced peaks which correspond to transitions $(n, s, \lambda = -) \rightarrow (n + 1, s, \lambda = +)$ with $n \geq 1$ (see above).

The temperature dependence of the magneto-optical conductivity is illustrated in Fig. 2.18, which shows σ_{xx} [Fig. 2.18 (a)] and σ_{xy} [Fig. 2.18 (b)] as functions of the frequency for a fixed magnetic field, chemical potential, and broadening. The main feature observed in Fig. 2.18 is that with increasing temperature, additional transitions become possible (or better: more probable) which then give rise to new peaks—mainly at low frequencies. For higher frequencies, on the other hand, the magneto-optical conductivity remains largely unaffected, although the peaks and oscillations are slightly reduced.

In Fig. 2.19, the dependence of the magneto-optical conductivity on the chemical potential is displayed for n -doped quantum wells. As can be seen in Fig. 2.19 (a), at low frequencies and for large chemical potentials, σ_{xx} has a huge peak, whose height increases with increasing chemical potential and which originates from transitions near the Fermi level. With increasing frequency, the magneto-optical conductivity tends to zero as there are no transitions possible from the valence to the conduction Landau levels for those energies. Only if the energy is beyond a certain value, namely the energy of the first allowed transition (see the selection rules at the end of Sec. 2.4.1) whose energy exceeds 2μ , can a non-vanishing magneto-optical conductivity σ_{xx} be observed (for low temperatures). For frequencies above this threshold value, σ_{xx} exhibits exactly the same behavior as the magneto-optical conductivity σ_{xx} at lower chemical potentials because at these energies, the same transitions can also occur for any lower chemical potential.

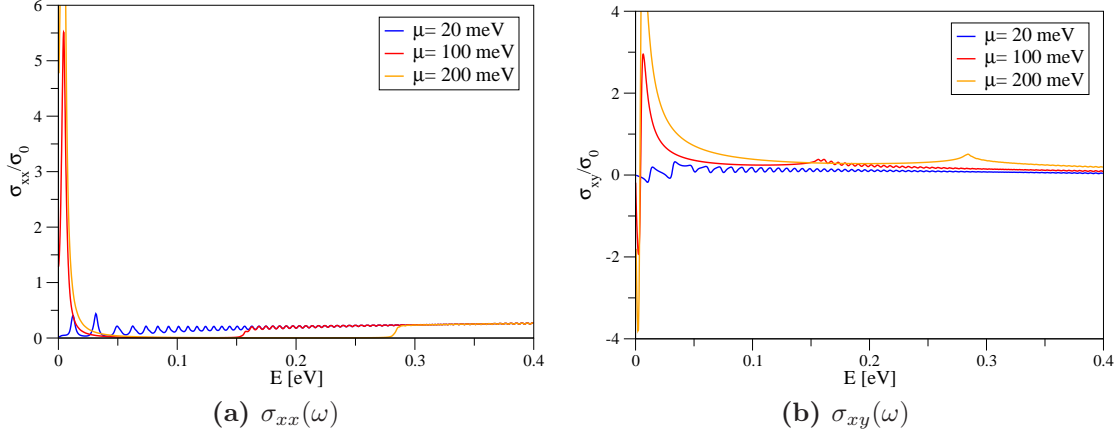


Figure 2.19.: Real parts of the (a) longitudinal magneto-optical and (b) optical Hall conductivities in a HgTe quantum well (corresponding to a quantum-well thickness of $d = 7.0$ nm) plotted versus $E = \hbar\omega$ for a fixed temperature $T = 1$ K, magnetic field $B = 1$ T, broadening $\Gamma_{\text{br}} = 1$ meV, and different chemical potentials ($\mu = 20, 100, 200$ meV).

Having studied the parameters corresponding to the QSH regime, we conclude this section with the remark that the same qualitative behavior as discussed above can also be found for the regime of ordinary insulators, that is, $d < d_c \approx 6.3$ nm. For comparison, Fig. 2.20 shows the (real part of the) magneto-optical conductivity as a function of the frequency for the same magnetic fields, chemical potential, impurity broadening, and temperature as in Fig. 2.16, but for a quantum-well thickness $d = 5.5$ nm.

2.5. Conclusions

We have derived analytical formulas to calculate the energy spectra of HgTe quantum wells in infinite, semi-infinite, and finite-strip systems in the presence of perpendicular magnetic fields and hard walls. Complementary to the analytical formulas, we have also used a finite-difference scheme to investigate the magnetic field dependence of the energy spectra and their respective eigenstates in a finite-strip geometry for parameters corresponding to the normal ($d < d_c$), inverted ($d > d_c$), and critical regimes ($d \approx d_c$). In the inverted regime ($d > d_c$), we found that for magnetic fields below the crossover point between the uppermost (electron-like) valence and lowest (hole-like) conduction Landau levels, one can still observe counterpropagating, spin-polarized states at finite magnetic fields, although these states are no longer protected by time-reversal symmetry. Above the crossover point, the band structure becomes normal and one can no longer find those states. This situation is similar for parameters corresponding to the normal regime ($d < d_c$), where one cannot find

2. Magnetic properties of HgTe quantum wells

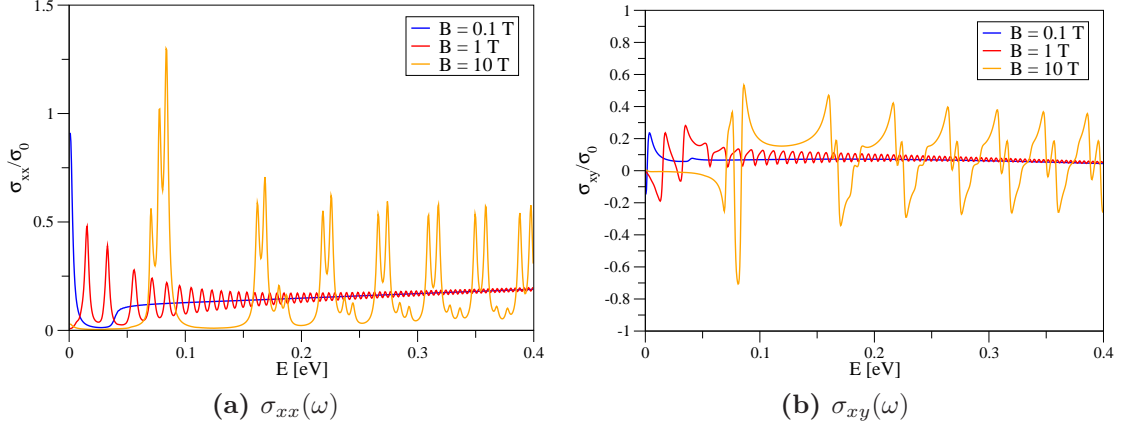


Figure 2.20.: Real parts of the (a) longitudinal magneto-optical and (b) optical Hall conductivities in a HgTe quantum well (corresponding to a quantum-well thickness of $d = 5.5$ nm) plotted versus $E = \hbar\omega$ for a fixed temperature $T = 1$ K, chemical potential $\mu = 20$ meV, broadening $\Gamma_{br} = 1$ meV, and different magnetic fields ($B = 0.1, 1, 10$ T).

counterpropagating, spin-polarized states even for zero or weak magnetic fields. Furthermore, we have studied the bulk magnetization and susceptibility in HgTe quantum wells and have investigated their dependence on the magnetic field, chemical potential, and carrier density. In the case of fixed chemical potentials as well as in the case of fixed densities, the magnetization (for both the normal as well as the inverted regime) exhibits characteristic de Haas-van Alphen oscillations, which in the case of fixed carrier densities follow the oscillations in the chemical potential. Corresponding to those oscillations of the magnetization, one can also observe oscillations in the magnetic susceptibility. With increasing temperature, the amplitude of these oscillations decreases. Furthermore, we found that, if the band structure is inverted, the ground-state magnetization (and consequently also the ground-state susceptibility) is discontinuous at the crossover point between the uppermost valence and lowest conduction Landau levels. At finite temperatures and/or doping, however, this discontinuity is canceled by the contribution from electrons and holes and the total magnetization and susceptibility are continuous. Finally, we have calculated the magneto-optical conductivity for HgTe quantum wells, and have studied its dependence on the magnetic field, chemical potential, and temperature. We have found that for large magnetic fields, when the spacing between neighboring Landau levels is large compared to the lifetime broadening, one can observe pronounced peaks and oscillations in the magneto-optical conductivity, while this structure is smeared out for weak magnetic fields. We, moreover, find that with increasing temperature, additional peaks appear at low frequencies as new transitions become more probable.

3. Optical conductivity of graphene

3.1. Graphene

Since it was first isolated in 2004 [59], graphene, a material which is composed of a single layer of carbon atoms arranged in a 2D honeycomb lattice, has attracted immense attention [1, 2]. Whereas graphene has only recently been observed experimentally, its electronic band structure has been known since the work of Wallace more than 60 years ago [60]. At that time, studies in graphene were intended as a starting point for the calculation of the band structure of graphite, whose electronic properties were described successfully by the Slonczewski-Weiss-McClure model in the following decade [61, 62].

However, with its experimental realization, the focus has shifted to graphene and enormous effort, both experimentally [1] and theoretically [2], has been put into the investigation of this material. One of the main reasons for this interest is that its low-energy excitations can be described by a 2D Dirac-like Hamiltonian of massless fermions with an effective speed of light $v_F \approx 10^6$ m/s, which essentially allows one to study quantum electrodynamics in (2+1) dimensions by studying the electronic properties of graphene [1, 2, 63].

One particular field which has received considerable attention, both experimentally [64, 65, 66, 67] as well as theoretically [68, 69, 70, 71, 72, 73, 74, 75, 76, 77, 78, 79, 80], is the optical (or ac) conductivity in graphene, that is, the frequency-dependent conductivity in the presence of an alternating electric field, the measurement of which can provide valuable information about the dynamics of the charge carriers in graphene. The main feature that can be observed in the optical conductivity is that for frequencies larger than twice the chemical potential μ , the optical conductivity is roughly given by $\sigma_0 = e^2/(4\hbar)$, the so-called universal ac conductivity [64, 65]. For frequencies below 2μ , the optical conductivity is greatly reduced, which can be explained within a single-particle model where transitions induced by photons with energies $\hbar\omega < 2\mu$ are forbidden due to Pauli's exclusion principle (see Fig. 3.1). In experiments, however, one does not observe the optical conductivity to vanish completely, as one would expect from the simple single-particle argument given above. To describe this behavior, mechanisms involving disorder and/or phonons, both of which can account for a finite absorption below 2μ , have been studied the-

3. Optical conductivity of graphene

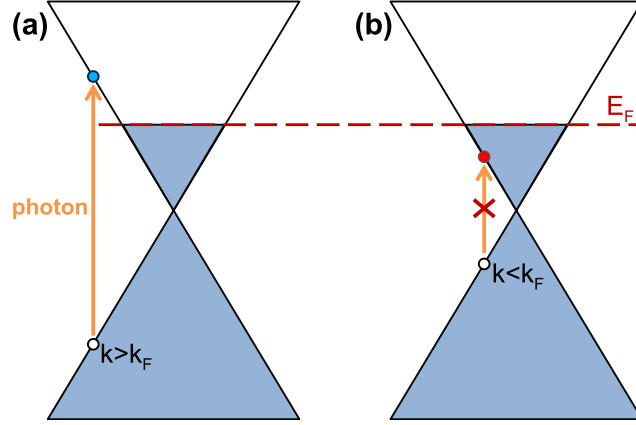


Figure 3.1.: Optical transitions in n -doped graphene if only the electronic single-particle states are considered. Since energy as well as momentum need to be conserved and there is no transfer of momentum from the photon to the electronic system, there can only be vertical transitions. Due to Pauli's exclusion principle, there can, furthermore, only be transitions from occupied to unoccupied states, that is, from states below the Fermi level E_F to states with an energy $E > E_F$. Thus, only transitions with energies larger than $2E_F$ are allowed.

oretically [72, 73, 74, 75, 78]. In addition to these single-electron effects, excitonic effects [79] as well as effects arising from the Coulomb interaction [80] have also been considered.

Closely related, the magneto-optical conductivity, that is, the optical conductivity in the presence of a magnetic field, has also been investigated theoretically if disorder described by a phenomenological scattering rate [81, 82, 83] and coupling between electrons and Einstein phonons [84] are included.

Besides these aforementioned studies on the optical conductivity, the role played by several different phonons has, for example, also been studied in the context of the optical absorption [85] and transport [86] in carbon nanotubes, the current saturation in graphene [87], as well as the relaxation of optically excited carriers in graphene [88]. As mentioned above, phonon-assisted transitions induced by photons with energies $\hbar\omega < 2\mu$ become possible due to electron-phonon coupling (see Fig. 3.2). Our main goal in this chapter is to study the optical conductivity in the presence of phonons. Since it has been shown in Ref. 73 that—in contrast to the dc conductivity—the effect of acoustic phonons on the optical conductivity is negligible (see below), we restrict ourselves to optical as well as surface polar phonons (SPP). These SPPs are due to polar substrates onto which the graphene sheet is applied and for which we use SiO_2 as a specific material in our model. While the impact of optical phonons has been studied in several earlier works [72, 73, 74, 75, 78], the effect of SPPs on the optical conductivity in graphene is yet to be examined. Here, we use the linear response theory to derive a Kubo formula for the optical conductivity and

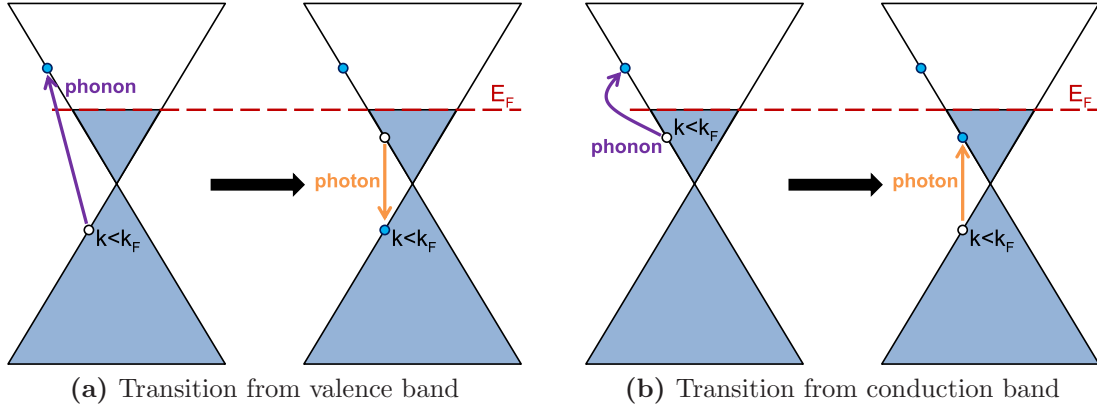


Figure 3.2.: Optical transitions in n -doped graphene if single-particle states and interaction between electrons and phonons are considered. A (a) valence- or (b) conduction-band electron absorbs or emits a phonon and the electronic system reaches a virtual state. By absorbing or radiating a photon, the electronic system then reaches its final state. Energy and momentum conservation has to be satisfied only when comparing the initial and final states. Note that reverse processes where a photon is first absorbed to arrive at a virtual state and the final state is reached by absorption or emission of a phonon are also possible.

evaluate this formula for several different combinations of phonons, including SPPs. Moreover, we include the effect of disorder on a phenomenological level. This chapter consists of two main parts, Sec. 3.2, which gives a brief overview of the model and the theoretical background of the formalism we employ here, and Sec. 3.3, which is devoted to the discussion of the effect of optical and surface polar phonons on the optical conductivity. A brief summary and outlook conclude the chapter.

3.2. Model

3.2.1. Hamiltonian and electron Green's function

Graphene consists of carbon atoms which are arranged in a 2D honeycomb lattice, that is, the hexagonal structure shown in Fig. 3.3 (a). This hexagonal structure is described by a 2D Bravais lattice with the vectors

$$\mathbf{a}_{1/2} = \frac{a}{2} \begin{pmatrix} 3 \\ \pm\sqrt{3} \end{pmatrix}, \quad (3.1)$$

where $a \approx 1.42 \text{ \AA}$ denotes the distance between two carbon atoms, and by a basis consisting of two carbon atoms, labeled A and B. Its reciprocal lattice is also a

3. Optical conductivity of graphene

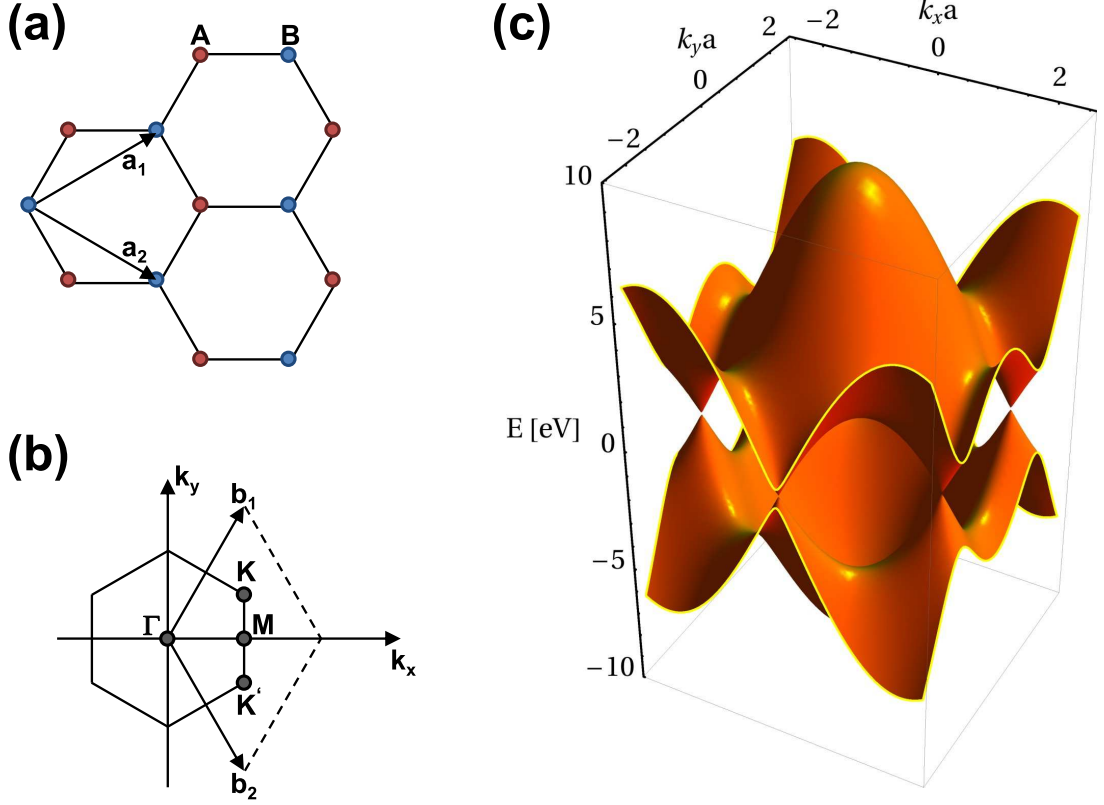


Figure 3.3.: (a) Real and (b) reciprocal lattices of graphene as well as the (c) energy spectrum obtained within the tight-binding description of graphene. Here, $a \approx 1.42 \text{ \AA}$ is the distance between two carbon atoms.

hexagonal lattice [see Fig. 3.3 (b)] which is spanned by the unit vectors

$$\mathbf{b}_{1/2} = \frac{2\pi}{3a} \begin{pmatrix} 1 \\ \pm\sqrt{3} \end{pmatrix}. \quad (3.2)$$

The electronic band structure of graphene can be described within a tight-binding approach [2, 60] and one finds that the valence and conduction bands touch each other at

$$\mathbf{K} = \frac{2\pi}{3a} \begin{pmatrix} 1 \\ 1/\sqrt{3} \end{pmatrix} \quad \text{and} \quad \mathbf{K}' = \frac{2\pi}{3a} \begin{pmatrix} 1 \\ -1/\sqrt{3} \end{pmatrix}. \quad (3.3)$$

In the following, we use the nearest-neighbor tight-binding Hamiltonian, which can be written as

$$\hat{H}_e = -t \sum_{\mathbf{k}, s} \left[\Phi^*(\mathbf{k}) \hat{a}_{\mathbf{k}s}^\dagger \hat{b}_{\mathbf{k}s} + \Phi(\mathbf{k}) \hat{b}_{\mathbf{k}s}^\dagger \hat{a}_{\mathbf{k}s} \right] \quad (3.4)$$

in momentum space [2, 60]. Here, t is the nearest-neighbor hopping energy and $\hat{a}_{\mathbf{k}s}^\dagger$ ($\hat{b}_{\mathbf{k}s}^\dagger$) and $\hat{a}_{\mathbf{k}s}$ ($\hat{b}_{\mathbf{k}s}$) denote the creation and annihilation operators of electrons at

sublattice A (B) with momentum \mathbf{k} and spin s . Equation (3.4) contains the complex function

$$\Phi(\mathbf{k}) = 1 + \exp(-i\mathbf{k} \cdot \mathbf{a}_1) + \exp(-i\mathbf{k} \cdot \mathbf{a}_2), \quad (3.5)$$

where \mathbf{a}_1 and \mathbf{a}_2 denote the unit vectors of the hexagonal lattice introduced above. As can be seen from Eq. (3.4), the spin and the momentum are good quantum numbers and diagonalization of the electronic Hamiltonian yields

$$\hat{H}_e = \sum_{\mathbf{k}, s, \lambda} \varepsilon_\lambda(\mathbf{k}) \hat{c}_{\lambda \mathbf{k} s}^\dagger \hat{c}_{\lambda \mathbf{k} s}, \quad (3.6)$$

with the energies $\varepsilon_{c/v}(\mathbf{k}) = \pm t |\Phi(\mathbf{k})|$ of the conduction (c , $\lambda = +1$) and valence (v , $\lambda = -1$) bands [shown in Fig. 3.3 (c)] and the corresponding creation and annihilation operators $\hat{c}_{\lambda \mathbf{k} s}^\dagger$ and $\hat{c}_{\lambda \mathbf{k} s}$. In particular, one finds $\varepsilon_{c/v}(\mathbf{K}) = \varepsilon_{c/v}(\mathbf{K}') = 0$ for the energies at the K and K' points.

Since the goal of this chapter is to study and compare the effects of several different phonons on the optical conductivity of graphene, we need to take into account the presence of those phonons. A general phononic Hamiltonian reads as

$$\hat{H}_{\text{ph}} = \sum_{\mathbf{q}, \Lambda} \hbar \omega_\Lambda(\mathbf{q}) \hat{p}_{\mathbf{q} \Lambda}^\dagger \hat{p}_{\mathbf{q} \Lambda}, \quad (3.7)$$

where different phonon branches are labeled as Λ , the phonon momentum as \mathbf{q} , and the corresponding frequencies and creation (annihilation) operators as $\omega_\Lambda(\mathbf{q})$ and $\hat{p}_{\mathbf{q} \Lambda}^\dagger$ ($\hat{p}_{\mathbf{q} \Lambda}$). Whereas Eqs. (3.4) and (3.7) describe isolated systems of electrons and phonons, respectively, the coupling between those systems is given by

$$\hat{H}_{e-\text{ph}} = \sum_{\mathbf{k}, s, \lambda, \lambda'} \sum_{\mathbf{q}, \Lambda} M_{\mathbf{k} \mathbf{q} \Lambda}^{\lambda \lambda'} \left(\hat{p}_{-\mathbf{q} \Lambda}^\dagger + \hat{p}_{\mathbf{q} \Lambda} \right) \hat{c}_{\lambda(\mathbf{k}+\mathbf{q})s}^\dagger \hat{c}_{\lambda' \mathbf{k} s}, \quad (3.8)$$

where $M_{\mathbf{k} \mathbf{q} \Lambda}^{\lambda \lambda'}$ is the electron-phonon coupling matrix element [56]. Hence, the total Hamiltonian of our model reads as

$$\hat{H} = \hat{H}_e + \hat{H}_{\text{ph}} + \hat{H}_{e-\text{ph}} \quad (3.9)$$

and we use standard diagrammatic perturbation theory to calculate the electronic Matsubara Green's function

$$\mathcal{G}_{\lambda \lambda', s}(\mathbf{k}, i\nu_n) = - \int_0^{\hbar \beta} d\tau \left\langle \mathcal{T} \left[\hat{c}_{\lambda \mathbf{k} s}(\tau) \hat{c}_{\lambda' \mathbf{k} s}^\dagger(0) \right] \right\rangle e^{i\nu_n \tau}, \quad (3.10)$$

where τ and $i\nu_n$ denote the imaginary time and (fermionic) frequency, $\langle \dots \rangle$ the thermal average, \mathcal{T} the imaginary time-ordering operator, and $\beta = 1/(k_B T)$ with T and k_B being the temperature and the Boltzmann constant, respectively [56, 57, 58]. By

3. Optical conductivity of graphene

solving the corresponding Dyson equation, we can express the electronic Green's function via the self-energy $\Sigma_{\lambda\lambda'}(\mathbf{k}, i\nu_n)$ and obtain the matrix elements

$$\begin{aligned}\mathcal{G}_{vv,s}(\mathbf{k}, i\nu_n) &= \frac{1}{\tilde{G}_v^{-1}(\mathbf{k}, i\nu_n) - \Sigma_{vc}(\mathbf{k}, i\nu_n) \Sigma_{cv}(\mathbf{k}, i\nu_n) \tilde{G}_c(\mathbf{k}, i\nu_n) / \hbar^2}, \\ \mathcal{G}_{cc,s}(\mathbf{k}, i\nu_n) &= \frac{1}{\tilde{G}_c^{-1}(\mathbf{k}, i\nu_n) - \Sigma_{vc}(\mathbf{k}, i\nu_n) \Sigma_{cv}(\mathbf{k}, i\nu_n) \tilde{G}_v(\mathbf{k}, i\nu_n) / \hbar^2}, \\ \mathcal{G}_{vc/cv,s}(\mathbf{k}, i\nu_n) &= \frac{\Sigma_{vc/cv} / \hbar}{\tilde{G}_c^{-1}(\mathbf{k}, i\nu_n) \tilde{G}_v^{-1}(\mathbf{k}, i\nu_n) - \Sigma_{vc}(\mathbf{k}, i\nu_n) \Sigma_{cv}(\mathbf{k}, i\nu_n) / \hbar^2},\end{aligned}\quad (3.11)$$

where

$$\tilde{G}_{c/v}^{-1}(\mathbf{k}, i\nu_n) = i\nu_n - \frac{\varepsilon_{c/v}(\mathbf{k}) - \mu + \Sigma_{cc/vv}(\mathbf{k}, i\nu_n)}{\hbar}. \quad (3.12)$$

Here, $\mu = \mu(T)$ denotes the chemical potential at the temperature T . Calculating the self-energy up to the first non-vanishing order, we obtain

$$\begin{aligned}\Sigma_{ss'}(\mathbf{k}, i\nu_n) \approx \frac{1}{\hbar} \sum_{\Lambda, \mathbf{q}, \tilde{s}} M_{(\mathbf{k}-\mathbf{q})\mathbf{q}\Lambda}^{\tilde{s}\tilde{s}'} M_{\mathbf{k}, -\mathbf{q}\Lambda}^{\tilde{s}\tilde{s}'} \left\{ \frac{n_{\mathbf{q}\Lambda} + 1 - f[\epsilon_{\tilde{s}}(\mathbf{k}-\mathbf{q})]}{i\nu_n - [\epsilon_{\tilde{s}}(\mathbf{k}-\mathbf{q}) - \mu] / \hbar - \omega_{\Lambda}(\mathbf{q})} \right. \\ \left. + \frac{n_{\mathbf{q}\Lambda} + f[\epsilon_{\tilde{s}}(\mathbf{k}-\mathbf{q})]}{i\nu_n - [\epsilon_{\tilde{s}}(\mathbf{k}-\mathbf{q}) - \mu] / \hbar + \omega_{\Lambda}(\mathbf{q})} \right\},\end{aligned}\quad (3.13)$$

with the Fermi-Dirac and Bose-Einstein distribution functions, $f_{\text{FD}}(\varepsilon) = n_{\text{FD}}(\varepsilon - \mu)$ and $n_{\mathbf{q}\Lambda} = n_{\text{BE}}[\hbar\omega_{\Lambda}(\mathbf{q})]$, where $n_{\text{FD/BE}}(\varepsilon) = 1/[\exp(\beta\varepsilon) \pm 1]$.

Equation (3.13) shows that the total phononic contribution to the self-energy is obtained by summation over the different phonon branches of the system. In the following, we will briefly discuss the different phonons investigated within this chapter. One can distinguish between two types of phonons which couple to the electrons in graphene: intrinsic graphene phonons and surface polar phonons (SPP), that is, phonons in polar substrates which interact with the electrons in graphene via the electric fields those phonons cause.

As shown in Ref. 73, the effect of (graphene) acoustic phonons on the ac conductivity is negligible.¹ Hence, we only consider the (graphene) optical phonons as well as SPPs in this chapter. There are two branches of optical phonons, longitudinal-optical (LO) and transverse-optical (TO) phonons. In the vicinity of the Γ point, the dispersion of both LO and TO phonons (denoted by Γ_{LO} and Γ_{TO}) can be approximated by the constant energy $\hbar\omega_{\Gamma} \approx 197$ meV. Moreover, we need to know the products of the electron-phonon coupling matrix elements entering Eq. (3.13),

¹In the lowest order, acoustic phonons scatter elastically with electrons and their contribution is similar to that of Coulomb impurity scattering, where the latter is, however, much stronger. By introducing a finite lifetime broadening later on, we therefore also include the effect of acoustic phonons on a phenomenological level.

$\tilde{M}_\Lambda = M_{(\mathbf{k}-\mathbf{q})\mathbf{q}\Lambda}^{\lambda\tilde{\lambda}} M_{\mathbf{k},-\mathbf{q}\Lambda}^{\tilde{\lambda}\lambda'}$. Since $n_{\mathbf{q}\Gamma_{\text{TO}}} = n_{\mathbf{q}\Gamma_{\text{LO}}}$, we can use

$$\tilde{M}_{\Gamma_{\text{LO}}} + \tilde{M}_{\Gamma_{\text{TO}}} = \frac{\hbar D_\Gamma^2}{2NM_c\omega_\Gamma} (1 + \lambda\lambda'), \quad (3.14)$$

with the carbon mass M_c , the number of unit cells N , and $D_\Gamma \approx 11.2$ eV/Å [89, 90, 91, 92, 93]. Near the K and K' points, on the other hand, only the TO phonon (denoted by K_{TO}) has a nonnegligible electron-phonon coupling [87] and contributes to the electron self-energy and its dispersion in this region can again be assumed as constant, $\hbar\omega_K \approx 157$ meV. The coupling of the K_{TO} phonons to the electrons in graphene is described by

$$\tilde{M}_{K_{\text{TO}}} = \frac{\hbar D_\Gamma^2}{2NM_c\omega_K} \left[1 + \lambda\lambda' - \tilde{\lambda} (\lambda e^{-i\vartheta} + \lambda' e^{i\vartheta}) \right], \quad (3.15)$$

where $\vartheta = \Theta_{\mathbf{k}} - \Theta_{\mathbf{k}-\mathbf{q}}$ and $e^{i\Theta_{\mathbf{k}}} = \Phi(\mathbf{k}) / |\Phi(\mathbf{k})|$ [85, 89, 90].

Moreover, SPPs originating from a polar substrate on which graphene is prepared are included in our model. Typically, there are two longitudinal surface optical (SO) phonons in polar substrates that interact with the electrons in graphene and whose dispersion can again be approximated by constant frequencies ω_{SO_1} and ω_{SO_2} [87]. The SPP coupling matrix elements read as [94, 95]

$$\tilde{M}_\Lambda = \frac{\pi^2 e^2 F_\Lambda^2}{NAq} e^{-2qz_0} \left[1 + \lambda\lambda' + \tilde{\lambda} (\lambda e^{-i\vartheta} + \lambda' e^{i\vartheta}) \right], \quad (3.16)$$

where $A = 3\sqrt{3}a^2/2$ is the area of the unit cell, $z_0 \approx 3.5$ Å is the van der Waals distance between the graphene sheet and the substrate, and the parameter F_Λ^2 describes the magnitude of the polarization field, which in turn depends on the substrate material [96]. In this work, we use SiO_2 as specific substrate for our model with the parameters $\hbar\omega_{\text{SO}_1} = 58.9$ meV, $F_1^2 = 0.237$ meV, $\hbar\omega_{\text{SO}_2} = 156.4$ meV, and $F_2^2 = 1.612$ meV. Other polar substrates, such as HfO_2 , SiC , or hexagonal BN, can be treated in exactly the same way by using the appropriate substrate-specific values for the parameters $\hbar\omega_\Lambda$ and F_Λ (see Table I in Ref. [87]).

The above matrix elements have been derived under the assumption that the electric fields caused by the SPPs and interacting with the electrons in graphene are not screened. If we take into account that those electric fields are screened, we need to replace \tilde{M}_Λ in Eq. (3.16) by $\tilde{M}_\Lambda / [\epsilon(\mathbf{q}, \omega)]^2$, where $\epsilon(\mathbf{q}, \omega)$ is the dielectric function [95]. In this chapter, we focus on the qualitative effect of screening on the optical conductivity in the presence of SPPs and restrict ourselves to a simple model: The dielectric function is approximated by the static, low temperature dielectric function obtained from the Dirac Hamiltonian of graphene and the random-phase approximation (RPA). Within the RPA, the dielectric function is given by

$$\epsilon(\mathbf{q}, \omega) = 1 - \frac{2\pi e^2}{\kappa q} \Pi_g(\mathbf{q}, \omega), \quad (3.17)$$

3. Optical conductivity of graphene

where κ is the background dielectric constant and $\Pi_g(\mathbf{q}, \omega)$ the polarization function of graphene [97, 98]. Here, we use the background dielectric constant $\kappa = 2.5$ [95, 98]. At low temperatures, the static polarization function is given by [97, 98]

$$\frac{\Pi_g(\mathbf{q}, 0)}{\nu_g} = 1 + \Theta\left(\frac{q}{2k_F^g} - 1\right) \frac{q}{4k_F^g} \left[\arccos\left(\frac{2k_F^g}{q}\right) - \frac{2k_F^g}{q} \sqrt{1 - \left(\frac{2k_F^g}{q}\right)^2} \right]. \quad (3.18)$$

Here, k_F^g denotes the Fermi wave vector and ν_g the density of states at the Fermi level in graphene.

In the following section, we will write down a Kubo formula for the optical conductivity in graphene and express the resulting correlation functions in terms of the phonon-dressed electron Green's function calculated above.

3.2.2. Kubo formula for the optical conductivity

Our starting point in the derivation of a Kubo formula for the optical conductivity is the current operator. As explained in Ref. 74, one way to obtain the current operator $\hat{\mathbf{I}}$ in the tight-binding description of graphene is to describe the effect of a uniform electric field

$$\mathbf{E}(t) = -\frac{\partial \mathbf{A}(t)}{\partial t} \quad (3.19)$$

by the uniform vector potential $\mathbf{A}(t)$ and by introducing the vector potential via the Peierls' phase [48] in the Hamiltonian \hat{H} . After that, this modified Hamiltonian is expanded in powers of the vector potential up to the first order. If the vector potential/electric field is oriented along the x -direction and contributions due to \hat{H}_{e-ph} are disregarded, this procedure yields

$$\hat{I}_x = \hat{I}_x^d A_x(t) + \hat{I}_x^p, \quad (3.20)$$

which consists of the paramagnetic current operator

$$\hat{I}_x^p = \frac{iev_F}{3} \sum_{\mathbf{k}, s} \left\{ [\Phi^*(\mathbf{k}) - 3] \hat{a}_{\mathbf{k}s}^\dagger \hat{b}_{\mathbf{k}s} - \text{h.c.} \right\} \quad (3.21)$$

and the diamagnetic current operator $\hat{I}_x^d A_x(t)$, where

$$\hat{I}_x^d = -\frac{e^2 v_F^2}{9t} \sum_{\mathbf{k}, s} \left\{ [\Phi^*(\mathbf{k}) + 3] \hat{a}_{\mathbf{k}s}^\dagger \hat{b}_{\mathbf{k}s} + \text{h.c.} \right\} \quad (3.22)$$

and $v_F = 3at/(2\hbar)$. Up to the first order, the effect of the electric field can be described by

$$\hat{H}_{\text{ext}} = -\hat{\mathbf{I}}^p \cdot \mathbf{A}(t) = -\hat{I}_x^p A_x(t), \quad (3.23)$$

with the total Hamiltonian of the system in the presence of a uniform external electric field being $\hat{H} + \hat{H}_{\text{ext}}$.

Using linear response theory (for the unperturbed Hamiltonian \hat{H} and the perturbation \hat{H}_{ext}) and conducting a Fourier transformation with respect to the time [56, 57, 58], we find that the current density due to the external field is given by

$$\delta \langle \hat{j}_x(\omega) \rangle = \frac{1}{S} \left[\langle \hat{I}_x^d \rangle - \frac{1}{\hbar} \Pi_{xx}^R(\omega) \right] A_x(\omega) \quad (3.24)$$

with $S = NA$ being the surface area of the graphene sample and $\Pi_{xx}^R(\omega)$ being the (Fourier transformed) retarded current-current correlation function. The retarded correlation function $\Pi_{xx}^R(\omega)$ can be related to the imaginary-time correlation function

$$\Pi_{xx}(i\omega_n) = - \int_0^{\hbar\beta} d\tau \left\langle \mathcal{T} \left[\hat{I}_x^p(\tau) \hat{I}_x^p(0) \right] \right\rangle e^{i\omega_n \tau} \quad (3.25)$$

by $\Pi_{xx}^R(\omega) = \Pi_{xx}(\omega + i0^+)$, that is, by replacing $i\omega_n$ with $\omega + i0^+$ in Eq. (3.25) [56, 57, 58]. Here, $i\omega_n$ denotes a bosonic frequency. Hence, the Kubo formula for the conductivity reads as

$$\sigma_{xx}(\omega) = \frac{-i \langle I_x^d \rangle}{S\omega} + \frac{i \Pi_{xx}^R(\omega)}{\hbar S \omega}. \quad (3.26)$$

We are interested in the real part of the conductivity, which can be extracted from Eq. (3.26) and reads

$$\text{Re}[\sigma_{xx}(\omega)] = - \frac{\text{Im}[\Pi_{xx}^R(\omega)]}{\hbar \omega S}, \quad (3.27)$$

where we have also used that the thermal average $\langle I_x^d \rangle$ is a real number.

If Eq. (3.21) is inserted into Eq. (3.25) and vertex corrections are ignored, we find

$$\begin{aligned} \Pi_{xx}(i\omega_n) &= \left(\frac{ev_F}{6} \right)^2 \sum_{\mathbf{k}, s} \sum_{\lambda_1 \dots \lambda_4} d(\mathbf{k}, \lambda_1, \lambda_2, \lambda_3, \lambda_4) \\ &\quad \frac{1}{\beta \hbar} \sum_{i\nu_{n'}} \mathcal{G}_{\lambda_1 \lambda_2}(\mathbf{k}, i\nu_{n'} + i\omega_n) \mathcal{G}_{\lambda_3 \lambda_4}(\mathbf{k}, i\nu_{n'}), \end{aligned} \quad (3.28)$$

where the phonon-dressed Green's functions are given by Eq. (3.11) and the dipole matrix element by

$$\begin{aligned} d(\mathbf{k}, \lambda_1, \lambda_2, \lambda_3, \lambda_4) &= |\Phi(\mathbf{k}) - 3|^2 (\lambda_1 \lambda_2 + \lambda_3 \lambda_4) \\ &\quad - e^{2i\Theta_{\mathbf{k}}} [\Phi^*(\mathbf{k}) - 3]^2 \lambda_1 \lambda_3 - e^{-2i\Theta_{\mathbf{k}}} [\Phi(\mathbf{k}) - 3]^2 \lambda_2 \lambda_4. \end{aligned} \quad (3.29)$$

By expressing the Green's functions in Eq. (3.28) via their spectral functions,

$$\mathcal{A}_{\lambda\lambda'}(\mathbf{k}, \omega) = -2\text{Im}[\mathcal{G}_{\lambda\lambda'}(\mathbf{k}, \omega + i0^+)], \quad (3.30)$$

3. Optical conductivity of graphene

and computing the resulting sum over the fermionic frequencies, we then obtain

$$\begin{aligned} \Pi_{xx}(\omega_n) = \left(\frac{ev_F}{6}\right)^2 \sum_{\mathbf{k}, s} \sum_{\lambda_1 \dots \lambda_4} \int \frac{d\omega' d\omega''}{(2\pi)^2} \frac{n_{\text{FD}}(\hbar\omega') - n_{\text{FD}}(\hbar\omega'')}{i\nu_n + \omega' - \omega''} d(\mathbf{k}, \lambda_1, \lambda_2, \lambda_3, \lambda_4) \\ \times \mathcal{A}_{\lambda_1 \lambda_2}(\mathbf{k}, \omega'') \mathcal{A}_{\lambda_3 \lambda_4}(\mathbf{k}, \omega') \end{aligned} \quad (3.31)$$

for the correlation function [56]. Equation (3.31) is an extension of the expression found for the current-current correlation function in Ref. 72, Eq. (34), to the case of a general, not necessarily diagonal self-energy.

If the self-energy is diagonal, the spectral function reads $\mathcal{A}_{\lambda\lambda'}(\mathbf{k}, \omega) = \delta_{\lambda\lambda'} \mathcal{A}_\lambda(\mathbf{k}, \omega)$ and one can simplify the expression for the imaginary part of the retarded correlation function,

$$\begin{aligned} \text{Im}[\Pi_{xx}^R(\omega)] = -\left(\frac{ev_F}{6}\right)^2 \sum_{\mathbf{k}} \sum_{\lambda, \lambda'} \int \frac{d\omega'}{2\pi} [n_{\text{FD}}(\hbar\omega') - n_{\text{FD}}(\hbar\omega + \hbar\omega')] \\ \times d(\mathbf{k}, \lambda, \lambda, \lambda', \lambda') \mathcal{A}_\lambda(\mathbf{k}, \omega + \omega') \mathcal{A}_{\lambda'}(\mathbf{k}, \omega'). \end{aligned} \quad (3.32)$$

In order to obtain Eq. (3.32), we have used that $d(\mathbf{k}, \lambda, \lambda, \lambda', \lambda')$ is real. By insertion of Eq. (3.32) into Eq. (3.27), we arrive at

$$\begin{aligned} \text{Re}[\sigma_{xx}(\omega)] = \left(\frac{ev_F}{6}\right)^2 \frac{1}{\hbar\omega S} \sum_{\mathbf{k}} \sum_{\lambda, \lambda'} \int \frac{d\omega'}{2\pi} [n_{\text{FD}}(\hbar\omega') - n_{\text{FD}}(\hbar\omega + \hbar\omega')] \\ \times d(\mathbf{k}, \lambda, \lambda, \lambda', \lambda') \mathcal{A}_\lambda(\mathbf{k}, \omega + \omega') \mathcal{A}_{\lambda'}(\mathbf{k}, \omega') \end{aligned} \quad (3.33)$$

if the self-energy is diagonal.

The main focus of this chapter is on the ac conductivity and consequently on the contribution arising due to the imaginary part of the correlation function, Π_{xx} , in Eq. (3.27). In order to calculate the optical conductivity numerically, we proceed as follows: First the self-energy due to electron-phonon coupling is computed via Eq. (3.13), from which the Green's and spectral functions can then be extracted by way of Eqs. (3.11) and (3.30). Inserting the spectral functions obtained by this procedure into Eq. (3.31) and taking the imaginary part of the resulting correlation function yields the conductivity.

3.3. Results

In the following, we investigate the dependence of the optical conductivity on the temperature and doping levels if the coupling between electrons and several different phonons is included. For simplicity, effects of renormalization of the chemical potential due to the real part of the self-energy are not considered, as are the effects

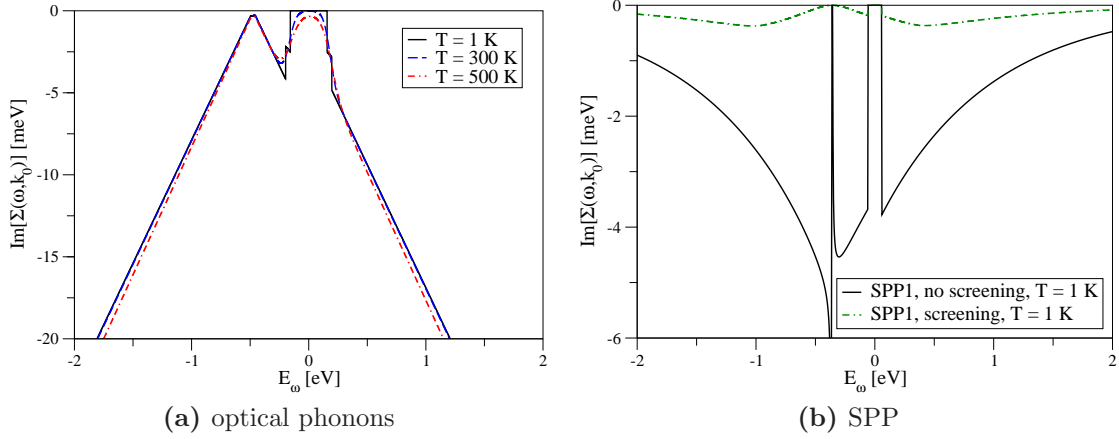


Figure 3.4.: Frequency dependence of the contributions (a) due to the K_{TO} , Γ_{LO} and Γ_{TO} optical phonons and (b) due to the the SPP at $\hbar\omega_{\text{SO}_1} = 58.9$ meV (for a SiO_2 substrate) to the imaginary part of the (retarded) self-energy $\Sigma_{\lambda\lambda}(\mathbf{k}, \omega)$ near the K point ($t|\Phi(\mathbf{k}_0)| \approx 5$ meV) for $\mu = 0.3$ eV, several different temperatures, and $\lambda = +$.

of the offdiagonal elements of the self-energy, which at least in the case of optical phonons is a very good approximation. This can also be discerned from the fact that, if one uses the effective Dirac Hamiltonian of graphene instead of the tight-binding Hamiltonian (3.4), the contribution from optical phonons to the offdiagonal self-energy (3.13) is identically zero.

As mentioned above, we consider the graphene sheet to be on a SiO_2 substrate, a widely used material for experiments with graphene. Moreover, a SiO_2 substrate is polar and has optical polar modes that produce electric fields affecting the electrons in graphene (see above). Numerical integrations over ω have been conducted on a grid with $\Delta(\hbar\omega) = 0.25$ meV and a cutoff $\hbar|\omega| < 4$ eV. Likewise, sums and integrals over \mathbf{k} have been computed on a lattice with a spacing of $\Delta(\hbar v_F k) = 0.25$ meV along the directions given by \mathbf{b}_1 and \mathbf{b}_2 and an energy cutoff $t|\Phi(\mathbf{k})| < 1$ eV.

Typical contributions to the imaginary part of the (retarded) self-energy $\Sigma_{\lambda\lambda}(\mathbf{k}, \omega)$ are shown in Fig. 3.4, where the contributions from the optical phonons and the SPP at $\hbar\omega_{\text{SO}_1} = 58.9$ meV of the substrate SiO_2 are displayed for $\lambda = +$. As can be seen in Fig. 3.4, for each optical phonon or SPP (denoted by Λ) the self-energy is very small in the region $-\hbar\omega_\Lambda < \hbar\omega < \hbar\omega_\Lambda$ at low temperatures. Indeed, the self-energy vanishes in this region at $T = 0$, a consequence of the Fermi-Dirac and Bose-Einstein distribution functions entering in Eq. (3.13). At higher temperatures, the self-energy in this region increases as can be seen in Fig. 3.4 (a) for optical phonons. The same behavior can be observed for the imaginary part of the (diagonal) self-energy due to SPPs. A major difference that can be seen between the optical phonons and the SPPs

3. Optical conductivity of graphene

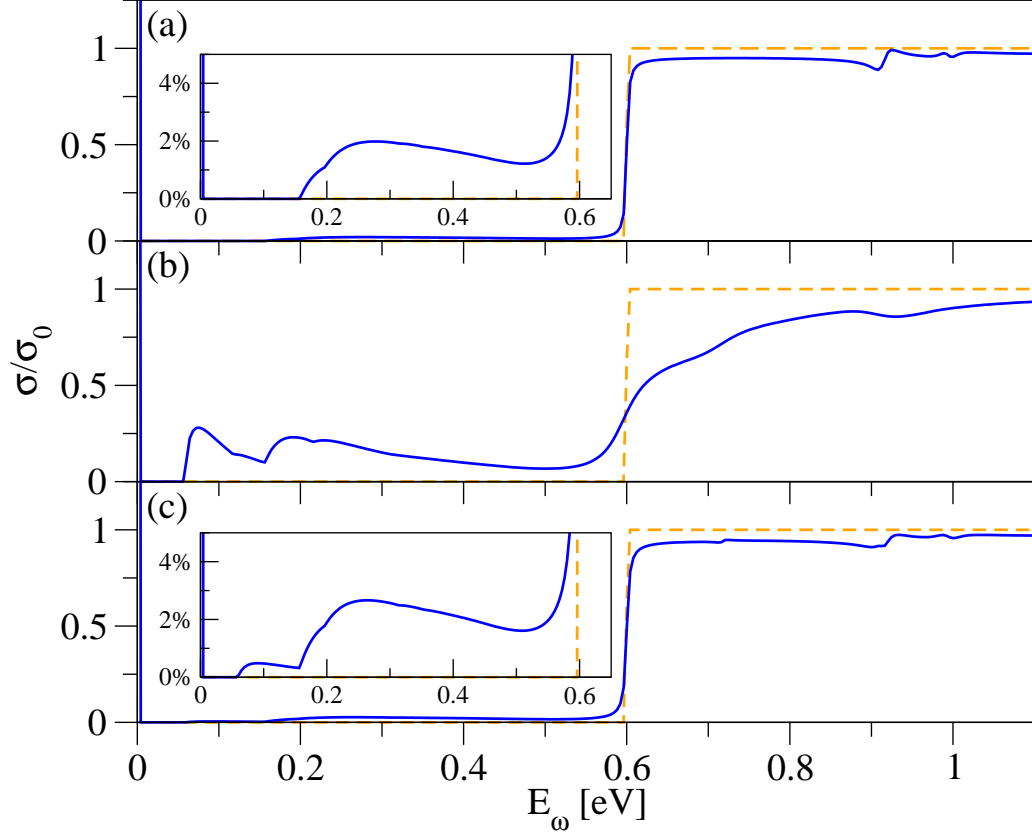


Figure 3.5.: Frequency dependence of the optical conductivity for $T = 1$ K, $\mu = 0.3$ eV, and several different phonon contributions (solid lines): (a) optical phonons, (b) optical phonons and SPPs, (c) optical phonons and screened SPPs. For comparison, the optical conductivity in the absence of disorder and phonons is included in each figure (dashed lines). The insets in Figs. (a) and (c) illustrate the details of the phonon sidebands.

is that the imaginary part increases with increasing absolute value of the frequency,² whereas the absolute value of the imaginary part of the self-energy contribution tends to zero with increasing $|\omega|$, a consequence of the exponential decay of the SPP matrix element 3.16. In the case of unscreened SPPs, there is furthermore a singularity at $\hbar\omega \approx -\hbar\omega_\Lambda - \mu + t|\Phi(\mathbf{k})|$ [if \mathbf{k} is not exactly at the K or K' points, where $\Phi(\mathbf{k}) = 0$ and the singularity does not arise]. By including screening, this singularity is canceled, which can be seen in Fig. 3.5 (b).

²Strictly speaking, this is only true if $|\omega|$ is not too large. In essence, the imaginary part of the self-energy due to optical phonons can be written as a combination of Fermi-Dirac and Bose-Einstein distribution functions and the graphene density-of-states evaluated at different energies. The density of states vanishes for energies $|\epsilon| > 3t$ in the tight-binding model, which also means that the imaginary part of the self-energy due to phonons vanishes for large frequencies.

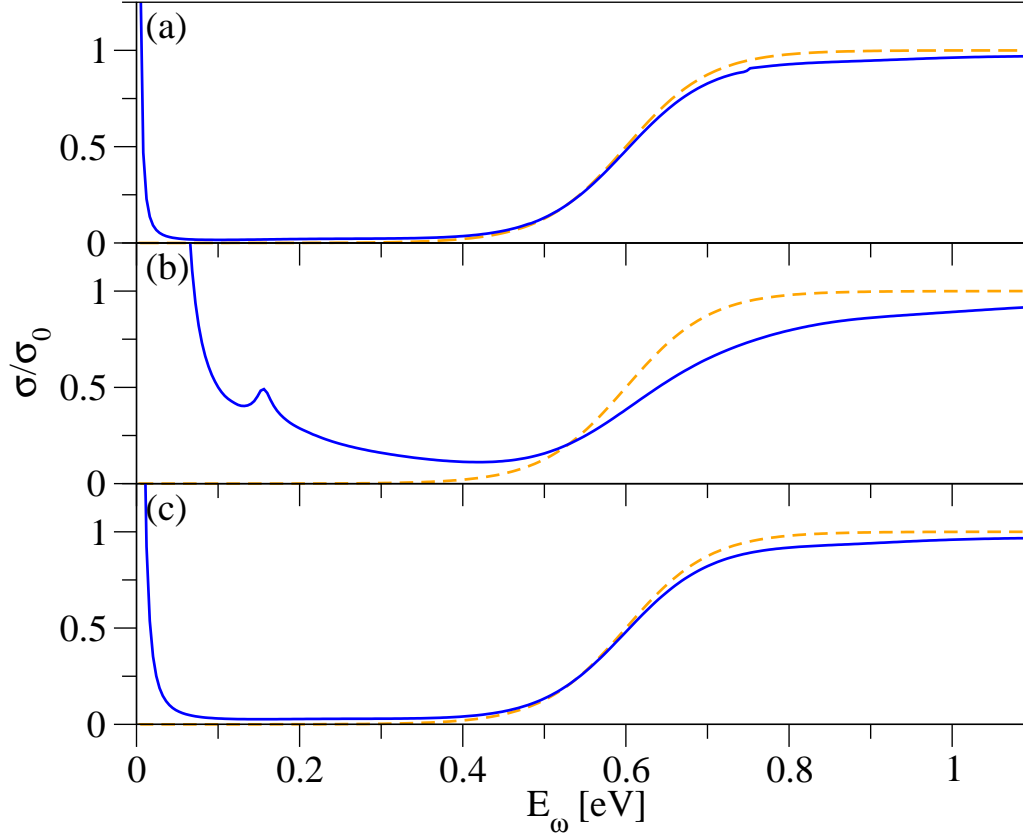


Figure 3.6.: Frequency dependence of the optical conductivity for $T = 300$ K, $\mu = 0.3$ eV, and several different phonon contributions (solid lines): (a) optical phonons, (b) optical phonons and SPPs, (c) optical phonons and screened SPPs. For comparison, the optical conductivity in the absence of disorder and phonons is included in each figure (dashed lines).

In Fig. 3.5, the optical conductivity for a fixed chemical potential $\mu = 0.3$ eV, the temperature $T = 1$ K, and several different combinations of phonons is shown: Figure 3.5 (a) depicts the combined effect of the K_{TO} , Γ_{LO} and Γ_{TO} optical phonons, whereas Figs. 3.5 (b) and (c) depict the combined effects if optical phonons as well as both SPPs due to the substrate SiO_2 are taken into account. The results for the case where no screening is included in the model are shown in Fig. 3.5 (b) and the results obtained by including the static screening as introduced in Sec. 3.2.1 are shown in Fig. 3.5 (c).

The profiles in Fig. 3.5 (a) illustrate the main features of the effect electron-phonon coupling has on the optical conductivity (if no other scattering mechanisms are considered): Whereas there is a gap with the width 2μ in the absorption spectrum of the purely electronic single-particle model, where direct transitions between the electronic states in the conduction and valence bands are forbidden for those energies

3. Optical conductivity of graphene

due to Pauli blocking, there is a finite absorption in the region $0 < \hbar\omega < 2\mu$ in the presence of phonons. For energies exceeding the lowest phonon energy— $\hbar\omega = 157$ meV for K_{TO} phonons—phonon-assisted transitions are possible, giving rise to the phonon sideband seen in the inset of Fig. 3.5 (a). Only for energies at least twice the chemical potential, direct transitions are possible, resulting in a steep rise of the optical conductivity to the universal saturation value $\sigma_0 = e^2/(4\hbar)$. Figure 3.5 (a) also shows that electron-phonon coupling smears out the sharp transition at 2μ . Due to the finite imaginary part of the self-energy originating from the electron-phonon coupling, there is also a very narrow ($\Delta\omega \lesssim 4$ meV) Drude peak at $\omega = 0$. Another noticeable feature seen in Fig. 3.5 (a) is that the optical conductivity in the saturation regime $\hbar\omega > 2\mu$ is no longer perfectly smooth due to the electron-phonon coupling, an effect which has also been observed in Ref. 73.

If SPPs are included in addition to the optical phonons [see Fig. 3.5 (b)], absorption is possible already at $\hbar\omega_{SO_1} = 58.9$ meV and the maximal value for the absorption in the gap rises from $\sigma_{\max} \approx 0.02\sigma_0$ to $\sigma_{\max} \gtrsim 0.25\sigma_0$. Furthermore, the optical conductivity does not increase at $\approx 2\mu$ as steeply as in the clean case or the case where only optical phonons are included. A more realistic approach is to take into account screening for the SPPs, the result of which is shown in Fig. 3.5 (c). Here, the maximal value for the absorption in the gap is slightly larger compared to the maximal value one obtains if only optical phonons are included and one can clearly see the additional phonon sideband originating from the SPP at $\hbar\omega_{SO_1} = 58.9$ meV. If the temperature is increased to $T = 300$ K (see Fig. 3.6), one can see that the peak at $\omega = 0$ is broadened as more phonons become available and electron-phonon scattering becomes more probable. Furthermore, the profiles of the optical conductivity are much smoother compared to $T = 1$ K and only in the presence of unscreened SPPs can one still observe a peak from the SPP at $\hbar\omega_{SO_2} = 156.4$ meV [see Fig. 3.6 (b)]. Comparing Figs. 3.6 (a) and (c), one can also see how the optical conductivity at low energies, $\hbar\omega \approx 0.1$ eV, is increased in the presence of screened SPP compared to the case when only optical phonons are included.

Until now, our discussion has been restricted to the case of a clean system, where only phonons have been included. In the following, we take into account disorder by introducing a constant, phenomenological broadening parameter Γ_{br} in the imaginary part of the self-energy. Figure 3.7 shows the profiles of the optical conductivity at $T = 300$ K for $\Gamma_{br} = 5$ meV and the same combination of phonons as in Figs. 3.5 and 3.6. If no phonons are included (dashed lines), one can observe a broad Drude peak at $\omega = 0$ as well as finite absorption for the entire region $0 < \hbar\omega < 2\mu$. As can be seen in Figs. 3.7 (a) and (c), the effect of optical phonons and screened SPPs is to increase the absorption for $\hbar\omega \lesssim 2\mu$, although the main contribution arises due to the finite lifetime broadening, and to decrease the optical conductivity in the saturation regime. The same behavior can be found if unscreened SPPs are included, but as in the case of a clean system, the effects are much more pronounced here.

Figure 3.8 shows the optical conductivity at low temperatures for several different

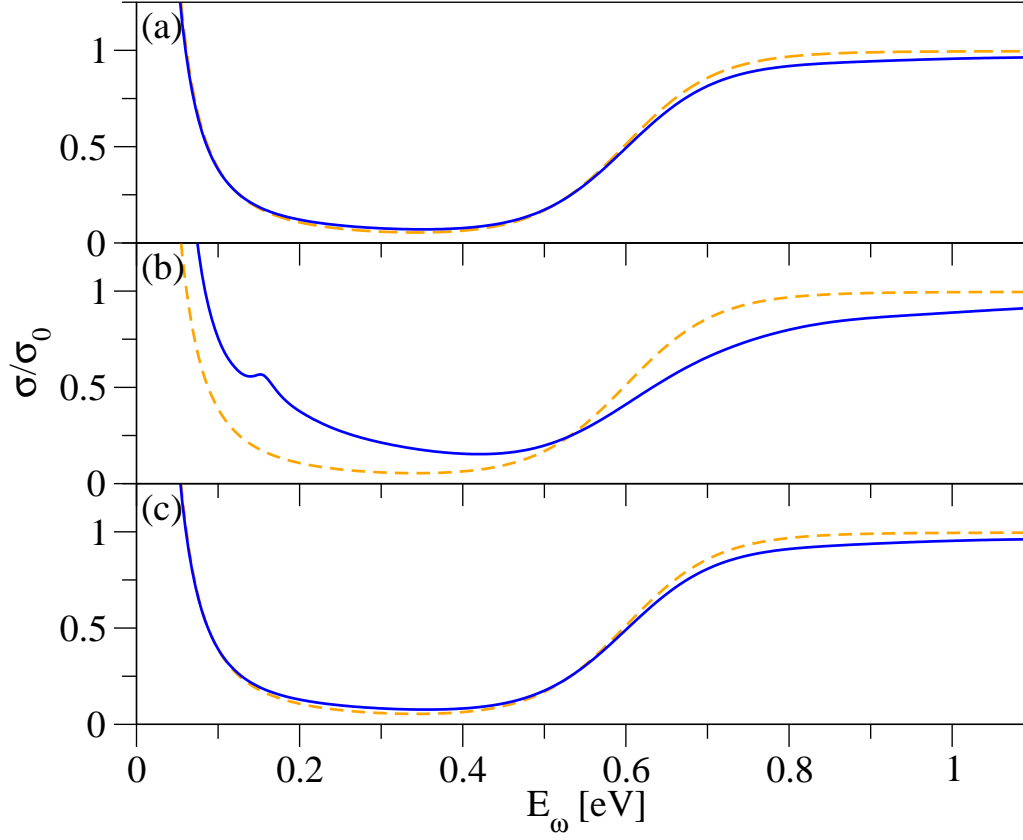


Figure 3.7.: Frequency dependence of the (real part of the) optical conductivity of graphene for $T = 300$ K, $\mu = 0.3$ eV, $\Gamma_{\text{br}} = 5$ meV, and several different phonon contributions (solid lines): (a) optical phonons, (b) optical phonons and SPPs, (c) optical phonons and screened SPPs. For comparison, the optical conductivity in the absence phonons, but with $\Gamma_{\text{br}} = 5$ meV is included in each figure (dashed lines).

combinations of phonons and different chemical potentials. Apart from the trends in the behavior of the optical conductivity discussed above, one can clearly see different gaps in the absorption spectrum, given by 2μ for each chemical potential. Another feature that can be discerned from Fig. 3.8 is that the maximal value of the phonon sideband increases with increasing chemical potential. This behavior can be observed for $\Gamma_{\text{br}} = 0$ as well as for $\Gamma_{\text{br}} = 5$ meV.

The values of the optical conductivity at $\hbar\omega = \mu$ and $\hbar\omega \rightarrow 0$ as functions of the temperature and for fixed chemical potentials and $\Gamma_{\text{br}} = 5$ meV are shown in Fig. 3.9 for the same combinations of phonons as above. At low temperatures, the midgap absorption does not depend strongly on the temperature. If the temperature is further increased, on the other hand, an increase of the optical conductivity at $\hbar\omega = \mu$ can be observed [see Fig. 3.9 (a)]. The smaller the chemical potential,

3. Optical conductivity of graphene

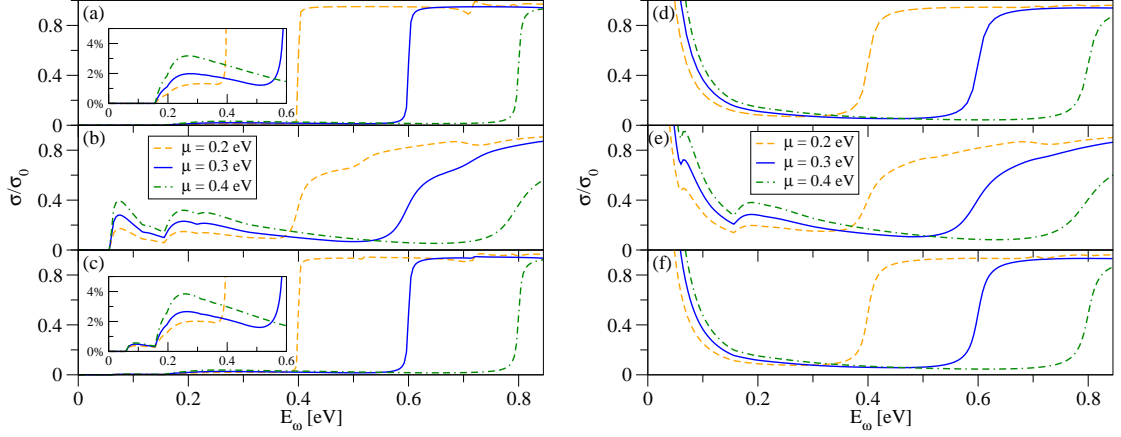


Figure 3.8.: Frequency dependence of the (real part of the) optical conductivity of graphene for $T = 1$ K, (a)-(c) $\Gamma_{\text{br}} = 0$ and (d)-(f) $\Gamma_{\text{br}} = 5$ meV, several chemical potentials, and several different phonon contributions: (a)/(d) optical phonons, (b)/(e) optical phonons and SPPs, (c)/(f) optical phonons and screened SPPs.

the earlier a noticeable increase of the optical conductivity sets in. As before, the effect is most profound for unscreened SPPs. The conductivity at $\hbar\omega \rightarrow 0$, shown in Fig. 3.9 (b), decreases with increasing temperature as more phonons become available for scattering with electrons, thereby reducing the transport time and thus $\sigma(0)$.

3.4. Conclusions and outlook

In this chapter, we have investigated the effect that optical phonons as well as SPPs have on the optical conductivity in graphene. To do so, we have written down a Kubo formula to describe the optical conductivity in the tight-binding description of graphene. Our focus has been on the absorption at frequencies $\hbar\omega < 2\mu$, where transitions are forbidden due to Pauli blocking in a clean system, but which can occur if phonons are present, giving rise to one or more phonon sidebands. We have studied the temperature dependence of this absorption if just optical phonons are considered and if a combination of optical and SPPs is included in the model. Furthermore, we have used the static, zero-temperature dielectric function calculated within the RPA to qualitatively describe the effect of screening on the electronic coupling of SPPs. In the presence of (unscreened) SPPs, we observe a significant absorption for frequencies $\hbar\omega < 2\mu$, which suggests that considering unscreened SPPs is not an adequate description of the optical conductivity observed experimentally. For optical phonons and screened SPPs, we observe finite absorption in the region $0 < \hbar\omega < 2\mu$, but not as large as in the case where screened SPPs are included. If we also take into account a finite lifetime broadening for the electrons by means of introducing a phenomenological scattering rate, we find that—apart from the case where SPPs are

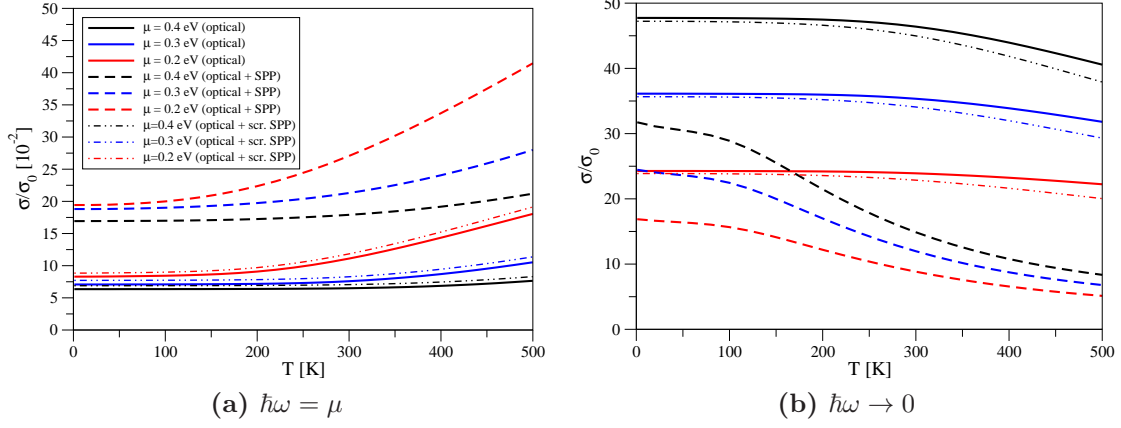


Figure 3.9.: Temperature dependence of the optical conductivity at (a) $\hbar\omega = \mu$ and (b) $\hbar\omega \rightarrow 0$ for several different chemical potentials μ and several combinations of phonons if $\Gamma_{\text{br}} = 5$ meV. The legend in Fig. (a) also refers to Fig. (b).

used without screening—the main absorption arises due to the lifetime broadening with an additional contribution to absorption arising from the phonons.

In the future, we plan to refine the present model by including a more realistic (energy-dependent) model to account for impurity scattering instead of the phenomenological constant. Moreover, in the case where screening is accounted for in the coupling between electrons and SPPs, the static dielectric function used so far should be replaced by the full temperature-dependent dielectric function.

4. Theory of thermal spin-charge coupling in electronic systems

4.1. Introduction

The central theme in spintronics is the generation and control of nonequilibrium electron spin in solids [8, 9, 99, 100]. So far, the spin generation has been done by optical, magnetic, and, most important for device prospects, electrical means [9, 101]. In a typical device, spin-polarized electrons from a ferromagnetic conductor are driven by electromagnetic force to a nonmagnetic conductor. There the spin accumulates, with the steady state facilitated by spin relaxation. There are also novel ways to generate pure spin currents, without accompanying charge currents [102, 103, 104, 105, 106]. The concept of electrical spin injection was first proposed by Aronov [107], and experimentally confirmed by Johnson and Silsbee [108], who also formulated the problem from a nonequilibrium thermodynamics and drift-diffusion view [109, 110]. An equivalent description in terms of quasichemical potentials, convenient to treat discrete (junction) systems, was formulated systematically by Rashba [111]. This model, which we call the standard model of spin injection, is widely used to describe electrical spin injection into metals and semiconductors [8, 9, 101] and can also be extended to ac currents [112].

Until recently, one particularly interesting possibility of generating spin, by spin-heat coupling, has been largely neglected. The generation of nonequilibrium spin by heat currents and the opposite process of generating heat currents by spin accumulation has already been proposed by Johnson and Silsbee [109] based on nonequilibrium thermodynamics concepts (see also Ref. 113). The spin-heat coupling is now the central point of spin caloritronics (or spin calorics) [114, 115, 7]. Although the theory of thermoelectricity has long been known [116, 117], only experimental improvements over the past few years have made its application in the context of generating and transporting spin appear possible [118, 119, 120, 121, 122].

At the heart of spin caloritronics is the spin Seebeck effect [123, 124, 125]. The conventional Seebeck effect, also called thermopower [117], describes the generation of an electric voltage when a thermal gradient is applied to a conductor. In analogy, the spin Seebeck effect describes the generation of spin accumulation in ferromagnets by thermal gradients. The effect was originally observed in the ferromagnetic conductor NiFe [123, 126], where indication of spin accumulation over large length scales (mil-

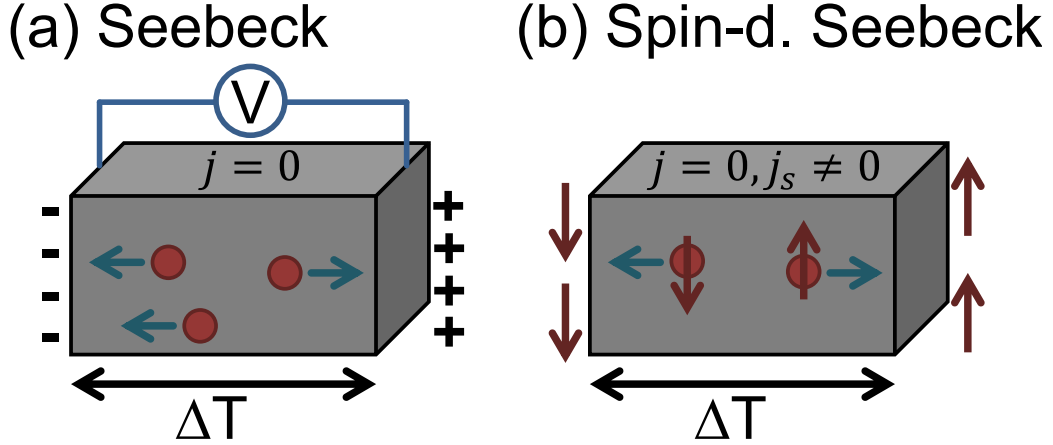


Figure 4.1.: Schematic illustrations of the (a) Seebeck and (b) spin-dependent Seebeck effects. Here, ΔT is the temperature difference, V the voltage, j the charge current, j_s the spin current, and vertical arrows denote up and down spin projections.

limeters), independent of the spin-relaxation scales in the ferromagnet, was found. Since it also exists at room temperature, the spin Seebeck phenomenon may have some technological applications [127].

Inspired by the conventional (charge) Seebeck effect, the spin Seebeck effect was originally thought to be driven by free electrons. Therefore, the first interpretation of the effect was made by generalizing thermoelectric concepts to account for the spin degree of freedom, as described in Refs. 123 and 126 and illustrated in Fig. 4.1. However, the spin Seebeck effect is not limited to metals. It has also been observed in ferromagnetic insulators [125] as well as in the ferromagnetic semiconductor (Ga,Mn)As [128]. This suggests that the spin Seebeck effect does not need to be connected with charge flow. In (Ga,Mn)As the sample was even cut preventing charge redistribution over the whole slab; the spin Seebeck signals were unaffected and in both cases, of compact and disconnected samples, the Pt stripes pick up the same inverse spin Hall signals [129, 130]. The evidence points to a mechanism of magnon-assisted spin pumping from the ferromagnet into the Pt, producing spin currents there. A theory for this spin pumping from a ferromagnetic insulator was suggested in Ref. 131. It was predicted that phonons can play an important role in the spin Seebeck effect, leading to its huge enhancement [132]. Recent measurements of the spin Seebeck effect in multiple (Ga,Mn)As samples also suggest that such an effect can be driven by phonons [133]. In order to explain the main trends of the observed temperature and spatial dependence of the spin Seebeck effect in (Ga,Mn)As, a phenomenological model involving phonon-magnon coupling was introduced [133].

As already demonstrated by this brief discussion of the correct interpretation of the spin Seebeck effect, the field of spin caloritronics is now no longer restricted to adopt-

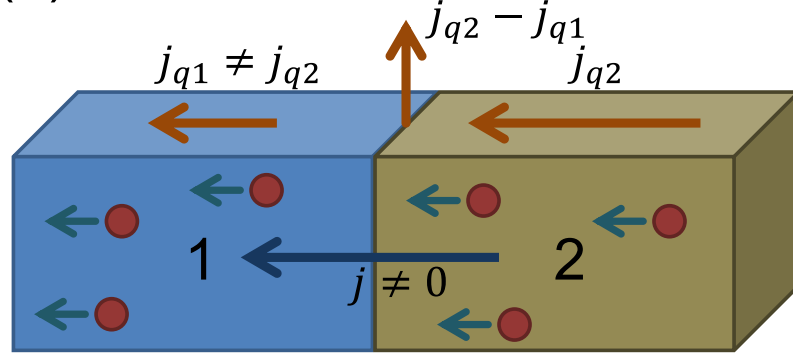
ing thermoelectrical concepts and incorporating the spin degree of freedom into them, but has become much wider. Following Ref. 7, one can classify spin caloritronic effects into three categories: (i) independent electron effects, that is, effects that can be described by combining thermoelectricity and collinear magnetoelectronics, (ii) collective effects, that is, effects that originate from the collective dynamics of the magnetic order parameter, and (iii) relativistic effects, that is, effects which arise from thermoelectric generalizations of relativistic corrections, such as the anomalous Hall and spin Hall effects. Whereas the original interpretation of the spin Seebeck effect would fall in category (i), the most likely interpretation of this effect mentioned above would fall in category (ii). Considering the quite confusing, but historically grown nomenclature for certain spin caloritronic effects, a nomenclature to systematically distinguish between these different categories has been introduced in Ref. 7. According to this nomenclature, single-electron effects as in category (i) should properly be labeled as spin-dependent thermoelectric effects. For example, the phenomenon of a spin current (carried by free electrons and) driven by a temperature gradient (see Fig. 4.1), that is, the original interpretation of the spin Seebeck effect and the obvious spin caloritronics analog to the Seebeck effect, is properly referred to as spin-dependent Seebeck effect in this nomenclature. In this chapter, we try to follow these conventions.

In addition to the Seebeck effect, there is also another thermoelectric effect, the Peltier effect, which refers to the evolution of heat across an isothermal junction of two different materials due to an electric current being passed through the junction [116, 117]. Recently, a spin caloritronics analog to the Peltier effect, termed spin-dependent Peltier effect, has been predicted and experimentally observed in a permalloy ($\text{Ni}_{80}\text{Fe}_{20}$)(PY)/copper/PY valve stack [134, 135]. The spin-dependent Peltier effect describes the heating or cooling at the interface between a ferromagnetic and normal conductor driven by a spin current (see Fig. 4.2).

Another fascinating discovery is that of the thermally driven spin injection from a ferromagnet to a normal conductor [136]. In this experiment, thermal currents in permalloy drive spin accumulation into copper, which is then detected in a non-local geometry [9, 101]. The structures were of submicron sizes, so it is plausible that the effects are electronic in nature and are a manifestation of the spin-dependent Seebeck effect, although magnon contributions to such thermal spin-injection setups could also be sizable. A practical model was introduced in Refs. 137, 134 to find, with a finite elements numerical scheme, the profiles of temperature and spin accumulation in the experimental devices. Recently, yet another form of thermal spin flow, coined Seebeck spin tunneling, has been demonstrated in ferromagnet-oxide-silicon tunnel junctions [138]. Here, a temperature difference between the ferromagnet and silicon causes a transfer of spin angular momentum across the interface between both materials.

An important goal for both theory and experiment of the spin(-dependent) Seebeck phenomena is to decipher the roles of the electronic and non-electronic contributions.

(a) Peltier



(b) Spin-dependent Peltier

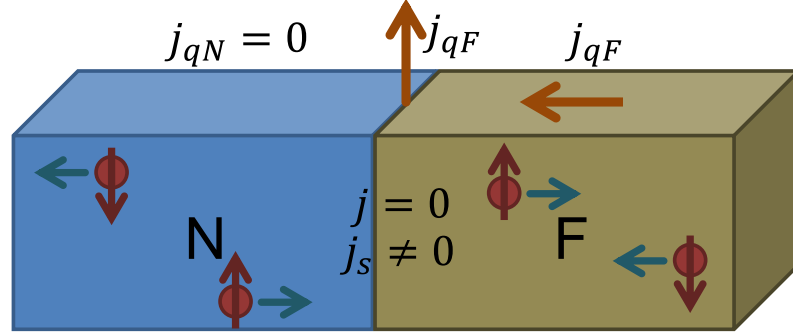


Figure 4.2.: Schematic illustrations of the (a) Peltier and (b) spin-dependent Peltier effects, where j and j_s denote the charge and spin currents. The thermal current j_q is different in each region. Small vertical arrows denote up/down spin projections.

It is yet unclear under which circumstances the electronic contribution may dominate. It seems likely that when going to smaller, submicron structures in which the spin accumulation will be a bulk effect, the spin phenomena carried by electrons will become important. Similarly, in materials with strong magnon damping, such that magnons are in local equilibrium with the given temperature profile, electrons may ultimately carry the entire spin(-dependent) Seebeck effect. It is thus important to set the benchmarks for the electronic contributions in useful device geometries. This is what we do in this chapter: we explore the role of the electronic contributions in F/N and F/N/F junctions, which are subjected to thermal gradients, and derive useful analytical formulas for various spin-injection efficiencies.

Our purpose is twofold: First, we use the drift-diffusion framework of the standard model of spin injection presented in Refs. 8, 9, 101 and generalize it to include electronic heat transport and thereby derive a theory for charge, spin, and heat transport

4.2. Spin-polarized transport in the presence of thermal fluctuations

in electronic materials.¹ Second, we apply this theory to describe F/N and F/N/F junctions placed in thermal gradients. While the Peltier and Seebeck effects in such structures have been investigated in Ref. 139, we focus here on the description of thermal spin injection and the investigation of the corresponding spin accumulation. We also look at the spin injection in the presence of both electric and thermal currents, and find the conditions under which the resulting spin current in N vanishes. In all junctions studied, we present, as general as possible, analytical formulas for the spin-accumulation and spin-current profiles, as well as for the thermal spin-injection efficiency and the nonequilibrium (spin-accumulation-driven) spin Seebeck coefficient. Moreover, we look at several different setups of the Peltier and spin-dependent Peltier effects and calculate their respective contributions to the heating or cooling at the interfaces in F/N and F/N/F junctions.

This chapter is organized as follows: Following the introduction of the formalism and the basic equations in Sec. 4.2, the electronic contribution to the spin Seebeck effect in a ferromagnetic metal is discussed within the framework of this formalism in Sec. 4.3, while Secs. 4.4 and 4.5 are devoted to the discussion of thermal spin injection and related thermoelectric effects in F/N and F/N/F junctions, respectively. A short summary concludes the chapter.

4.2. Spin-polarized transport in the presence of thermal fluctuations

4.2.1. Spin-unpolarized transport equations

As a first step, we will restrict ourselves to the description of transport in an electronic system that consists only of electrons of one species, that is, either of spin up or spin down electrons (denoted by the subscript $\lambda = \uparrow$ or $\lambda = \downarrow$ throughout this chapter). The derivation presented here is a textbook matter [117, 140] and is given here to introduce the terminology needed for the spin-polarized case and to match the concepts from the standard spin-injection model of Ref. 9.

If this system is in thermodynamic equilibrium, the temperature T and the chemical potential $\eta(T)$ are uniform throughout the system. Knowing the chemical potential,² one can calculate the density of the respective electron species under consideration from

$$n_{\lambda}^0[\eta(T), T] = \int d\varepsilon g_{\lambda}(\varepsilon) f_0 \left[\frac{\varepsilon - \eta(T)}{k_B T} \right], \quad (4.1)$$

¹This means that our model and the effects investigated in this chapter fall into category (i) of the aforementioned division of spin caloritronic effects.

²The chemical potential is not only a function of the temperature but also of the total electron density.

4. Theory of thermal spin-charge coupling in electronic systems

where k_B denotes the Boltzmann constant, $g_\lambda(\varepsilon)$ the electronic density of states at the energy ε , and f_0 the equilibrium Fermi-Dirac distribution function. Similarly, the equilibrium energy density is given by

$$e_\lambda^0[\eta(T), T] = \int d\varepsilon \varepsilon g_\lambda(\varepsilon) f_0 \left[\frac{\varepsilon - \eta(T)}{k_B T} \right]. \quad (4.2)$$

The system is not in equilibrium if an electric field $-\nabla\varphi(x)$ is present in its bulk. In this case the chemical potential becomes space dependent. This is taken into account by replacing $\eta(T)$ with $\eta(T) + e\mu_\lambda(x)$, where the quasichemical potential $\mu_\lambda(x)$ now contains the space dependence.³ Since we want to incorporate the effects of thermal gradients into our formalism, we furthermore allow for different local equilibrium temperatures by replacing the constant temperature T by a space-dependent temperature $T(x)$. As a consequence, there is an additional position dependence of the chemical potential due to the temperature, that is, $\eta(T)$ has to be replaced by $\eta[T(x)]$. Thus, the total chemical potential is given by $\eta[T(x)] + e\mu_\lambda(x)$. Assuming the local nonequilibrium distribution function to be only energy dependent because momentum relaxation happens on length scales much smaller compared to the variation of the electric potential $\varphi(x)$, one obtains

$$f_\lambda(\varepsilon, x) = f_0 \left\{ \frac{\varepsilon - \eta[T(x)] - e\mu_\lambda(x) - e\varphi(x)}{k_B T(x)} \right\}. \quad (4.3)$$

Therefore, the nonequilibrium electron and energy densities read as

$$n_\lambda(x) = \int d\varepsilon g_\lambda(\varepsilon) f_\lambda(\varepsilon, x) = n_\lambda^0 \{ \eta[T(x)] + e\mu_\lambda(x) + e\varphi(x), T(x) \}, \quad (4.4)$$

$$e_\lambda(x) = \int d\varepsilon \varepsilon g_\lambda(\varepsilon) f_\lambda(\varepsilon, x) = e_\lambda^0 \{ \eta[T(x)] + e\mu_\lambda(x) + e\varphi(x), T(x) \}. \quad (4.5)$$

The electrostatic field gives rise to an electric current. This charge current consists of two parts: the drift current, proportional to the electric field $E(x) = -\nabla\varphi(x)$ and the diffusion current, proportional to the gradient of the local electron density. Since the proportionality factor of the diffusion current, the diffusivity $D_\lambda(\varepsilon)$, is energy dependent, it is convenient to treat electrons with different energies separately. The spectral diffusion current density reads as

$$j_{D\lambda}(x, \varepsilon) d\varepsilon = e D_\lambda(\varepsilon) \nabla [g_\lambda(\varepsilon) f_\lambda(\varepsilon, x)] d\varepsilon, \quad (4.6)$$

³In general, μ_λ also depends on the temperature T . If we consider different, space-dependent local equilibrium temperatures $T(x)$, the gradient of the quasichemical potential reads as $\nabla\mu_\lambda[x, T(x)] = \frac{\partial\mu_\lambda}{\partial x} + \frac{\partial\mu_\lambda}{\partial T} \nabla T$. Since we are only interested in first order effects, the temperature dependence of μ_λ , which leads to a second order contribution (in the nonequilibrium quantities $\mu_\lambda[x, T(x)]$, $\varphi(x)$, and $\nabla T(x)$), can be omitted.

4.2. Spin-polarized transport in the presence of thermal fluctuations

from which the complete diffusion current can be obtained by integrating over the entire energy spectrum. The total charge current for electrons of spin λ is given by

$$j_\lambda(x) = -\sigma_\lambda \nabla \varphi(x) + e \int d\varepsilon D_\lambda(\varepsilon) g_\lambda(\varepsilon) \nabla f_\lambda(\varepsilon, x), \quad (4.7)$$

where σ_λ is the conductivity. By inserting Eq. (4.3) into Eq. (4.7), using the Einstein relation,⁴ and keeping only terms linear in the nonequilibrium quantities $\mu_\lambda(x)$ and $\varphi(x)$, we find

$$j_\lambda(x) = \sigma_\lambda \nabla \left\{ \frac{\eta[T(x)]}{e} + \mu_\lambda(x) \right\} - S_\lambda \sigma_\lambda \nabla T(x). \quad (4.8)$$

Here, the conductivity is given by the Einstein relation

$$\sigma_\lambda = e^2 \int d\varepsilon D_\lambda(\varepsilon) g_\lambda(\varepsilon) \left(-\frac{\partial f_0}{\partial \varepsilon} \right) \approx e^2 D_\lambda(\varepsilon_F) g_\lambda(\varepsilon_F) \quad (4.9)$$

and the Seebeck coefficient by

$$S_\lambda = -\frac{e}{\sigma_\lambda} \int d\varepsilon D_\lambda(\varepsilon) g_\lambda(\varepsilon) \left(-\frac{\partial f_0}{\partial \varepsilon} \right) \frac{\varepsilon - \eta[T(x)]}{T(x)} \approx -\mathcal{L} e T(x) \left[\frac{g'_\lambda(\varepsilon_F)}{g_\lambda(\varepsilon_F)} + \frac{D'_\lambda(\varepsilon_F)}{D_\lambda(\varepsilon_F)} \right]. \quad (4.10)$$

In both cases, the integrals are calculated to the first non-vanishing order in the Sommerfeld expansion [117]. The Lorenz number is $\mathcal{L} = (\pi^2/3)(k_B/e)^2$ and $g'_\lambda(\varepsilon_F)$ and $D'_\lambda(\varepsilon_F)$ are the derivatives of the density of states and the diffusivity with respect to the energy evaluated at the Fermi level ε_F .

In addition to the charge current, there is a heat current in nonequilibrium. A treatment similar to that of the charge current above yields

$$j_{q,\lambda}(x) = S_\lambda \sigma_\lambda T(x) \nabla \left\{ \frac{\eta[T(x)]}{e} + \mu_\lambda(x) \right\} - \mathcal{L} \sigma_\lambda T(x) \nabla T(x). \quad (4.11)$$

If the charge and heat currents are defined as in Eqs. (4.8) and (4.11), currents $j_\lambda(x) > 0$ and $j_{q,\lambda}(x) > 0$ flow parallel to the x direction.

At sharp contacts, the chemical potential and the temperature are generally not continuous. Thus, instead of Eqs. (4.8) and (4.11), discretized versions of these equations are used. The charge current at the contact (C) is given by

$$j_{\lambda c} = \Sigma_{\lambda c} \left(\frac{1}{e} \Delta \eta_c + \Delta \mu_{\lambda c} \right) - S_{\lambda c} \Sigma_{\lambda c} \Delta T_c \quad (4.12)$$

and the heat current by

$$j_{q\lambda c} = T S_{\lambda c} \Sigma_{\lambda c} \left(\frac{1}{e} \Delta \eta_c + \Delta \mu_{\lambda c} \right) - \mathcal{L} T \Sigma_{\lambda c} \Delta T_c, \quad (4.13)$$

⁴The Einstein relation is obtained by requiring that $j_\lambda = 0$ if $\nabla \left\{ \frac{\eta[T(x)]}{e} + \mu_\lambda(x) \right\} = 0$ and $\nabla T(x) = 0$.

4. Theory of thermal spin-charge coupling in electronic systems

where $\Delta\eta_c + e\Delta\mu_{\lambda c}$ and ΔT_c denote the drops of the total chemical potential and the temperature at the contact, respectively. The (effective) contact conductance and the contact thermopower are given by $\Sigma_{\lambda c}$ and $S_{\lambda c}$, respectively, while T is the average temperature of the system.

4.2.2. Spin-polarized transport equations

We now consider spin-polarized systems, which we treat as consisting of two subsystems, one of spin-up and one of spin-down electrons; each subsystem is described by the equations from Sec. 4.2.1.

Energy as well as particles can be exchanged between the two spin pools (by collisions and spin-flip processes, respectively). As energy relaxation (tens of femtoseconds) happens usually on much shorter time scales than spin relaxation (picoseconds to nanoseconds), we assume that a local equilibrium exists at each position x . Consequently, both subsystems share a common *local* equilibrium chemical potential $\eta[T(x)]$ and temperature $T(x)$. On the other hand, the local nonequilibrium quasichemical potentials $\mu_\lambda(x)$ can be different for each spin subsystem.

From Eq. (4.4), we obtain

$$n(x) = n_\uparrow^0 \{ \eta[T(x)] + e\mu_\uparrow(x) + e\varphi(x), T(x) \} + n_\downarrow^0 \{ \eta[T(x)] + e\mu_\downarrow(x) + e\varphi(x), T(x) \} \quad (4.14)$$

for the complete local electron density of the system. By expanding the electron density up to the first order in the local nonequilibrium quantities, $\mu_\uparrow(x)$, $\mu_\downarrow(x)$, and $\varphi(x)$, and using the Sommerfeld expansion subsequently to calculate the integrals that enter via Eq. (4.1), we can write the electron density as

$$n(x) = n_0 + \delta n(x). \quad (4.15)$$

Here, we have introduced the local equilibrium density, $n_0 = n_\uparrow^0 \{ \eta[T(x)], T(x) \} + n_\downarrow^0 \{ \eta[T(x)], T(x) \}$, and the local nonequilibrium electron density fluctuations,

$$\delta n(x) = eg [\mu(x) + \varphi(x)] + eg_s \mu_s(x). \quad (4.16)$$

Additionally, we have introduced the quasichemical potential, $\mu = (\mu_\uparrow + \mu_\downarrow)/2$, the spin accumulation, $\mu_s = (\mu_\uparrow - \mu_\downarrow)/2$, as well as the densities of states $g = g_\uparrow(\varepsilon_F) + g_\downarrow(\varepsilon_F)$ and $g_s = g_\uparrow(\varepsilon_F) - g_\downarrow(\varepsilon_F)$ at the Fermi level. We further assume that there is no accumulation of charge inside the conductor under bias $\varphi(x)$. This assumption of local charge neutrality is valid for metals and highly doped semiconductors and requires $n(x) = n_0$.⁵ Hence, Eq. (4.15) yields the condition

$$\delta n(x) = 0. \quad (4.17)$$

⁵In non-degenerate semiconductors one can relax this condition and obtain the resulting nonlinear current-voltage characteristics and bias-dependent spin-injection efficiency [141, 142, 143].

4.2. Spin-polarized transport in the presence of thermal fluctuations

The local spin density,

$$s(x) = n_{\uparrow}^0 \{ \eta [T(x)] + e\mu_{\uparrow}(x) + e\varphi(x), T(x) \} - n_{\downarrow}^0 \{ \eta [T(x)] + e\mu_{\downarrow}(x) + e\varphi(x), T(x) \}, \quad (4.18)$$

can be evaluated analogously to the local electron density: First, Eq. (4.18) is expanded in the local nonequilibrium quantities up to the first order. The resulting integrals are performed employing the Sommerfeld expansion up to the first non-vanishing order and, as a final step, the charge neutrality condition, Eq. (4.17), is used to simplify the result. This procedure yields

$$s(x) = s_0(x) + \delta s(x), \quad (4.19)$$

with the local equilibrium spin density being given by $s_0(x) = n_{\uparrow}^0 \{ \eta [T(x)], T(x) \} - n_{\downarrow}^0 \{ \eta [T(x)], T(x) \}$ and the local nonequilibrium spin density by

$$\delta s(x) = e \frac{g^2 - g_s^2}{g} \mu_s(x). \quad (4.20)$$

It is important to note that $s_0(x)$ is determined by the local temperature $T(x)$, as a result of the rapid energy relaxation as compared to the spin relaxation.

The same procedure can be applied to calculate the energy density from Eq. (4.5),

$$e(x) = e_{\uparrow}^0 \{ \eta [T(x)] + e\mu_{\uparrow}(x) + e\varphi(x), T(x) \} + e_{\downarrow}^0 \{ \eta [T(x)] + e\mu_{\downarrow}(x) + e\varphi(x), T(x) \}, \quad (4.21)$$

which can be split in a local equilibrium energy density, $e_0(x) = e_{\uparrow}^0 \{ \eta [T(x)], T(x) \} + e_{\downarrow}^0 \{ \eta [T(x)], T(x) \}$, and local energy density fluctuations $\delta e(x)$, that is,

$$e(x) = e_0(x) + \delta e(x). \quad (4.22)$$

By calculating $\delta e(x)$ in the same way as $\delta s(x)$, we find that

$$\delta e(x) = 0, \quad (4.23)$$

consistent with our assumption of fast energy relaxation to the local quasiequilibrium. Next, we consider the currents flowing through the system. Since our goal is to calculate the quasichemical and spin quasichemical potentials, as well as the temperature profile, we not only derive transport equations based on Eqs. (4.8) and (4.11), but also continuity equations for each of the currents considered, that is, charge, spin, and heat currents.

The charge current consists of the electric currents carried by spin up and spin down electrons,

$$\begin{aligned} j(x) &= j_{\uparrow}(x) + j_{\downarrow}(x) \\ &= \sigma \nabla \left\{ \frac{\eta [T(x)]}{e} + \mu(x) \right\} + \sigma_s \nabla \mu_s(x) - \frac{1}{2} (S\sigma + S_s\sigma_s) \nabla T(x), \end{aligned} \quad (4.24)$$

4. Theory of thermal spin-charge coupling in electronic systems

where the conductivities are given by $\sigma = \sigma_{\uparrow} + \sigma_{\downarrow}$ and $\sigma_s = \sigma_{\uparrow} - \sigma_{\downarrow}$, and the Seebeck coefficients by $S = S_{\uparrow} + S_{\downarrow}$ and $S_s = S_{\uparrow} - S_{\downarrow}$. In nonmagnetic materials $\sigma_s = 0$ and $S_s = 0$. In our model we consider a steady state, which requires

$$\nabla j(x) = 0, \quad (4.25)$$

that is, a uniform electric current, $j(x) = j$.

The spin current is the difference between the electric currents of spin up and spin down electrons,

$$\begin{aligned} j_s(x) &= j_{\uparrow}(x) - j_{\downarrow}(x) \\ &= \sigma_s \nabla \left\{ \frac{\eta[T(x)]}{e} + \mu(x) \right\} + \sigma \nabla \mu_s(x) - \frac{1}{2} (S_s \sigma + S \sigma_s) \nabla T(x). \end{aligned} \quad (4.26)$$

As we have seen, the spin density $s(x)$ deviates from its local equilibrium value $s_0(x)$. Unlike charge, spin is not conserved and spin relaxation processes lead to a decrease of the local nonequilibrium spin to $s_0(x)$. Therefore, the continuity equation for the spin current is given by

$$\nabla j_s(x) = e \frac{\delta s(x)}{\tau_s}, \quad (4.27)$$

where τ_s is the spin relaxation time. We will not distinguish between different spin-relaxation mechanisms in our model. Instead, we treat τ_s as an effective spin-relaxation time, which incorporates all the different spin-relaxation mechanisms. We stress that spin-relaxation processes bring the nonequilibrium spin $s(x)$ to the (quasi)equilibrium value $s_0(x)$, defined *locally* by $T(x)$. Here, we deviate from the treatment given in Ref. 126.

The heat current,

$$\begin{aligned} j_q(x) &= j_{q,\uparrow}(x) + j_{q,\downarrow}(x) \\ &= \frac{T(S\sigma + S_s\sigma_s)}{2} \nabla \left\{ \frac{\eta[T(x)]}{e} + \mu(x) \right\} + \frac{T(S_s\sigma + S\sigma_s)}{2} \nabla \mu_s(x) - \mathcal{L}T\sigma \nabla T(x), \end{aligned} \quad (4.28)$$

is the heat carried through the system by the electrons of both spin species. Closely related is the energy current,

$$j_u(x) = j_q(x) - \left\{ \frac{\eta[T(x)]}{e} + \mu(x) \right\} j - \mu_s(x) j_s(x). \quad (4.29)$$

By inserting Eqs. (4.24), (4.26), and (4.28) and using that the divergence of the charge current vanishes in a steady state, that is, Eq. (4.25), we find

$$\begin{aligned} \nabla j_u(x) &= \frac{T(x)}{2} \nabla [Sj + S_s j_s(x)] - \mu_s(x) \nabla j_s(x) \\ &\quad - \nabla \left[\mathcal{L}\sigma T(x) \left(1 - \frac{S^2 + S_s^2 + 2SS_s P_\sigma}{4\mathcal{L}} \right) \nabla T(x) \right] - \frac{j_{\uparrow}^2(x)}{\sigma_{\uparrow}} - \frac{j_{\downarrow}^2(x)}{\sigma_{\downarrow}}, \end{aligned} \quad (4.30)$$

4.2. Spin-polarized transport in the presence of thermal fluctuations

where $P_\sigma = \sigma_s/\sigma$ is the conductivity spin polarization. The above formula contains Thomson (first term) as well as Joule heating (final two terms). Equation (4.23) can be used to formulate the continuity equation for the energy current by enforcing the energy conservation,

$$\nabla j_u(x) = 0. \quad (4.31)$$

Thus, if j is treated as an external parameter, the transport equation for the charge current, Eq. (4.24), as well as the transport and continuity equations for the spin and heat currents, Eqs. (4.26), (4.27), (4.28), and (4.31), form a complete set of inhomogeneous differential equations to determine the quasichemical potentials $\mu(x)$ and $\mu_s(x)$, the temperature profile $T(x)$, as well as the currents $j_s(x)$ and $j_q(x)$. The solution to this set of differential equations, that couple charge, spin, and heat transport, will be discussed in the next section.

4.2.3. Spin-diffusion equation and its general solution

In the following, the general solutions to the equations introduced in Sec. 4.2.2 will be discussed. Inserting Eq. (4.26) into the spin-current continuity equation (4.27), and using Eqs. (4.20), (4.24), and (4.25) generalizes the standard [144, 145] spin-diffusion equation,

$$\nabla^2 \mu_s(x) = \frac{\mu_s(x)}{\lambda_s^2} + \frac{1}{2} \nabla \cdot [S_s \nabla T(x)]. \quad (4.32)$$

Here, we have introduced the spin-diffusion length [8, 9]

$$\lambda_s = \sqrt{\tau_s g \sigma (1 - P_\sigma^2) / [e^2 (g^2 - g_s^2)]}. \quad (4.33)$$

As we are primarily interested in linear effects, we neglect the position-dependence of the spin Seebeck coefficient S_s , which enters via $T(x)$, and arrive at a simplified diffusion equation for the spin accumulation,

$$\nabla^2 \mu_s(x) = \frac{\mu_s(x)}{\lambda_s^2} + \frac{S_s}{2} \nabla^2 T(x), \quad (4.34)$$

where S_s is evaluated at the mean temperature T . In order to solve this equation, we need the temperature profile which can be determined from Eq. (4.31). If only first order effects are taken into account, Eq. (4.31) gives the differential equation

$$\nabla^2 T(x) = \frac{2S_s(1 - P_\sigma^2)}{\lambda_s^2 (4\mathcal{L} - S^2 - S_s^2 - 2SS_sP_\sigma)} \mu_s(x), \quad (4.35)$$

deforming the typically linear profile of $T(x)$. The solution to the coupled differential Eqs. (4.34) and (4.35) reads as

$$\mu_s(x) = A \exp\left(\frac{x}{\tilde{\lambda}_s}\right) + B \exp\left(-\frac{x}{\tilde{\lambda}_s}\right), \quad (4.36)$$

4. Theory of thermal spin-charge coupling in electronic systems

$$T(x) = \frac{2S_s(1 - P_\sigma^2)}{4\mathcal{L} - (S + S_s P_\sigma)^2} \mu_s(x) + Cx + D, \quad (4.37)$$

with the modified spin-diffusion length

$$\tilde{\lambda}_s = \lambda_s \sqrt{\frac{4\mathcal{L} - S^2 - S_s^2 - 2SS_s P_\sigma}{4\mathcal{L} - (S + S_s P_\sigma)^2}}. \quad (4.38)$$

Integration of Eq. (4.24) yields the total chemical potential

$$\frac{\eta[T(x)]}{e} + \mu(x) = \frac{j}{\sigma} x - P_\sigma \mu_s(x) + \frac{S + S_s P_\sigma}{2} T(x) + E. \quad (4.39)$$

The integration constants A , B , C , D , and E have to be determined by including the respective boundary conditions of the system under consideration.

If $S_\lambda \ll \sqrt{\mathcal{L}}$ (see the next section), it is often possible to assume a uniform temperature gradient, that is,

$$T(x) = Cx + D. \quad (4.40)$$

Then, Eq. (4.34) reduces to the standard spin-diffusion equation and its solution is given by

$$\mu_s(x) = A \exp\left(\frac{x}{\lambda_s}\right) + B \exp\left(-\frac{x}{\lambda_s}\right), \quad (4.41)$$

while integration of Eq. (4.24) yields the total chemical potential

$$\frac{\eta[T(x)]}{e} + \mu(x) = \left(\frac{j}{\sigma} + \frac{S + S_s P_\sigma}{2} C\right) x - P_\sigma \mu_s(x) + E. \quad (4.42)$$

As before, A , B , C , D , and E are integration constants to be specified by boundary conditions. However, assuming a constant temperature gradient in ferromagnets is not consistent with Eq. (4.31) and therefore this approximation cannot be used in situations that depend crucially on the heat current profile (see next section).

The spin and heat currents can be obtained by inserting the solutions found above into Eqs. (4.26) and (4.28).

4.2.4. Contact properties

To find the specific solution for a system consisting of different materials, such as a F/N junction, we have to know the behavior of the currents at the interfaces between two different materials. The currents at a contact can be obtained by applying Eqs. (4.12) and (4.13), giving

$$j_c = j_{\uparrow c} + j_{\downarrow c} = \Sigma_c \left(\frac{1}{e} \Delta \eta_c + \Delta \mu_c \right) + \Sigma_{sc} \Delta \mu_{sc} - \frac{1}{2} (S_c \Sigma_c + S_{sc} \Sigma_{sc}) \Delta T_c, \quad (4.43)$$

4.3. Ferromagnet placed in a thermal gradient

$$j_{sc} = j_{\uparrow c} - j_{\downarrow c} = \Sigma_{sc} \left(\frac{1}{e} \Delta \eta_c + \Delta \mu_c \right) + \Sigma_c \Delta \mu_{sc} - \frac{1}{2} (S_{sc} \Sigma_c + S_c \Sigma_{sc}) \Delta T_c, \quad (4.44)$$

$$\begin{aligned} j_{qc} = j_{q\uparrow c} + j_{q\downarrow c} &= \frac{T}{2} (S_c \Sigma_c + S_{sc} \Sigma_{sc}) \left(\frac{1}{e} \Delta \eta_c + \Delta \mu_c \right) \\ &+ \frac{T}{2} (S_{sc} \Sigma_c + S_c \Sigma_{sc}) \Delta \mu_{sc} - \mathcal{L} T \Sigma_c \Delta T_c, \end{aligned} \quad (4.45)$$

where ΔT_c is the temperature drop at the contact, and $\Delta \eta_c$, $\Delta \mu_c$, and $\Delta \mu_{sc}$ are the drops of the local equilibrium chemical, quasichemical and spin quasichemical potentials. Moreover, the contact conductances $\Sigma_c = \Sigma_{\uparrow c} + \Sigma_{\downarrow c}$ and $\Sigma_s^c = \Sigma_{\uparrow c} - \Sigma_{\downarrow c}$ as well as the contact thermopowers $S_c = S_{\uparrow c} + S_{\downarrow c}$ and $S_{sc} = S_{\uparrow c} - S_{\downarrow c}$ have been introduced.

Equations (4.43)-(4.45) will be used in Secs. 4.4 and 4.5 to fix the integration constants of the general solutions (4.40)-(4.42) and Eqs. (4.36)-(4.42) found in Sec. 4.2.3.

4.3. Ferromagnet placed in a thermal gradient

As a first example, we consider a ferromagnetic metal F of length L ($-L/2 < x < L/2$) subject to a thermal gradient under open-circuit conditions, that is, $j = 0$. The gradient is applied by creating a temperature difference $\Delta T = T_2 - T_1$ between both ends of the metal, which are held at temperatures T_1 and T_2 , respectively, as shown in Fig. 4.3.

At the ends of the ferromagnet, we impose the boundary conditions $T(-L/2) = T_1$, $T(L/2) = T_2$, and set $j_s(\pm L/2) = 0$. Since we consider only first-order effects, the Seebeck coefficients are assumed to be constant over the length of the ferromagnet and are evaluated at the mean temperature $T = (T_1 + T_2)/2$. Using the above boundary conditions and Eqs. (4.36)-(4.39) yields the spin accumulation

$$\mu_s(x) = \frac{S_s}{2} \tilde{\lambda}_s \frac{\Delta T}{L} \frac{\sinh(x/\tilde{\lambda}_s)}{\cosh(L/2\tilde{\lambda}_s)} \frac{4\mathcal{L} - (S + S_s P_\sigma)^2}{N(L)}, \quad (4.46)$$

and the spin current

$$j_s(x) = -\frac{S_s}{2} \frac{\tilde{\lambda}_s}{\tilde{R}} \frac{\Delta T}{L} \left[1 - \frac{\cosh(x/\tilde{\lambda}_s)}{\cosh(L/2\tilde{\lambda}_s)} \right] \frac{4\mathcal{L} - S^2 - S_s^2 - 2SS_s P_\sigma}{N(L)}, \quad (4.47)$$

where $\tilde{R} = \tilde{\lambda}_s / [\sigma(1 - P_\sigma^2)]$ and

$$N(L) = 4\mathcal{L} - S^2 - S_s^2 - 2SS_s P_\sigma + S_s^2 (1 - P_\sigma^2) \frac{\tanh(L/2\tilde{\lambda}_s)}{L/2\tilde{\lambda}_s}. \quad (4.48)$$

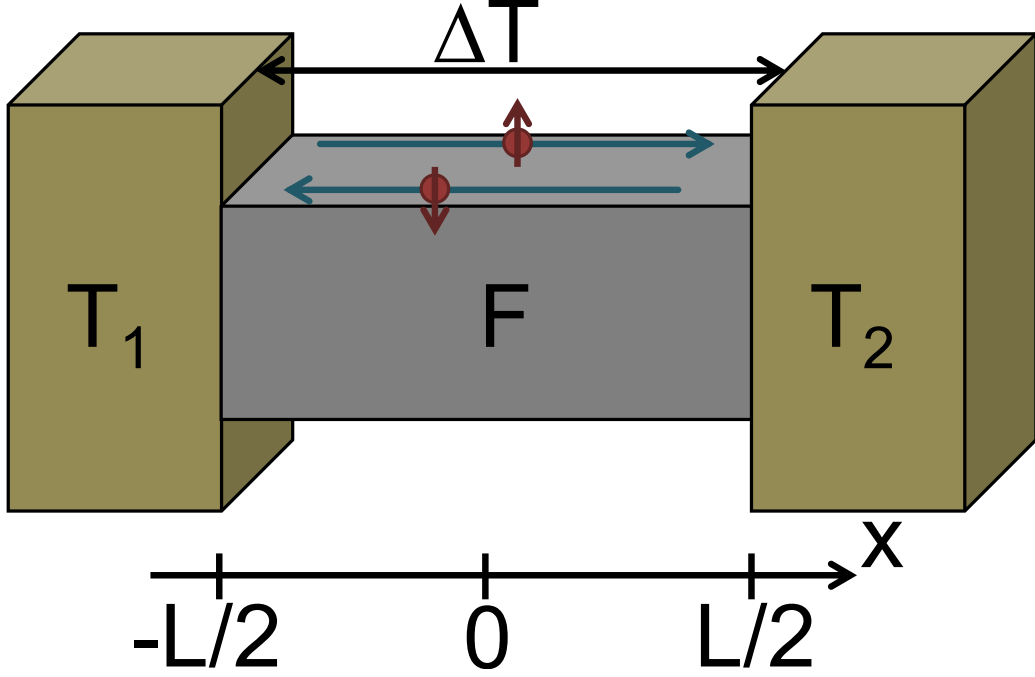


Figure 4.3.: A schematic illustration of a ferromagnet metal placed in a thermal gradient, which leads to the generation of a spin current.

If a constant temperature gradient is assumed and the reduced model given by Eqs. (4.40)-(4.42) is used, the spin accumulation reads as

$$\mu_s(x) = \frac{S_s}{2} \lambda_s \frac{\Delta T}{L} \frac{\sinh(x/\lambda_s)}{\cosh(L/2\lambda_s)}, \quad (4.49)$$

and the spin current

$$j_s(x) = -\frac{S_s}{2} \frac{\lambda_s}{R} \frac{\Delta T}{L} \left[1 - \frac{\cosh(x/\lambda_s)}{\cosh(L/2\lambda_s)} \right], \quad (4.50)$$

where $R = \lambda_s / [\sigma(1 - P_\sigma^2)]$ is the effective resistance of the ferromagnet.

For metals $S_\lambda \ll \sqrt{\mathcal{L}}$ and Eqs. (4.46) and (4.47) reduce to Eqs. (4.49) and (4.50), that is, the assumption of a uniform temperature gradient $\nabla T = \Delta T/L$ is justified. Only at the boundaries of the sample both temperature profiles differ (insignificantly) as there is a small exponential decay within the spin-diffusion length $\tilde{\lambda}_s \approx \lambda_s$ if the full model is used compared to a perfectly linear temperature profile of the reduced model.

Equations (4.49) and (4.50) from the reduced model correspond to the profiles of the spin accumulation and spin current found in Ref. 146, where a Boltzmann equation approach has been used to describe thermoelectric spin diffusion in a ferromagnetic metal.

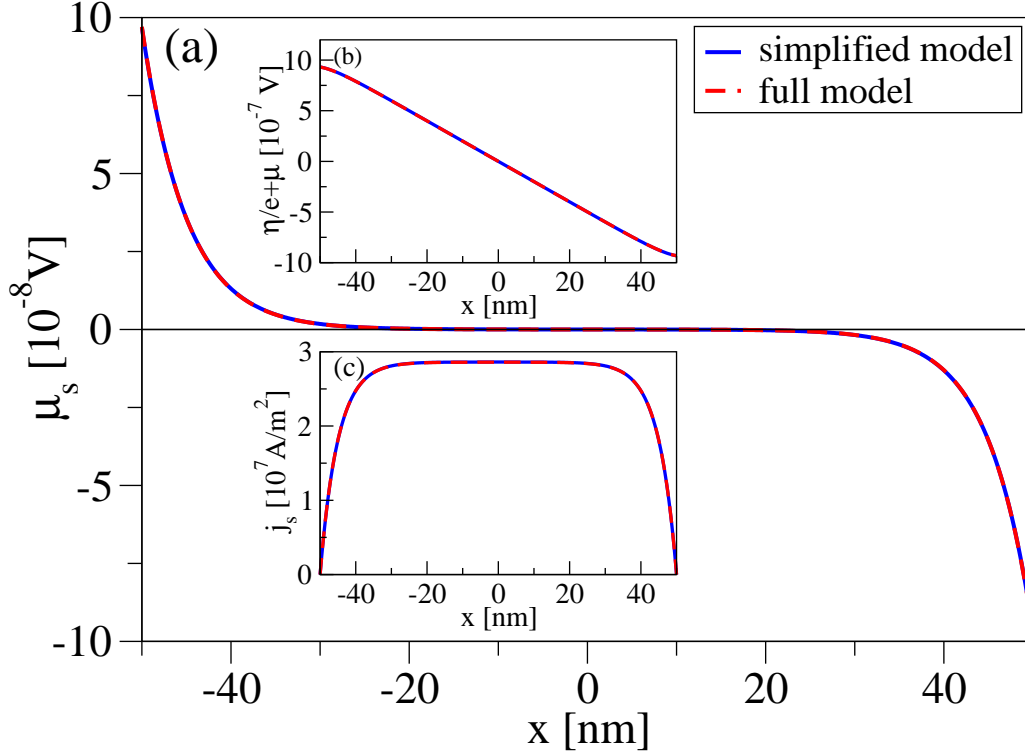


Figure 4.4.: Profiles of the (a) spin accumulation, the (b) total chemical potential, and the (c) spin current for $\text{Ni}_{81}\text{Fe}_{19}$ at $T = 300$ K with $L = 100$ nm and $\Delta T = 100$ mK. The solid lines show the results obtained if a constant temperature gradient $\nabla T = \Delta T/L_F$ is assumed, while the dashed lines (fully overlapping with the solid ones) show the results obtained if the temperature profile is determined by $\nabla j_u = 0$.

In Fig. 4.4, the results calculated for a model $\text{Ni}_{81}\text{Fe}_{19}$ film with realistic parameters [126] [$\lambda_s = 5$ nm, $\sigma = 2.9 \times 10^6$ 1/ Ωm , $S_0 = (S_\uparrow \sigma_\uparrow + S_\downarrow \sigma_\downarrow)/(\sigma_\uparrow + \sigma_\downarrow) = -2.0 \times 10^{-5}$ V/K with $P_\sigma = 0.7$ and $P_S = (S_\uparrow - S_\downarrow)/(S_\uparrow + S_\downarrow) = 3.0$] at a mean temperature $T = 300$ K are displayed. The length of the sample is $L = 100$ nm and the temperature difference is $\Delta T = 100$ mK. As can be seen in Fig. 4.4, the agreement between both solutions is very good.

Figure 4.4 (b) shows an almost linear drop of the total chemical potential between both ends of the ferromagnet. Only at the contacts is this linear drop superimposed by an exponential decay. It is also at the contacts that nonequilibrium spin accumulates and decays within the spin-diffusion length [see Figs. 4.4 (a) and 4.4 (c)]. Thus, only near the contacts is there an electronic contribution to the spin voltage and our electronic model does not reproduce the linear inverse spin Hall voltage observed in this system [123], which suggests that a mechanism different from electronic spin diffusion is responsible for the detected spin Hall voltage [146]. Also, the “entropic” terms in the spin accumulation as introduced in Ref. 126, which would lead to a

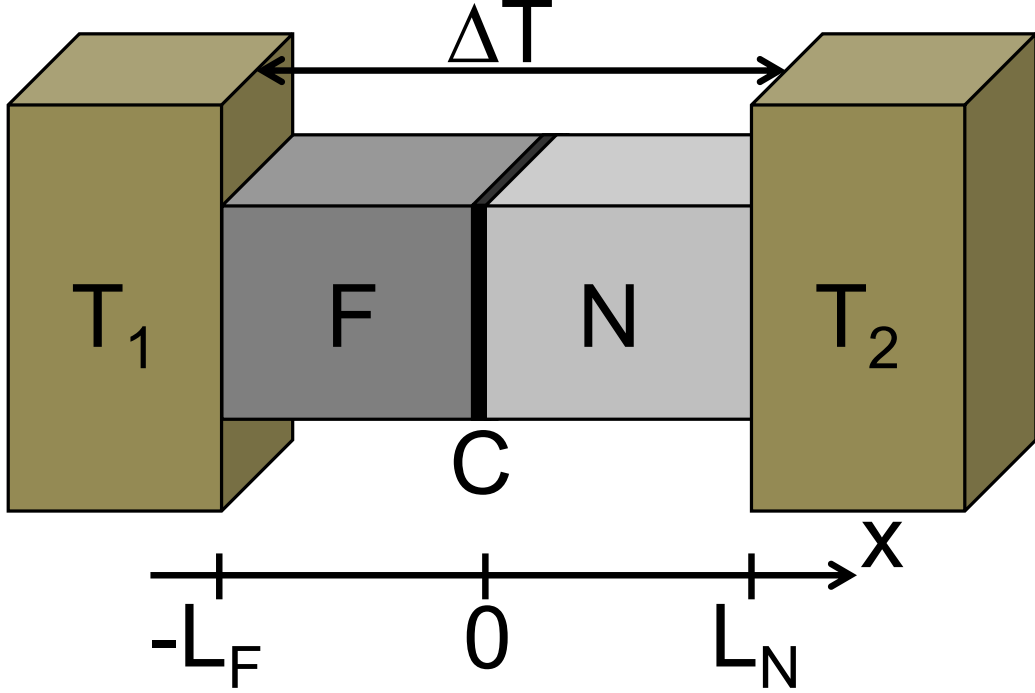


Figure 4.5.: A schematic illustration of a F/N junction placed in a thermal gradient.

uniform decay of the spin accumulation across the whole sample, not just at the distances of the spin-diffusion lengths off of the edges, do not arise in our theory.

4.4. F/N junctions

4.4.1. F/N junctions placed in thermal gradients

In this section, we investigate an open ($j = 0$) F/N junction under a thermal gradient. The F/N junction consists of a ferromagnet and a nonmagnetic conductor, denoted by the additional subscripts F and N in the quantities defined in the previous sections. The extension of the ferromagnet is given by $-L_F < x < 0$, whereas the nonmagnetic conductor is described by values $0 < x < L_N$. We also assume that the properties of the contact region C, located at $x = 0$, are known. By coupling the F and N regions to reservoirs with different temperatures, T_2 and T_1 , respectively, a temperature gradient is created across the junction. The model investigated in the following is summarized in Fig. 4.5.

As in the previous section, we can assume uniform (but for each region different) temperature gradients ∇T_F and ∇T_N and use the simplified spin-diffusion equation (4.34), and the corresponding solutions (4.40)-(4.42), to describe the total chemical potential, the spin accumulation, and the temperature profile in each region separately.

The integration constants are solved invoking the following boundary conditions: $T(-L_F) = T_1$, $T(L_N) = T_2$, and $j_s(-L_F) = j_s(L_N) = 0$. Furthermore, we use Eqs. (4.43)-(4.45) and assume, as in the standard spin-injection model [9], that the charge, spin, and heat currents are continuous at the interface, giving us five additional equations for the integration constants. From this set of equations, the integration constants, including the gradients ∇T_F and ∇T_N , can be obtained. Depending on the choice of the direction of the gradient, one finds that spin is either injected from the F region into the N region or extracted from the N region by a pure spin current, that is, a spin current without accompanying charge current.

In order to measure the efficiency of the thermal spin injection [$j_s(0) < 0$] and extraction [$j_s(0) > 0$] at the interface, we calculate the *thermal spin-injection efficiency* $\kappa = j_s(x=0)/\nabla T_N$, which corresponds to a spin thermal conductivity. Our model gives

$$\kappa = - \frac{\sigma_N \tanh(L_N/\lambda_{sN})}{2 [R_F \tanh(L_N/\lambda_{sN}) + R_c \tanh(L_N/\lambda_{sN}) \tanh(L_F/\lambda_{sF}) + R_N \tanh(L_F/\lambda_{sF})] \times \{ \tanh(L_F/\lambda_{sF}) S_{sc} R_c (1 - P_\Sigma^2) + [1 - \cosh^{-1}(L_F/\lambda_{sF})] S_{sF} R_F (1 - P_{\sigma F}^2) \}}, \quad (4.51)$$

with the effective resistances for the F, N, and contact regions,

$$R_N = \lambda_{sN}/\sigma_N, \quad (4.52)$$

$$R_F = \lambda_{sF}/[\sigma_F(1 - P_{\sigma F}^2)], \quad (4.53)$$

$$R_c = 1/[\Sigma_c(1 - P_\Sigma^2)], \quad (4.54)$$

and the contact conductance spin polarization

$$P_\Sigma = \Sigma_{sc}/\Sigma_c. \quad (4.55)$$

Equation (4.51) has been derived in the limit of $S_{\lambda F/N/c} \ll \sqrt{\mathcal{L}}$, in which the temperature gradients are given by

$$\nabla T_F = \frac{\Delta T}{\sigma_F \mathcal{R}_{FN}}, \quad (4.56)$$

$$\nabla T_N = \frac{\Delta T}{\sigma_N \mathcal{R}_{FN}}, \quad (4.57)$$

where

$$\mathcal{R}_{FN} = \frac{L_F}{\sigma_F} + \frac{1}{\Sigma_c} + \frac{L_N}{\sigma_N}. \quad (4.58)$$

If the sample sizes are large, that is, if $L_F \gg \lambda_{sF}$ and $L_N \gg \lambda_{sN}$, as is usually the case (but not in Figs. 4.6 and 4.7 where $L_N < \lambda_{sN}$), the situation at the interface is

4. Theory of thermal spin-charge coupling in electronic systems

not sensitive to the boundary conditions far away from the interface and Eq. (4.51) reduces to

$$\begin{aligned}\kappa &= -\frac{\sigma_N}{2} \frac{S_{sc}R_c(1 - P_\Sigma^2) + S_{sF}R_F(1 - P_{\sigma F}^2)}{R_F + R_c + R_N} \\ &= -\frac{\sigma_N}{2} \langle S_s(1 - P_\sigma^2) \rangle_R,\end{aligned}\quad (4.59)$$

where $\langle \dots \rangle_R$ denotes an average over the effective resistances. The above expressions for the spin-injection efficiency and the gradients, Eqs. (4.51)-(4.59), could have also been obtained by using Eqs. (4.36)-(4.39) to calculate the profiles and taking the limit $S_{\lambda F/N/c} \ll \sqrt{\mathcal{L}}$. Equation (4.59) is the spin-heat coupling equivalent of the well-known formula for the electrical spin-injection efficiency [8, 9].

Using the spin-injection efficiency, Eq. (4.51) [or Eq. (4.59) for large devices], the profiles of the spin current and accumulation in the N region ($0 < x < L_N$) can be written compactly as

$$j_s(x) = -\kappa \nabla T_N \frac{\sinh[(x - L_N)/\lambda_{sN}]}{\sinh(L_N/\lambda_{sN})} \quad (4.60)$$

and

$$\mu_s(x) = -R_N \kappa \nabla T_N \frac{\cosh[(x - L_N)/\lambda_{sN}]}{\sinh(L_N/\lambda_{sN})}, \quad (4.61)$$

which reduce to

$$j_s(x) = \kappa \nabla T_N \exp(-x/\lambda_{sN}) \quad (4.62)$$

and

$$\mu_s(x) = -R_N \kappa \nabla T_N \exp(-x/\lambda_{sN}) \quad (4.63)$$

for $L_N \gg \lambda_{sN}$. In particular, at the contact the spin accumulation in the nonmagnetic material can be calculated as

$$\mu_s(0^+) = -R_N \kappa \nabla T_N \coth(L_N/\lambda_{sN}). \quad (4.64)$$

Equation (4.51) also makes it clear that whether there is spin injection or extraction depends not only on the direction of the temperature gradient, but also on the specific materials chosen.

Another quantity of interest is the total drop of the chemical potential across the F/N junction,

$$\Delta(\eta/e + \mu) = [\eta(T_2) - \eta(T_1)]/e + \mu(L_N) - \mu(-L_F), \quad (4.65)$$

because, in analogy to the calculation of the total resistance of the F/N junction in the case of the electrical spin injection [9], it allows us to define the total Seebeck coefficient S of the device, which can be separated into an equilibrium and a nonequilibrium contribution:

$$\Delta(\eta/e + \mu) \equiv S \Delta T \equiv (S_0 + \delta S) \Delta T. \quad (4.66)$$

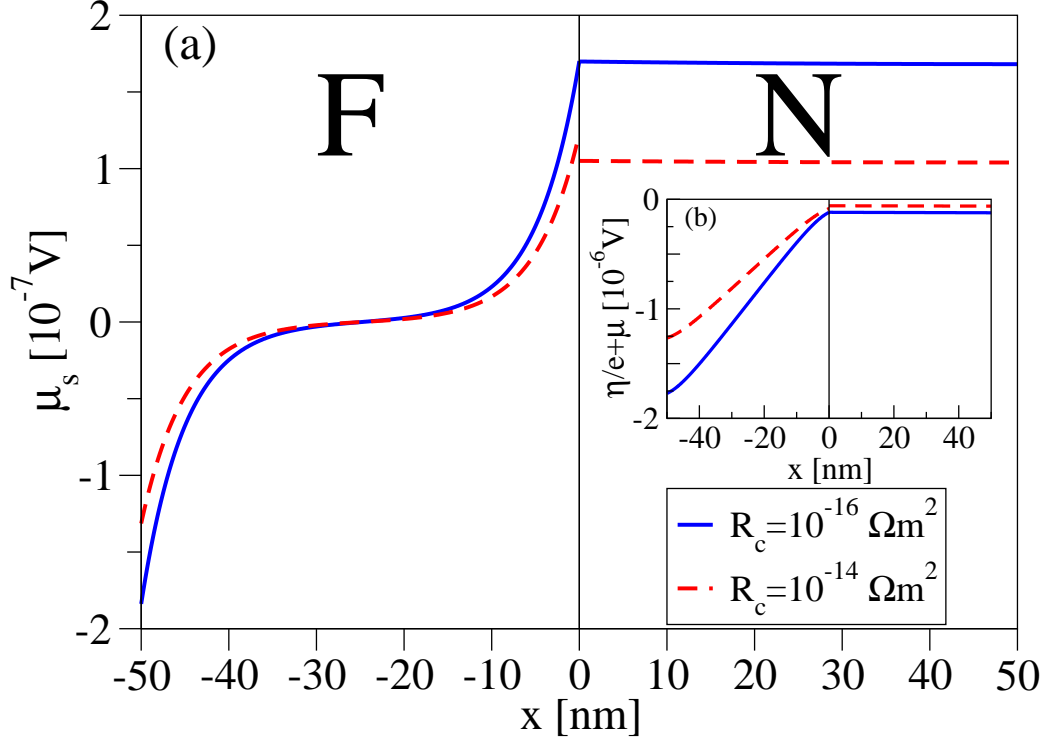


Figure 4.6.: Profiles of the (a) spin accumulation and the (b) total chemical potential for a $\text{Ni}_{81}\text{Fe}_{19}/\text{Cu}$ junction at $T = 300$ K with $L_F = L_N = 50$ nm and $\Delta T = -100$ mK. The solid lines show the results for $R_c = 1 \times 10^{-16} \Omega\text{m}^2$, the dashed lines for $R_c = 1 \times 10^{-14} \Omega\text{m}^2$.

Here,

$$S_0 = \frac{(S_F + S_{sF}P_{\sigma F}) \frac{L_F}{\sigma_F} + (S_c + S_{sc}P_\Sigma) \frac{1}{\Sigma_c} + S_N \frac{L_N}{\sigma_N}}{2\mathcal{R}_{FN}} \quad (4.67)$$

denotes the Seebeck coefficient of the F/N junction in the absence of spin accumulation, whereas

$$\delta S = \frac{P_{\sigma F} [\mu_s(-L_F) - \mu_s(0^-)] + P_\Sigma [\mu_s(0^-) - \mu_s(0^+)]}{\Delta T} \quad (4.68)$$

is the nonequilibrium contribution to the Seebeck coefficient due to spin accumulation. If the extensions of the F/N junction are much larger than the spin-diffusion lengths, the nonequilibrium Seebeck coefficient can be expressed as

$$\delta S = \frac{\frac{S_{sF}\lambda_{sF}(P_\Sigma - 2P_{\sigma F})}{2\sigma_F} + \frac{\kappa[(P_\Sigma - P_{\sigma F})R_F + P_\Sigma R_N]}{\sigma_N}}{\mathcal{R}_{FN}}. \quad (4.69)$$

For illustration, the profiles of the total chemical potential and the spin accumulation are displayed in Fig. 4.6 for a junction consisting of $\text{Ni}_{81}\text{Fe}_{19}$ (see Sec. 4.3 for the

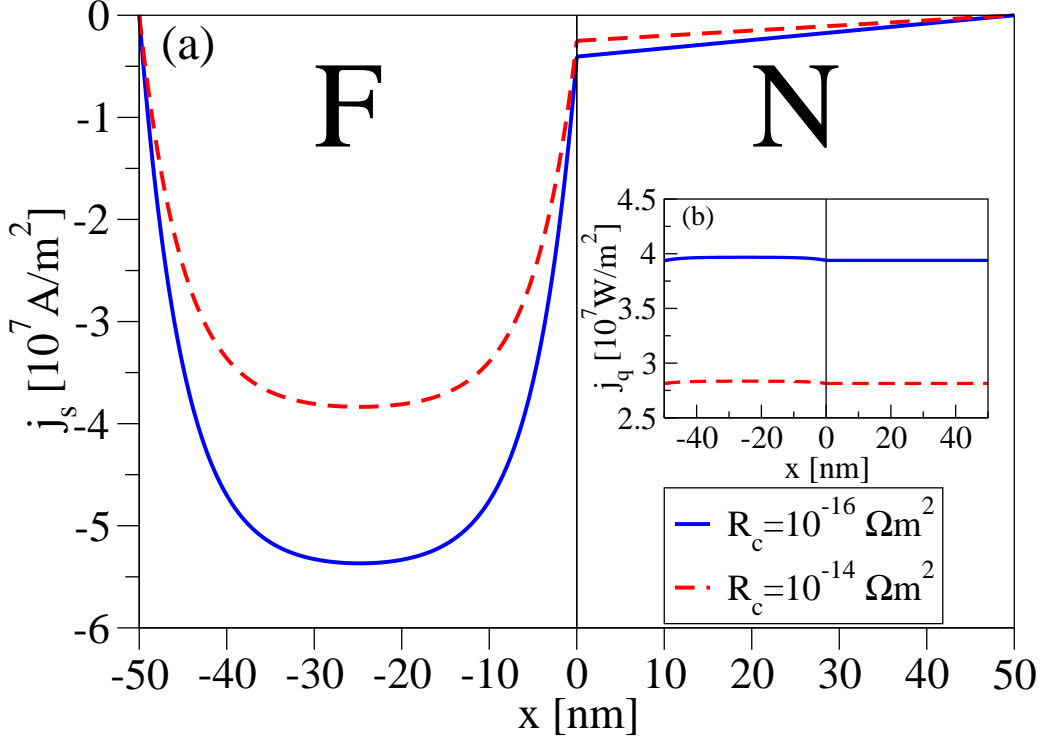


Figure 4.7.: Profiles of the (a) spin current and the (b) heat current for a $\text{Ni}_{81}\text{Fe}_{19}/\text{Cu}$ junction at $T = 300$ K with $L_F = L_N = 50$ nm and $\Delta T = -100$ mK. The solid lines show the results for $R_c = 1 \times 10^{-16} \Omega\text{m}^2$, the dashed lines for $R_c = 1 \times 10^{-14} \Omega\text{m}^2$.

corresponding parameters) and Cu ($\lambda_{sN} = 350$ nm, $\sigma_N = 5.88 \times 10^7$ 1/ Ωm , $S_N = 1.84 \times 10^{-6}$ V/K) with a temperature difference $\Delta T = T_2 - T_1 = -100$ mK between both ends of the junction and the mean temperature $T = 300$ K [136, 147, 126]. Figure 4.7 shows the spin and heat currents for the same system. In Figs. 4.6 and 4.7 we have chosen $R_c = 1 \times 10^{-16} \Omega\text{m}^2$ and $R_c = 1 \times 10^{-14} \Omega\text{m}^2$, as well as $P_\Sigma = 0.5$, $S_c = -1.0 \times 10^{-6}$ V/K, and $S_{sc} = 0.5S_c$ [147]. There is a drop of the total chemical potential across the junction [see Fig. 4.6 (b)]. For the chosen parameters, spin is injected from the F region into the N region, where nonequilibrium spin accumulates at the F/N interface and decays within the spin-diffusion length [see Figs. 4.6 (a) and 4.7 (a) where $L_N < \lambda_{sN}$]. By applying the temperature difference ΔT into the opposite direction, that is, by choosing $T_1 < T_2$, the situation reverses and spin would be extracted from the N region. Figure 4.6 (a) also illustrates that the spin accumulation in the N region decreases with increasing contact resistance. The heat current flows from the hot to the cold end of the junction [$j_q(x) > 0$], as can be seen in Fig. (4.7) (b). Furthermore, one can observe that in the F region the heat current

is not perfectly constant and decreases at $x = -L_F$ as well as at the contact,⁶ while in the N region the heat current remains constant.

We now discuss two important cases: transparent and tunnel contacts in large F/N junctions where $L_F \gg \lambda_{sF}$ and $L_N \gg \lambda_{sN}$. For transparent contacts $R_c \ll R_F, R_N$ and the spin-injection efficiency reduces to

$$\kappa = -\frac{\sigma_N}{2} \frac{S_{sF} R_F (1 - P_{\sigma F}^2)}{R_F + R_N}. \quad (4.70)$$

Thermal electronic spin injection from a ferromagnetic metal to a semiconductor, that is, the case of $R_N \gg R_F$, would suffer from the same "conductivity/resistance mismatch problem" [8, 109, 148, 149] as the usual electrical spin injection does. The nonequilibrium Seebeck coefficient can then be written as

$$\delta S = -\frac{S_{sF} \lambda_{sF} P_{\sigma F}}{2\sigma_F (L_F/\sigma_F + L_N/\sigma_N)} \left(1 + \frac{R_N}{R_F + R_N}\right). \quad (4.71)$$

In this case, κ and δS are restricted only by the individual effective resistances R_F and R_N of the F and N regions. Moreover, the spin accumulation μ_s is continuous at transparent contacts, that is, $\mu_s(0^+) = \mu_s(0^-)$ and Eq. (4.64) yields the expression found in Ref. 136 for $\mu_s(0)/\nabla T_F$.⁷

Tunnel contacts, on the other hand, have very large effective resistances $R_c \gg R_F, R_N$ for which Eqs. (4.59) and (4.69) reduce to

$$\kappa = -\frac{\sigma_N}{2} S_{sc} (1 - P_{\Sigma}^2) \quad (4.72)$$

and

$$\delta S = \frac{\frac{S_{sF} \lambda_{sF} (P_{\Sigma} - 2P_{\sigma F})}{2\sigma_F} + \frac{S_{sc} (1 - P_{\Sigma}^2) [P_{\sigma F} R_F - P_{\Sigma} (R_F + R_N)]}{2}}{\mathcal{R}_{FN}}. \quad (4.73)$$

The thermal spin-injection efficiency for the tunnel junction is determined by the spin-polarization properties of the contact and the conductivity mismatch issue does not arise in this case. A similar result has also been obtained recently in Ref. 150.

4.4.2. Interplay between thermal gradients and simultaneous charge currents

Another interesting effect is the interplay between a thermal gradient across the F/N junction and a simultaneous charge current (see Fig. 4.8). To analyze this process, we take Eqs. (4.40)-(4.42), this time with a finite charge current j , and replace the

⁶This is due to the assumption of constant temperature gradients and would not be the case if the full model was used.

⁷Here, we use that $\nabla T_N = (\sigma_F/\sigma_N)\nabla T_F$.

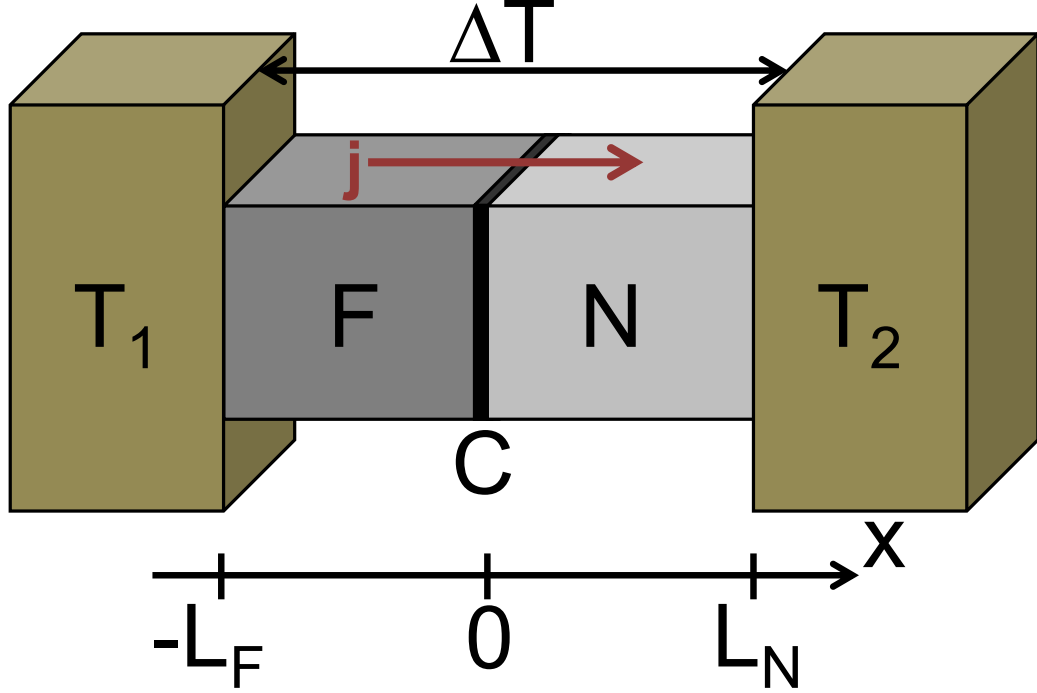


Figure 4.8.: A schematic illustration of a F/N junction placed in a thermal gradient with a charge current being simultaneously driven through the junction.

boundary condition for the spin current at $x = -L_F$ by $j_s(-L_F) = P_{\sigma F} j$ while leaving the boundary conditions for the temperature unchanged and also taking $j_s(L_N) = 0$ as before. By choosing the charge current $j = j_{\text{com}}$ appropriately, the effects of the charge current and the thermal gradient, each by itself applicable for injecting spin into the N region or extracting spin from it, can cancel each other out. As a result, we find that for $L_F \gg \lambda_{sF}$, a charge current

$$j_{\text{com}} = \frac{R_F (1 - P_{\sigma F}^2) S_{sF} + R_c (1 - P_{\Sigma}^2) S_s^c}{2\mathcal{R}_{FN} (R_F P_{\sigma F} + R_c P_{\Sigma})} \Delta T \quad (4.74)$$

extracts (injects) the spin injected (extracted) through a given temperature difference ΔT with no net spin current in the N region.

This effect is shown in Figs. 4.9 and 4.10 for the $\text{Ni}_{81}\text{Fe}_{19}/\text{Cu}$ junction investigated in this section (see above). We find that a current density of $j_{\text{com}} = 7.6 \times 10^7 \text{ A/m}^2$ ($j_{\text{com}} = 1.9 \times 10^7 \text{ A/m}^2$) is needed to compensate a temperature difference of $\Delta T = -100 \text{ mK}$ if $R_c = 1 \times 10^{-16} \Omega\text{m}^2$ ($R_c = 1 \times 10^{-14} \Omega\text{m}^2$). Figures 4.9 (a) and 4.10 (a) show that there is no spin accumulation and no spin current in the nonmagnetic material under the compensating electric current condition. The drop of the chemical potential across the F/N junction is shown in Fig. 4.9 (b) and the heat current flowing from the hot to the cold end of the junction in Fig. 4.10 (b).

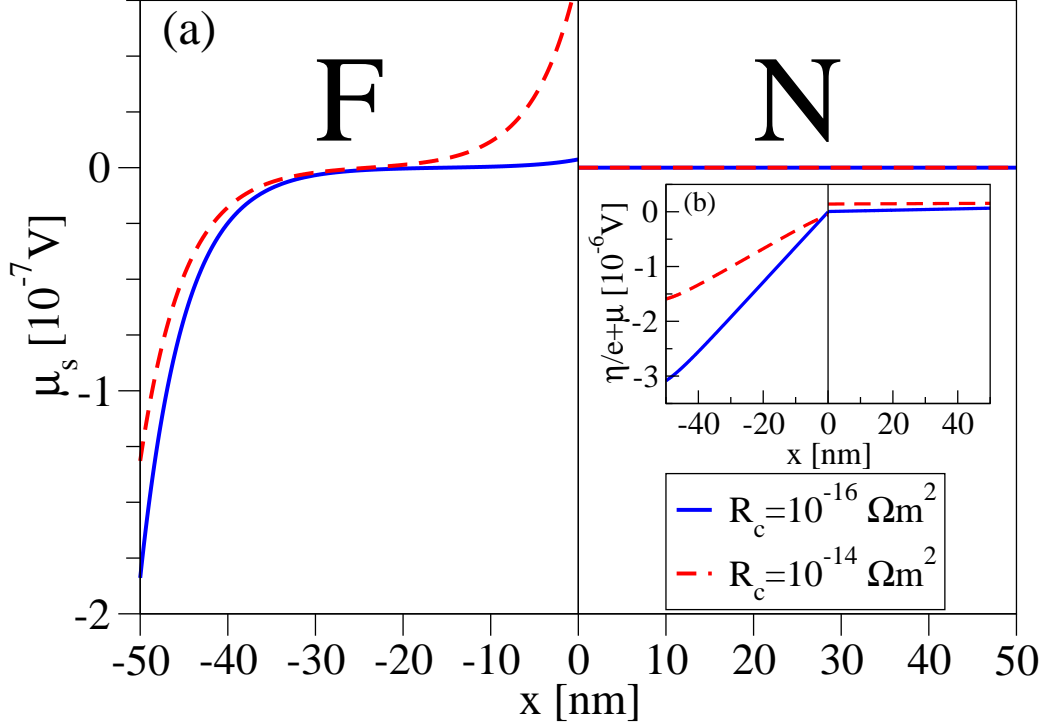


Figure 4.9.: Profiles of the (a) spin accumulation and the (b) total chemical potential for a $\text{Ni}_{81}\text{Fe}_{19}/\text{Cu}$ junction at $T = 300$ K with $L_F = L_N = 50$ nm and $\Delta T = -100$ mK if an electric current compensates the spin accumulation due to the thermal gradient. The solid lines show the results for $R_c = 1 \times 10^{-16} \Omega\text{m}^2$, the dashed lines for $R_c = 1 \times 10^{-14} \Omega\text{m}^2$.

The spin-injection compensation should be useful for experimental investigation of the purely electronic contribution to the spin Seebeck effect.

Moreover, we remark that j_{com} can be used to describe the efficiency of thermal spin injection if one investigates an open-circuit F/N junction ($j = 0$) placed in a thermal gradient as above. In this case, the spin current at the interface $j_s(x = 0)$ is described by Eqs. (4.51) or (4.59), respectively. We can then define the ratio between the spin current at the interface and the charge current one would have to drive through the junction to cancel the thermal spin injection, $P = j_s(x = 0)/j_{\text{com}}$. For large devices and $S_{\lambda F/N/c} \ll \sqrt{\mathcal{L}}$, this ratio can be calculated as

$$P = -\langle P_\sigma \rangle_R, \quad (4.75)$$

which represents the negative spin-injection efficiency of the electrical spin injection [9].

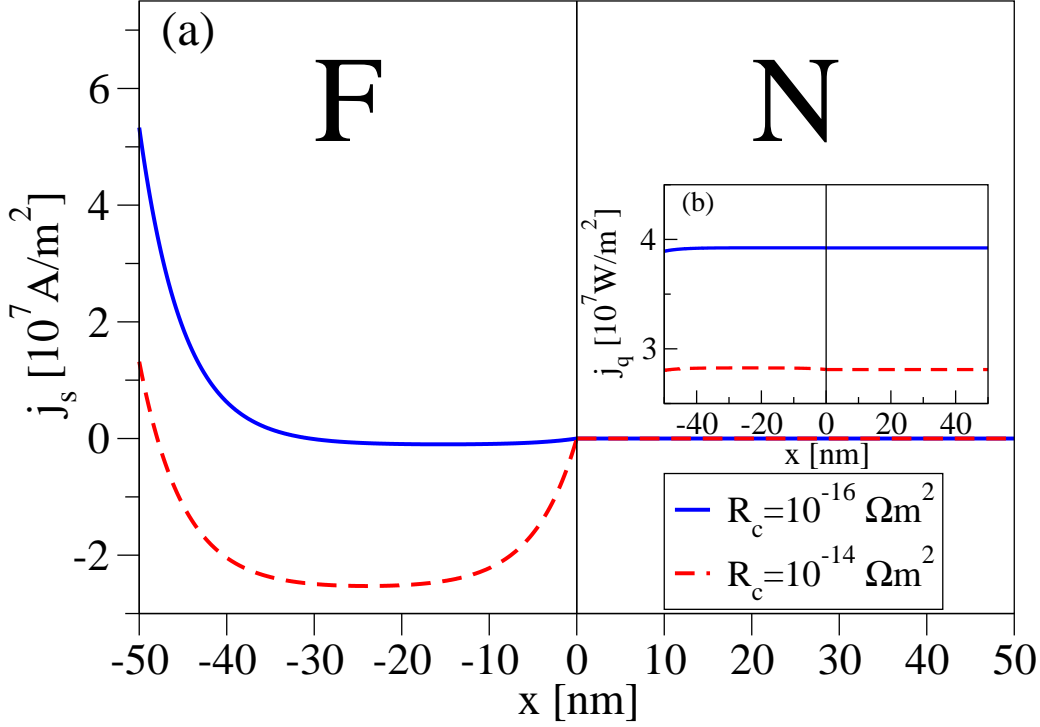


Figure 4.10.: Profiles of the (a) spin current and the (b) heat current for a $\text{Ni}_{81}\text{Fe}_{19}/\text{Cu}$ junction at $T = 300$ K with $L_F = L_N = 50$ nm and $\Delta T = -100$ mK if an electric current compensates the spin accumulation due to the thermal gradient. The solid lines show the results for $R_c = 1 \times 10^{-16} \Omega\text{m}^2$, the dashed lines for $R_c = 1 \times 10^{-14} \Omega\text{m}^2$.

4.4.3. Peltier effects in F/N junctions

As mentioned above, the spin-dependent Peltier effect describes the heating or cooling at the interface between a ferromagnetic and normal conductor driven by a spin current [135]. In the following, we study several different setups in which a spin current passes through the interface of an isothermal (or nearly isothermal) F/N junction and which therefore give rise to the spin-dependent Peltier effect.

For every setup investigated in this section, we assume $L_{N/F} \gg \lambda_{sN/F}$. The first setup considered is the electrical spin injection in a F/N junction: An electric current is driven across an isothermal F/N junction, that is, $\nabla T = 0$ [see Fig. 4.11 (a)]. Since the entire junction is kept at constant temperature, the continuity of the heat and energy current [Eq. (4.31)] does not apply and it is sufficient to solve just Eqs. (4.24), (4.26), and (4.27), that is, the formulas obtained for the electrical spin injection can be used. The spin current at the interface is given by [9]

$$j_s(0) = \frac{P_{\sigma F} R_F + P_{\Sigma} R_c}{R_F + R_c + R_N} j = \langle P_{\sigma} \rangle_R j. \quad (4.76)$$

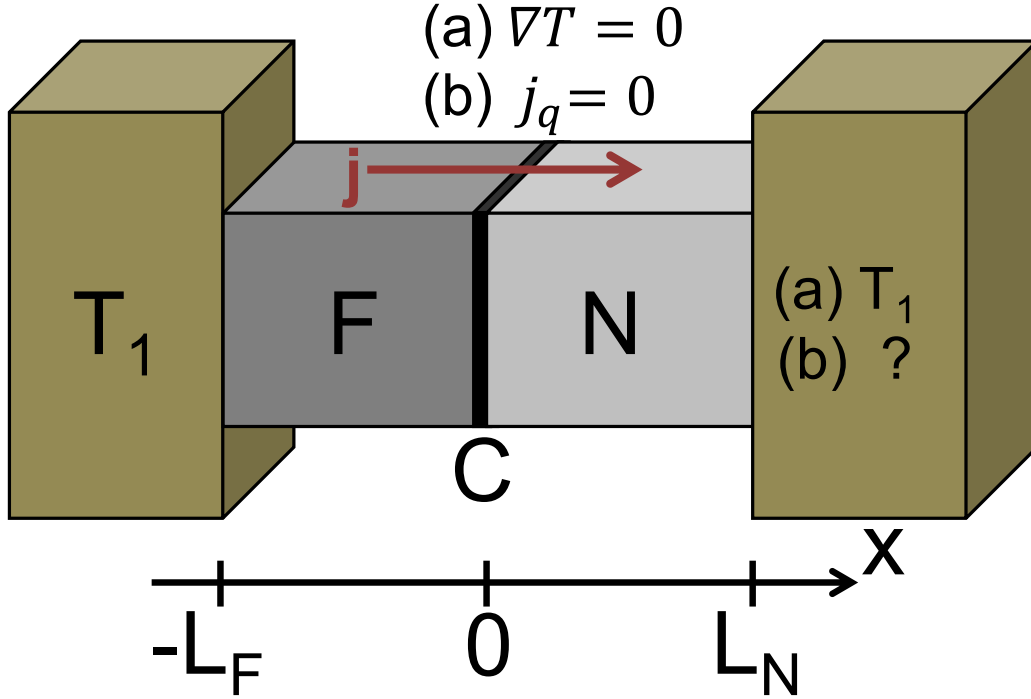


Figure 4.11.: A schematic illustration of a F/N junction in the electrical spin-injection setup, where (a) refers to an isothermal junction and (b) to the situation where $j_q(x) = 0$. The fact that in (b) the temperature at one end of the junction is not given as an external boundary condition, but has to be calculated from the model is implied by “?”.

For constant temperature profiles the heat current, Eq. (4.28), is not continuous at the interface and reads as

$$j_q(x) = \frac{TS_F}{2}j + \frac{TS_{sF}}{2}j_s(x), \quad x < 0 \quad (4.77)$$

and

$$j_q(x) = \frac{TS_N}{2}j, \quad x > 0. \quad (4.78)$$

Therefore, the total heat produced (dissipated) per time at the interface is given by

$$\Gamma_q^{\text{tot}} = j_q(0^-) - j_q(0^+) = \Gamma_q + \Gamma_q^s, \quad (4.79)$$

where

$$\Gamma_q = \frac{T(S_F - S_N)j}{2} \quad (4.80)$$

and

$$\Gamma_q^s = \frac{TS_{sF}\langle P_\sigma \rangle_R j}{2} \quad (4.81)$$

4. Theory of thermal spin-charge coupling in electronic systems

denote the rates of heat production (dissipation) due to the conventional (charge) Peltier and spin-dependent Peltier effects.

If the temperature is fixed at just one end of the junction, a temperature drop arises across the F/N junction due to the heat evolution at the interface. In order to estimate this temperature drop, we follow the approach used in Ref. 135 and investigate the hypothetical situation where no heat enters or leaves the F/N junction and no heat is generated inside the junction, that is, $j_q(x) = 0$ [see Fig. 4.11 (b)]. For $S_\lambda \ll \sqrt{\mathcal{L}}$, the profiles of the chemical potential, the spin accumulation, and the spin current are nearly identical in the cases of an isothermal F/N junction and a F/N junction with $j_q(x) = 0$ (see the following), and Eq. (4.82) should give a good estimate for the temperature difference arising across the junction due to the heating or cooling at the interface.

Thus, instead of $\nabla T = 0$, we apply the condition $j_q(x) = 0$ for any x . This situation requires us to solve the full system of differential equations given by Eqs. (4.24), (4.26), (4.27), (4.28), and (4.31). Since this situation depends crucially on the heat current [via $j_q(x) = 0$], the full solution given by Eqs. (4.36)-(4.39) has to be used, which, in contrast to the assumption of constant gradients in each region, ensures constant heat currents. The temperature far away from the interface is fixed at a given value for one region [for example, at T_1 in the F region as shown in Fig. 4.11 (b)]. At the interface, we impose the boundary conditions that the charge, spin, and heat currents given by Eqs. (4.43)-(4.45) have to be continuous. As before, we assume that $L_{N/F} \gg \lambda_{sN/F}$, in which case the situation at the interface is not sensitive to the boundary conditions far away from the interface. Thus, we choose $\lim_{x \rightarrow \pm\infty} \mu_s(x) = 0$ as boundary conditions for convenience.

The quantity we are interested in is the temperature drop across the entire junction, which can be obtained as

$$\Delta T = \Delta T_{\text{ch}} + \Delta T_s. \quad (4.82)$$

As usual, $S_{\lambda F/N/c} \ll \sqrt{\mathcal{L}}$ and the conventional contribution to the temperature drop then reads as

$$\Delta T_{\text{ch}} = \left[\frac{(S_F + S_{sF} P_{\sigma F}) L_F}{2\mathcal{L}\sigma_F} + \frac{S_c + S_{sc} P_\Sigma}{2\mathcal{L}\Sigma_c} \frac{S_N L_N}{2\mathcal{L}\sigma_N} \right] j, \quad (4.83)$$

while the contribution due to the spin accumulation in the region around the interface can be obtained from

$$\Delta T_s = \frac{S_{sF} (1 - P_{\sigma F}^2)}{2\mathcal{L}} \mu_s(0^-) + \frac{S_{sc} (1 - P_\Sigma^2)}{2\mathcal{L}} [\mu_s(0^+) - \mu_s(0^-)]. \quad (4.84)$$

In this limit, the spin current at the interface is given by the same expression as in

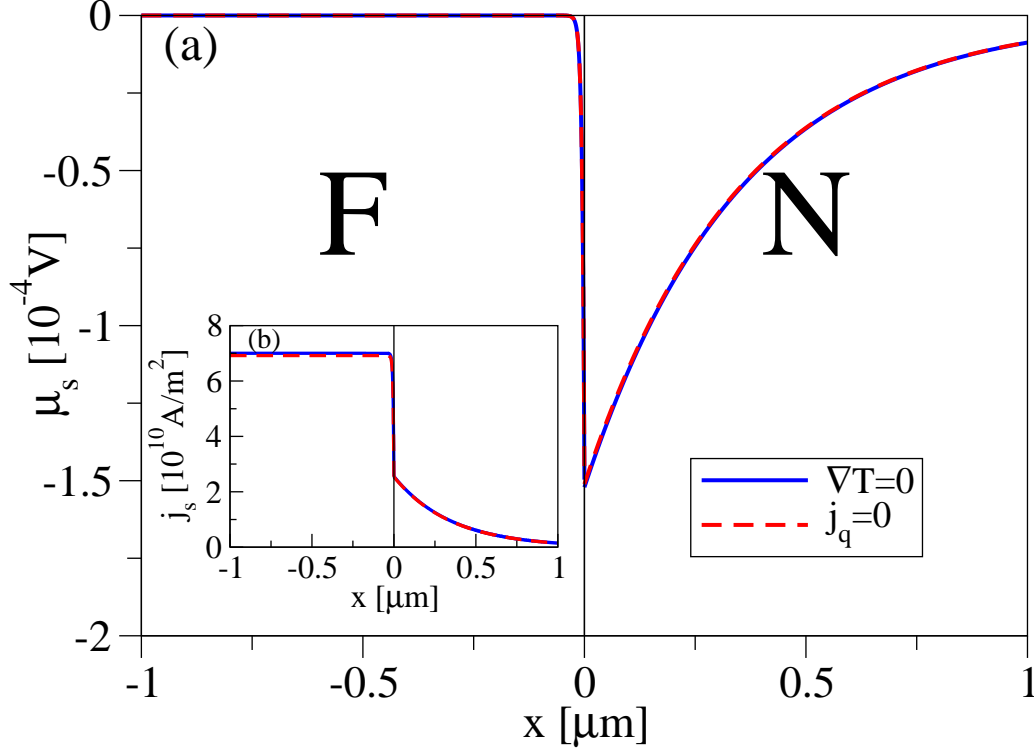


Figure 4.12.: Profiles of the (a) spin accumulation and the (b) spin current for a $\text{Ni}_{81}\text{Fe}_{19}/\text{Cu}$ junction with $L_F = L_N = 1 \mu\text{m}$, $R_c = 1 \times 10^{-16} \Omega\text{m}^2$, and $j = 10^{11} \text{ A/m}^2$. The solid lines show the results obtained for an isothermal junction at $T = 300 \text{ K}$, whereas the dashed lines show the results obtained for a junction with $j_q(x) = 0$ and $T(-L_1) = 300 \text{ K}$.

Eq. (4.76) and we find

$$\begin{aligned} \Delta T_s = & \frac{S_{sF}(1 - P_{\sigma F}^2)}{2\mathcal{L}} R_F (\langle P_\sigma \rangle_R - P_{\sigma F}) j \\ & + \frac{S_{sc}(1 - P_\Sigma^2)}{2\mathcal{L}} [R_F P_{\sigma F} - (R_F + R_N) \langle P_\sigma \rangle_R] j. \end{aligned} \quad (4.85)$$

In Fig. 4.12, we display the profiles of the spin accumulation [Fig. 4.12 (a)] and the spin current [Fig. 4.12 (b)] in $\text{Ni}_{81}\text{Fe}_{19}/\text{Cu}$ junctions ($L_F = L_N = 1 \mu\text{m}$, and $R_c = 1 \times 10^{-16} \Omega\text{m}^2$) across which a current $j = 10^{11} \text{ A/m}^2$ is driven. As can be seen in Fig. 4.12, the agreement between the solutions of an isothermal junction at $T = 300 \text{ K}$ and those of a junction where $j_q(x) = 0$ and $T(-L_F) = 300 \text{ K}$ is very good, that is, for $S_\lambda \ll \sqrt{\mathcal{L}}$ the behavior of the spin accumulation and current is relatively insensitive in these cases.

Having studied the spin-dependent Peltier effect in situations where the spin current is driven by an accompanying charge current, we now turn to a different scenario

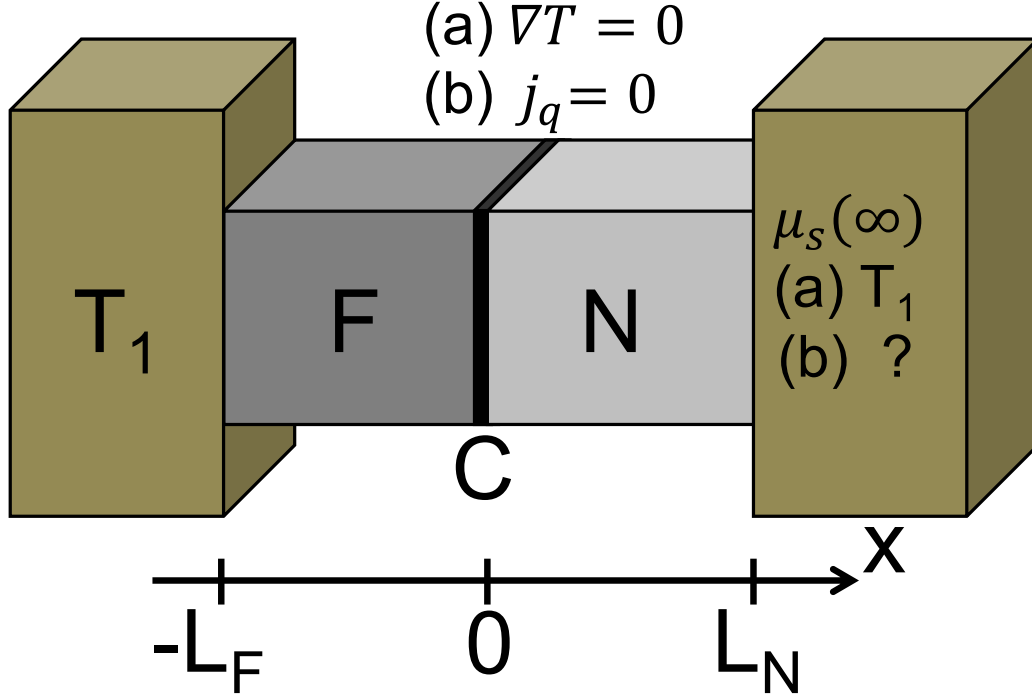


Figure 4.13.: A schematic illustration of a F/N junction in the Silsbee-Johnson spin-charge coupling setup, where (a) refers to an isothermal junction and (b) to the situation where $j_q(x) = 0$. The fact that in (b) the temperature at one end of the junction is not given as an external boundary condition, but has to be calculated from the model is implied by “?”.

in which we are dealing with a pure spin current ($j = 0$) and there, consequently, is no contribution from the conventional Peltier effect. First, we study heating or cooling effects at the interface of a F/N junction in the Silsbee-Johnson spin-charge coupling setup [108, 151], that is, we investigate the heat generated at the F/N interface while keeping the temperature constant across the entire structure, $\nabla T = 0$ [see Fig. 4.13 (a)]. The inverse process of spin injection, the Silsbee-Johnson spin-charge coupling, describes the generation of an electromotive force across the junction due to the presence of nonequilibrium spin in the proximity of the ferromagnet for $j = 0$. This nonequilibrium spin in the N region generates a spin current, which then drives the spin-dependent Peltier effect. For $\nabla T = 0$ and the boundary conditions $\mu_s(-\infty) = 0$ and $\mu_s(\infty) \neq 0$ (modeling the spin accumulation in the N region) the standard model of electrical spin injection yields

$$j_s(0) = \frac{\mu_s(\infty)}{R_F + R_C + R_N} \quad (4.86)$$

for the spin current at the interface [9, 101]. Equations (4.77) and (4.78), which apply to any case of $\nabla T = 0$, show that the heat current vanishes in the N region

and the rate of heat flowing to or away from the interface is given by

$$\Gamma_q^{\text{tot}} = \Gamma_q^s = \frac{TS_{\text{SF}}}{2} \frac{\mu_s(\infty)}{R_{\text{F}} + R_{\text{c}} + R_{\text{N}}}. \quad (4.87)$$

Finally, we look at the Silsbee-Johnson spin-charge coupling setup, but instead of keeping the junction at a constant temperature, we impose the condition $j_q(x) = 0$ while keeping one end at a fixed temperature and calculate the temperature drop across the junction [see Fig. 4.13 (b)]. By applying the additional boundary conditions $\lim_{x \rightarrow -\infty} \mu_s(x) = 0$ and requiring the currents to be continuous at the interface, we can use Eqs. (4.82)-(4.84) with $j = 0$. Thus, $\Delta T_{\text{ch}} = 0$ and the temperature drop across the junction is entirely due to the spin current and spin accumulation, $\Delta T = \Delta T_s$. We find that the spin current at the interface is given by Eq. (4.86) for $S_{\lambda\text{F/N/c}} \ll \sqrt{\mathcal{L}}$ and thus the temperature drop across the junction is given by

$$\Delta T = \frac{\langle S_s(1 - P_\sigma^2) \rangle_R}{2\mathcal{L}} \mu_s(\infty) = -\frac{\kappa}{\mathcal{L}\sigma_{\text{N}}} \mu_s(\infty), \quad (4.88)$$

where κ is the thermal spin-injection efficiency of the F/N junction as defined in Eq. (4.59). Equation (4.88) is the thermal analog of the Silsbee-Johnson spin-charge coupling. The sign of the temperature drop changes when changing the spin accumulation $\mu_s(\infty)$ from parallel to antiparallel to κ .

4.5. F/N/F junctions

4.5.1. F/N/F junctions placed in thermal gradients

The procedure that we used in the previous section to describe spin injection in a F/N junction can also be applied to more complex structures. Here, we will discuss spin injection in a F/N/F junction consisting of two ferromagnets F_1 and F_2 (denoted by the additional subscripts 1 and 2) of lengths L_1 and L_2 and a nonmagnetic conductor N (denoted by the additional subscript N) of length L_{N} between the ferromagnets. By adjusting the orientations of the magnetization in each ferromagnet independently, the junction can be either in a parallel ($\uparrow\uparrow$) or antiparallel ($\uparrow\downarrow$) configuration, that is, we restrict ourselves to collinear configurations. The interfaces C_1 and C_2 between the ferromagnets and the nonmagnetic material are located at $x = 0$ and $x = L_{\text{N}}$. In Ref. 139 the influence of electric currents on the temperature profile in such structures has been investigated if both ends of the device were held at the same temperature. Here, we consider a different situation: We investigate an open circuit geometry ($j = 0$) in which both ends of the device are coupled to different temperature reservoirs. Holding the opposite ends of the device at different temperatures, T_2 and T_1 , gives rise to temperature gradients across the junction. Figure 4.14 gives a schematic overview of this geometry.

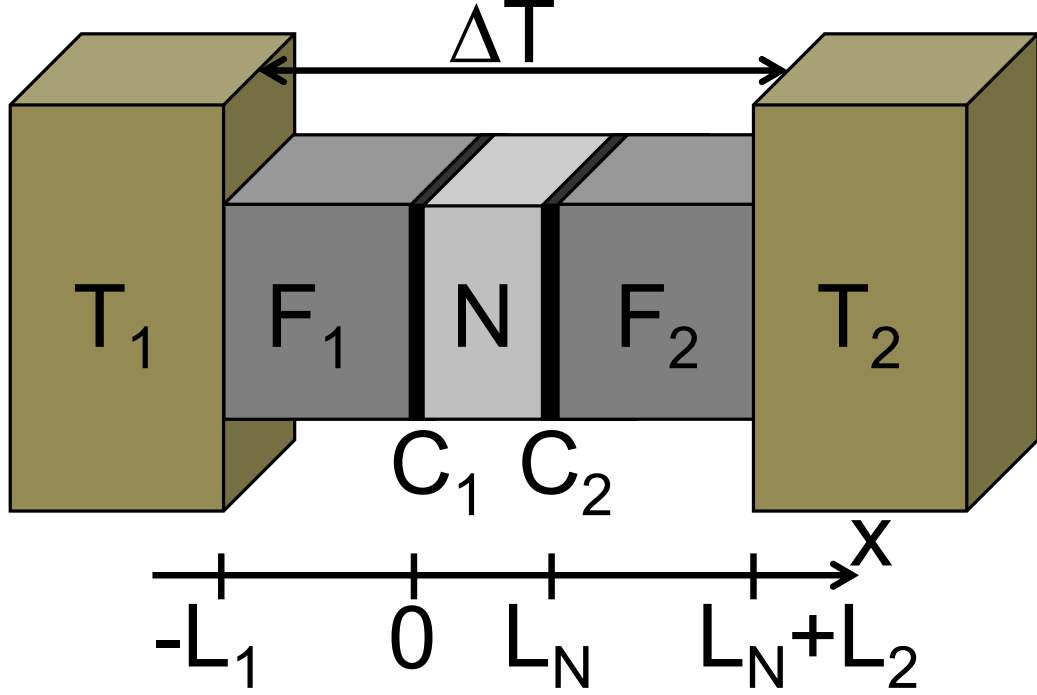


Figure 4.14.: A schematic illustration of a F/N/F junction placed in a thermal gradient.

The chemical potential, the spin accumulation, and the spin current are calculated as in the previous section: Assuming uniform temperature gradients ∇T_1 , ∇T_2 , and ∇T_N , we use the simplified spin-diffusion equation (4.34) and fix the integration constants by the boundary conditions $T(-L_1) = T_1$, $T(L_N + L_2) = T_2$, and $j_s(-L_1) = j_s(L_N + L_2) = 0$. Each of the contact regions C_1 and C_2 is characterized by Eqs. (4.43)-(4.45) and we require that the currents are continuous at each interface. This allows us to obtain the profiles of the chemical potential, the spin accumulation, and the spin current.

As in the case of the F/N junction, spin is either injected or extracted at the interfaces between the ferromagnets and the nonmagnetic material. We investigate the spin-injection efficiencies, $\kappa_1 = j_s(0)/\nabla T_N$ and $\kappa_2 = j_s(L_N)/\nabla T_N$, at the contacts C_1 and C_2 . In general, the expressions for κ_1 and κ_2 are quite unwieldy, but can be simplified somewhat if we assume the case of $L_1 \gg \lambda_{s1}$ and $L_2 \gg \lambda_{s2}$:

$$\kappa_i = \kappa_i^0 R_{\text{FN}}^i \frac{R_N \coth(L_N/\lambda_{sN}) + R_{cj} + R_j}{D_0} + \kappa_j^0 R_{\text{FN}}^j \frac{R_N}{D_0 \sinh(L_N/\lambda_{sN})} \quad (4.89)$$

with $i, j = 1, 2$ and $i \neq j$, the thermal spin-injection efficiencies of the individual F/N junctions,

$$\kappa_i^0 = -\frac{\sigma_N}{2} \frac{S_{sci} R_{ci} (1 - P_{\Sigma ci}^2) + S_{si} R_i (1 - P_{\sigma i}^2)}{R_i + R_{ci} + R_N}, \quad (4.90)$$

as defined in Eq. (4.59), their effective resistances,

$$R_{\text{FN}}^i = R_i + R_{c_i} + R_N, \quad (4.91)$$

and

$$D_0 = R_N^2 + (R_{c1} + R_1)(R_{c2} + R_2) + \coth(L_N/\lambda_{sN}) (R_1 + R_{c1} + R_{c2} + R_2) R_N. \quad (4.92)$$

Comparing the thermal and electrical [101] spin-injection efficiencies of the F/N/F junction, we find that the structure of Eq. (4.89) is similar to the structure of the electrical spin-injection efficiency. Here, the temperature gradient in the N region reads as

$$\nabla T_N = \frac{\Delta T}{\sigma_N \mathcal{R}_{\text{FNF}}}, \quad (4.93)$$

where

$$\mathcal{R}_{\text{FNF}} = \frac{L_1}{\sigma_1} + \frac{1}{\Sigma_{c1}} + \frac{L_N}{\sigma_N} + \frac{1}{\Sigma_{c2}} + \frac{L_2}{\sigma_2}. \quad (4.94)$$

For a given temperature gradient, Eq. (4.89) can be used to determine whether there is spin injection [$j_s(0) < 0$ or $j_s(L_N) > 0$] or extraction [$j_s(0) > 0$ or $j_s(L_N) < 0$] at the interface C_i . The profiles of the spin current and the spin accumulation in the N region ($0 < x < L_N$) are

$$\frac{j_s(x)}{\nabla T_N} = \frac{\kappa_2 \sinh(x/\lambda_{sN}) - \kappa_1 \sinh[(x - L_N)/\lambda_{sN}]}{\sinh(L_N/\lambda_{sN})} \quad (4.95)$$

and

$$\frac{\mu_s(x)}{R_N \nabla T_N} = \frac{\kappa_2 \cosh(x/\lambda_{sN}) - \kappa_1 \cosh[(x - L_N)/\lambda_{sN}]}{\sinh(L_N/\lambda_{sN})}. \quad (4.96)$$

If $L_N \gg \lambda_{sN}$, Eq. (4.89) reduces to Eq. (4.59), that is, the spin-injection efficiency of a simple F/N junction.

In analogy to the procedure employed in Sec. 4.4, we can calculate the drop of the chemical potential across the F/N/F junction

$$\Delta(\eta/e + \mu) = [\eta(T_2) - \eta(T_1)]/e + \mu(L_N + L_2) - \mu(-L_1) \quad (4.97)$$

and relate this drop to the Seebeck coefficient S of the entire device

$$\Delta(\eta/e + \mu) \equiv S \Delta T \equiv (S_0 + \delta S) \Delta T, \quad (4.98)$$

which we split into the equilibrium contribution S_0 and a nonequilibrium contribution δS due to spin accumulation. By investigating the chemical potential drops in the different regions and at the contacts we obtain the equilibrium and nonequilibrium Seebeck coefficients

$$S_0 = \frac{1}{2\mathcal{R}_{\text{FNF}}} \left[\frac{(S_1 + S_{s1}P_{\sigma1})L_1}{\sigma_1} + \frac{S_{c1} + S_{sc1}P_{\Sigma1}}{\Sigma_{c1}} + \frac{S_N L_N}{\sigma_N} + \frac{S_{c2} + S_{sc2}P_{\Sigma2}}{\Sigma_{c2}} + \frac{(S_2 + S_{s2}P_{\sigma2})L_2}{\sigma_2} \right] \quad (4.99)$$

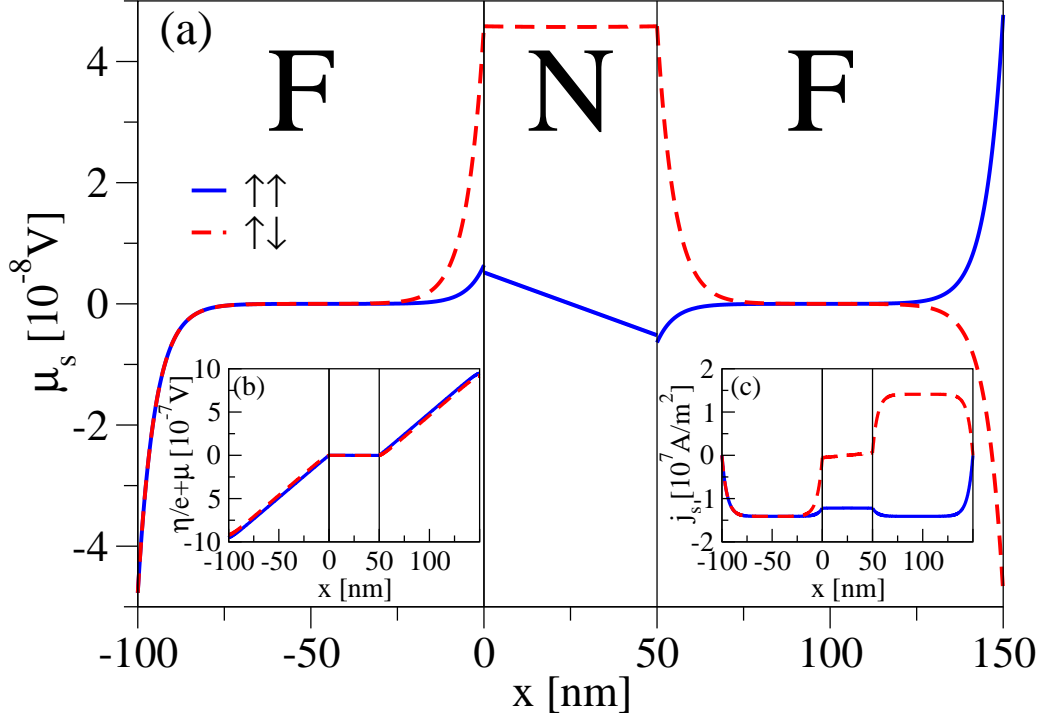


Figure 4.15.: Profiles of the (a) spin potential, the (b) total chemical potential, and the (c) spin current for a $\text{Ni}_{81}\text{Fe}_{19}/\text{Cu}/\text{Ni}_{81}\text{Fe}_{19}$ junction at $T = 300$ K with $L_1 = L_2 = 100$ nm, $L_N = 50$ nm, and $\Delta T = -100$ mK. The solid lines show the profiles for the parallel configuration, the dashed lines for the antiparallel configuration.

and

$$\begin{aligned} \delta S = \frac{1}{\mathcal{R}_{\text{FNF}}} & \left\{ P_{\Sigma 1} \left[\frac{R_1 \kappa_1}{\sigma_N} + \frac{S_{s1} \lambda_{s1}}{2\sigma_1} - \lambda_{sN} \frac{\kappa_2 - \kappa_1 \cosh(L_N/\lambda_{sN})}{\sinh(L_N/\lambda_{sN})} \right] \right. \\ & + P_{\Sigma 2} \left[\frac{R_2 \kappa_2}{\sigma_N} + \frac{S_{s2} \lambda_{s2}}{2\sigma_2} - \lambda_{sN} \frac{\kappa_1 - \kappa_2 \cosh(L_N/\lambda_{sN})}{\sinh(L_N/\lambda_{sN})} \right] \\ & \left. - P_{\sigma 1} \left(\frac{\kappa_1 R_1}{\sigma_N} + \frac{S_{s1} \lambda_{s1}}{\sigma_1} \right) - P_{\sigma 2} \left(\frac{\kappa_2 R_2}{\sigma_N} + \frac{S_{s2} \lambda_{s2}}{\sigma_2} \right) \right\}. \end{aligned} \quad (4.100)$$

Once more, Eq. (4.100) has been derived in the limit of $L_1 \gg \lambda_{s1}$ and $L_2 \gg \lambda_{s2}$, which usually applies to most devices.

Figure 4.15 shows the profiles for a symmetric F/N/F junction consisting of $\text{Ni}_{81}\text{Fe}_{19}$ as ferromagnets and Cu as the nonmagnetic material (for the corresponding parameters see Secs. 4.3 and 4.4) for $T = (T_1 + T_2)/2 = 300$ K and $\Delta T = T_2 - T_1 = -100$ mK. Here, the lengths of the individual constituents are chosen to be $L_1 = L_2 = 100$ nm and $L_N = 50$ nm. The contact parameters are $R_{c1} = R_{c2} = 1 \times 10^{-16} \Omega\text{m}^2$, $S_{c1} = S_{c2} = -1.0 \times 10^{-6} \text{ V/K}$, and $P_{\Sigma 1} = \pm P_{\Sigma 2} = 0.5$ and $S_{sc1} = \pm S_{sc2} = 0.5 S_{c1}$

depending on whether the parallel (+) or antiparallel (−) configuration is investigated. As shown in Figs. 4.15 (a) and (c), spin is injected into the N region from both F regions in the antiparallel configuration. If the F/N/F junction is in the parallel configuration, spin is injected into the N region from one F region, while at the opposite interface, spin is extracted from the N region. Changing the sign of ΔT would lead to spin extraction from the N region in the antiparallel configuration, whereas spin would still be injected at one interface and extracted at the other interface. In Fig. 4.15 (b), one can observe a drop of the total chemical potential across the F/N/F junction for both, the parallel and antiparallel configurations. If an asymmetric F/N/F junction (for example, by choosing different lengths L_1 and L_2 or different materials for F_1 and F_2) is considered, the qualitative properties of Fig. 4.15 will remain the same, although the graphs will be distorted compared to the symmetric case.

Next, we look at the difference between the drops of the chemical potential [given by Eq. (4.97)] in the parallel and antiparallel configurations (denoted by the superscripts $i = \uparrow\uparrow, \uparrow\downarrow$ in the following), as a quantitative measure of the spin accumulation in the N region (thermal analog of the giant magnetoresistance). If one analyzes the temperature profile $T(x)$ and the local equilibrium chemical potential $\eta[T(x)]$, one finds that within our model they are the same for the parallel and antiparallel configurations (in the limit $S_{\lambda j} \ll \sqrt{\mathcal{L}}$). Hence, the difference between the drops of the chemical potential is just the drop of the quasichemical potentials, that is,

$$\Delta(\eta/e + \mu)^{\uparrow\uparrow} - \Delta(\eta/e + \mu)^{\uparrow\downarrow} = \Delta\mu^{\uparrow\uparrow} - \Delta\mu^{\uparrow\downarrow}, \quad (4.101)$$

where $\Delta\mu^i = \mu^i(L_N + L_2) - \mu^i(-L_1)$. Moreover, the equilibrium Seebeck coefficients given by Eq. (4.99) are the same for both configurations and consequently

$$\Delta\mu^{\uparrow\uparrow} - \Delta\mu^{\uparrow\downarrow} = (\delta S^{\uparrow\uparrow} - \delta S^{\uparrow\downarrow}) \Delta T, \quad (4.102)$$

which, in the limit of $L_1 \gg \lambda_{s1}$ and $L_2 \gg \lambda_{s2}$, yields

$$\begin{aligned} \Delta\mu^{\uparrow\uparrow} - \Delta\mu^{\uparrow\downarrow} = & \frac{\lambda_{sN} \nabla T_N}{D_0 \sinh(L_N/\lambda_{sN})} \left[\left(\frac{S_{s1} \lambda_{s1}}{\sigma_1} + \frac{S_{sc1}}{\Sigma_{c1}} \right) (R_2 P_2 + R_{c2} P_{\Sigma 2}) \right. \\ & \left. + \left(\frac{S_{s2} \lambda_{s2}}{\sigma_2} + \frac{S_{sc2}}{\Sigma_{c2}} \right) (R_1 P_1 + R_{c1} P_{\Sigma 1}) \right], \end{aligned} \quad (4.103)$$

if Eq. (4.100) is inserted for each of the nonequilibrium Seebeck coefficients. In Eq. (4.103) as well as in the following, we choose to express the system parameters in terms of the parallel configuration (for example, $P_2 = P_2^{\uparrow\uparrow}$ etc.). As mentioned before, in our approximation the temperature gradient in the N region, given by Eq. (4.93), does not depend on whether the system is in its parallel or antiparallel configuration.

4. Theory of thermal spin-charge coupling in electronic systems

The charge neutrality condition (4.17) enables us to relate $\Delta\mu^i$ to the voltage drop measured across the junction, $\Delta\varphi^i = \varphi^i(L_N + L_2) - \varphi^i(-L_1)$. Using this, the difference between the voltage drops in both configurations can be written as

$$\Delta\varphi^{\uparrow\uparrow} - \Delta\varphi^{\uparrow\downarrow} = \frac{g_{s1}}{g_1} \left(\mu_{sL}^{\uparrow\uparrow} - \mu_{sL}^{\uparrow\downarrow} \right) - \frac{g_{s2}}{g_2} \left(\mu_{sR}^{\uparrow\uparrow} + \mu_{sR}^{\uparrow\downarrow} \right) - (\Delta\mu^{\uparrow\uparrow} - \Delta\mu^{\uparrow\downarrow}), \quad (4.104)$$

where the shorthand notations $\mu_{sL}^i = \mu_s^i(-L_1)$ and $\mu_{sR}^i = \mu_s^i(L_N + L_2)$ have been introduced. For $L_1 \gg \lambda_{s1}$ and $L_2 \gg \lambda_{s2}$, the contributions to Eq. (4.104) originating from the spin accumulation at $x = -L_1$ and $x = L_N + L_2$, $\mu_{sL}^{\uparrow\uparrow} - \mu_{sL}^{\uparrow\downarrow}$ and $\mu_{sR}^{\uparrow\uparrow} + \mu_{sR}^{\uparrow\downarrow}$, are small compared to $\Delta\mu^{\uparrow\uparrow} - \Delta\mu^{\uparrow\downarrow}$ and consequently

$$\Delta\varphi^{\uparrow\uparrow} - \Delta\varphi^{\uparrow\downarrow} \approx -(\Delta\mu^{\uparrow\uparrow} - \Delta\mu^{\uparrow\downarrow}). \quad (4.105)$$

Thus, one can also measure the difference between the quasichemical potential drops electrostatically, namely as the difference between the voltage drops across the F/N/F junction.

Figure 4.16 shows the dependence of $\Delta\mu^{\uparrow\uparrow} - \Delta\mu^{\uparrow\downarrow}$ on the length of the N region, L_N , for a symmetric $\text{Ni}_{81}\text{Fe}_{19}/\text{Cu}/\text{Ni}_{81}\text{Fe}_{19}$ junction similar to the one considered above (apart from L_N , R_{c1} , and R_{c2} the parameters are the same as in Fig. 4.15) for the contact resistances $R_{c1} = R_{c2} = 1 \times 10^{-16} \Omega\text{m}^2$ and $R_{c1} = R_{c2} = 1 \times 10^{-14} \Omega\text{m}^2$. With increasing length of the N region, the amplitude of the voltage difference decreases until, for very large N regions with $L_N \gg \lambda_{sN}$, there is no difference between the voltage drops in the parallel and antiparallel configurations and $\Delta\mu^{\uparrow\uparrow} - \Delta\mu^{\uparrow\downarrow} \rightarrow 0$. If L_N is comparable or even smaller than the spin-diffusion length ($\lambda_{sN} \approx 350$ nm in Cu), the voltage drops across the F/N/F junction are different for the different configurations with $\Delta\mu^{\uparrow\uparrow} - \Delta\mu^{\uparrow\downarrow}$ given by Eq. (4.103).

4.5.2. Peltier effects in F/N/F junctions

The section on F/N/F junctions is concluded by a brief discussion of Peltier effects in such structures in the limit of $S_{\lambda_j} \ll \sqrt{\mathcal{L}}$ and $L_{1/2} \gg \lambda_{s1/2}$.

Figure 4.17 (a) summarizes the first system considered: A charge current j is driven across an isothermal F/N/F junction and there is heating or cooling of the interfaces. Similarly to Sec. 4.4.3, the electrical spin-injection efficiencies at the interfaces $P_{j1} = j_s(0)/j$ and $P_{j2} = j_s(L_N)/j$ are given by the standard model of electrical spin injection and, as described in detail in Ref. 101, read as

$$P_{jk} = P_{jk}^0 R_{\text{FN}}^k \frac{R_N \coth(L_N/\lambda_{sN}) + R_{cl} + R_l}{D_0} + P_{jl}^0 R_{\text{FN}}^l \frac{R_N}{D_0 \sinh(L_N/\lambda_{sN})}, \quad (4.106)$$

where D_0 is given by Eq. (4.92) and $k, l = 1, 2$ and $k \neq l$. The effective resistances of the individual F/N junctions R_{FN}^k are given by Eq. (4.91) and their electrical

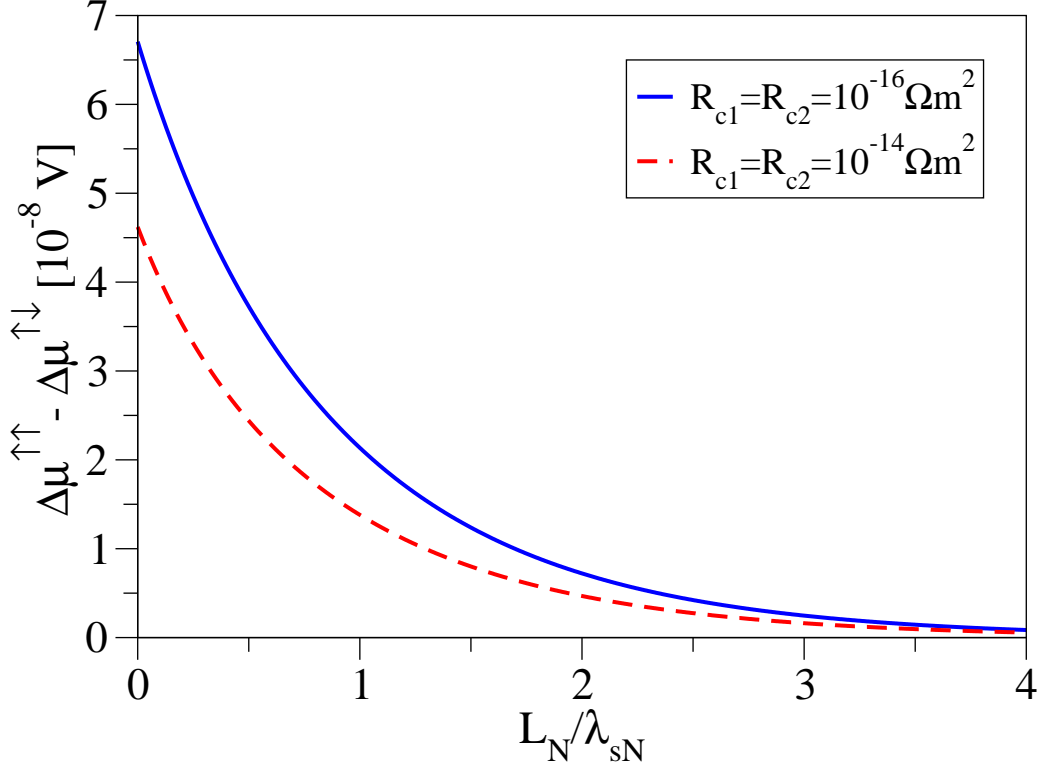


Figure 4.16.: Difference between the chemical potential drops of the parallel and antiparallel configurations, $\Delta\mu^{\uparrow\uparrow} - \Delta\mu^{\uparrow\downarrow}$, as a function of the length of the N region, L_N , for a $\text{Ni}_{81}\text{Fe}_{19}/\text{Cu}/\text{Ni}_{81}\text{Fe}_{19}$ junction at $T = 300$ K with $L_1 = L_2 = 100$ nm and $\Delta T = -100$ mK.

spin-injection efficiencies by

$$P_{jk}^0 = \frac{P_{\Sigma k} R_{ck} + P_{\sigma k} R_k}{R_k + R_{ck} + R_N}. \quad (4.107)$$

As noted above, the electrical spin-injection efficiencies (4.106) of a F/N/F junction are composed of the electrical spin-injection efficiencies of the individual F/N junctions in the same way the thermal spin-injection efficiencies [Eq. (4.89)] are composed of the thermal spin-injection efficiencies of the individual F/N junctions.

Consequently, the rates of heat production or dissipation at contacts C_1 and C_2 read as

$$\Gamma_{q1}^{\text{tot}} = j_q(0^-) - j_q(0^+) = \Gamma_{q1} + \Gamma_{q1}^s, \quad (4.108)$$

$$\Gamma_{q2}^{\text{tot}} = j_q(L_N^-) - j_q(L_N^+) = \Gamma_{q2} + \Gamma_{q2}^s \quad (4.109)$$

and consist of contributions from the conventional Peltier effect

$$\Gamma_{q1} = \frac{T(S_1 - S_N)j}{2}, \quad (4.110)$$

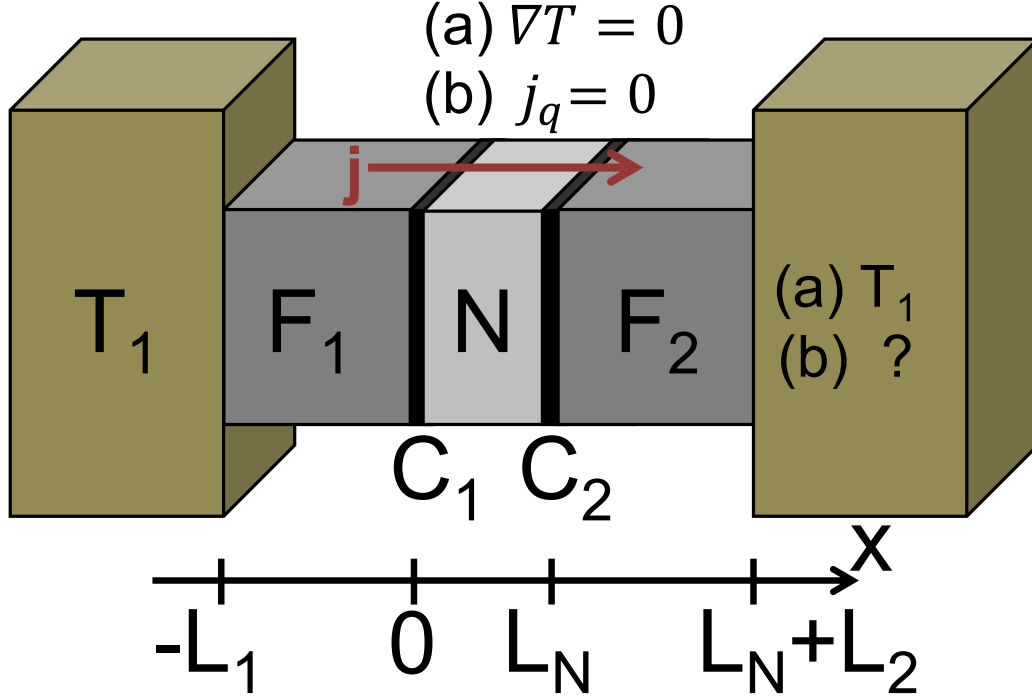


Figure 4.17.: A schematic illustration of a F/N/F junction in the electrical spin-injection setup, where (a) refers to an isothermal junction and (b) to the situation where $j_q(x) = 0$. The fact that in (b) the temperature at one end of the junction is not given as an external boundary condition, but has to be calculated from the model is implied by “?”.

$$\Gamma_{q2} = \frac{T(S_N - S_2)j}{2}, \quad (4.111)$$

as well as contributions from the spin-dependent Peltier effect

$$\Gamma_{q1}^s = \frac{TS_{s1}P_{j1}j}{2}, \quad (4.112)$$

$$\Gamma_{q2}^s = -\frac{TS_{s2}P_{j2}j}{2}. \quad (4.113)$$

Figure 4.18 illustrates this situation for an isothermal $\text{Ni}_{81}\text{Fe}_{19}/\text{Cu}/\text{Ni}_{81}\text{Fe}_{19}$ junction (in parallel and antiparallel configurations) at $T = 300$ K with $L_1 = L_2 = 100$ nm, $L_N = 50$ nm, $R_{c1} = R_{c2} = 1 \times 10^{-16} \Omega\text{m}^2$, $S_{c1} = S_{c2} = -1.0 \times 10^{-6}$ V/K, $P_{\Sigma 1} = \pm P_{\Sigma 2} = 0.5$, $S_{sc1} = \pm S_{sc2} = 0.5S_{c1}$, and $j = 10^7$ A/m². The profiles of the heat current in Fig. 4.18 show that, for the parameters chosen, there is cooling at C_1 ($x = 0$) as heat flows away from it, while heat flows to C_2 and leads to heating in the region around the C_2 ($x = L_N$). The widths of those regions of heating or cooling are given by the individual spin-diffusion lengths.

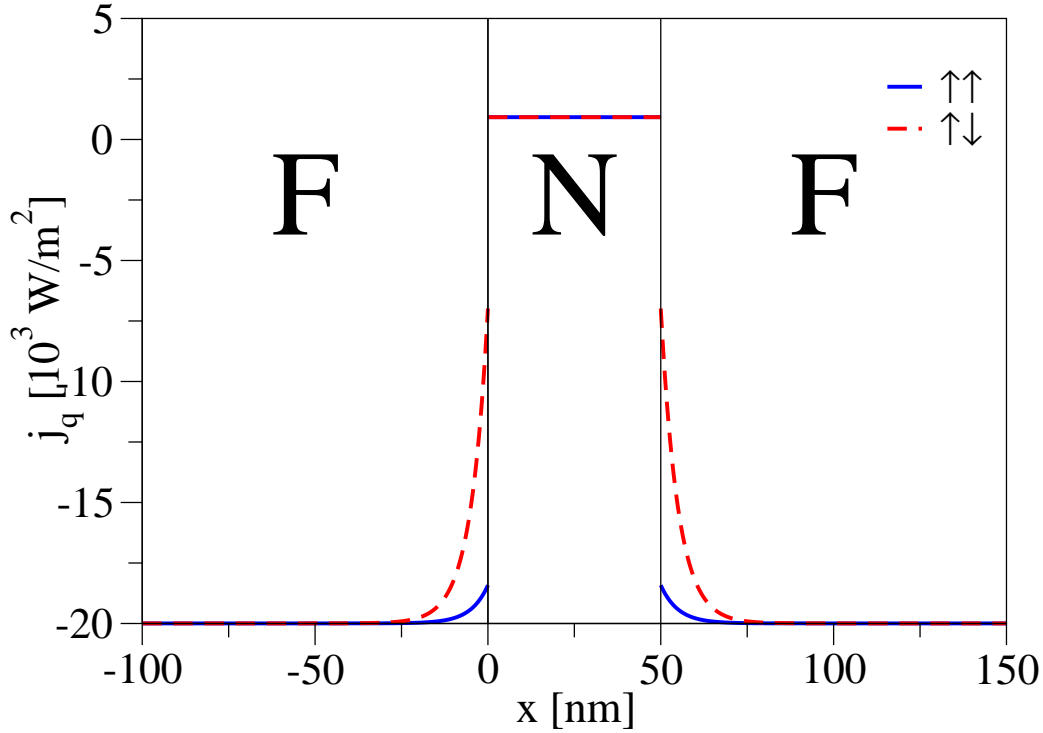


Figure 4.18.: Profiles of the heat current for an isothermal $\text{Ni}_{81}\text{Fe}_{19}/\text{Cu}/\text{Ni}_{81}\text{Fe}_{19}$ junction at $T = 300$ K with $L_1 = L_2 = 100$ nm, $L_N = 50$ nm, and $j = 10^7$ A/m². The solid line shows the profile for the parallel configuration, the dashed line for the antiparallel configuration.

The second system considered is a F/N/F junction where $j_q(x) = 0$ and across which an electric current j is driven and one end of which is anchored at a fixed temperature [see Fig. 4.17 (b)]. Requiring the charge, spin, and heat currents given by Eqs. (4.43)-(4.45) to be continuous and imposing the additional boundary conditions $\lim_{x \rightarrow \pm\infty} \mu_s(x) = 0$, we find that the temperature drop across the junction $\Delta T = \Delta T_{\text{ch}} + \Delta T_s$ is composed of a drop due to the conventional Peltier effect

$$\Delta T_{\text{ch}} = \left[\frac{(S_1 + S_{s1}P_{\sigma 1}) L_1}{2\mathcal{L}\sigma_1} + \frac{S_{c1} + S_{sc1}P_{\Sigma 1}}{2\mathcal{L}\Sigma_{c1}} + \frac{S_N L_N}{2\mathcal{L}\sigma_N} + \frac{S_{c2} + S_{sc2}P_{\Sigma 2}}{2\mathcal{L}\Sigma_{c2}} + \frac{(S_2 + S_{s2}P_{\sigma 2}) L_2}{2\mathcal{L}\sigma_2} \right] j, \quad (4.114)$$

4. Theory of thermal spin-charge coupling in electronic systems

and a contribution due to the spin accumulation in the region around the interfaces

$$\begin{aligned}\Delta T_s = & \frac{S_{s1}(1 - P_{\sigma 1}^2)}{2\mathcal{L}}\mu_s(0^-) - \frac{S_{s2}(1 - P_{\sigma 2}^2)}{2\mathcal{L}}\mu_s(L_N^+) \\ & + \frac{S_{sc1}(1 - P_{\Sigma 1}^2)}{2\mathcal{L}}[\mu_s(0^+) - \mu_s(0^-)] \\ & + \frac{S_{sc2}(1 - P_{\Sigma 2}^2)}{2\mathcal{L}}[\mu_s(L_N^+) - \mu_s(L_N^-)].\end{aligned}\quad (4.115)$$

Here, we are mainly interested in the difference between those temperature drops in configurations of parallel and antiparallel magnetizations of the ferromagnets (denoted by the superscripts $i = \uparrow\uparrow, \uparrow\downarrow$ as in Sec. 4.5.1). With the temperature drop due to the conventional Peltier effect being the same for both configurations, this difference is exclusively due to the spin accumulation, that is, $\Delta T^{\uparrow\uparrow} - \Delta T^{\uparrow\downarrow} = \Delta T_s^{\uparrow\uparrow} - \Delta T_s^{\uparrow\downarrow}$, which can be calculated as

$$\begin{aligned}\Delta T^{\uparrow\uparrow} - \Delta T^{\uparrow\downarrow} = & \frac{R_N j}{\mathcal{L} D_0 \sinh(L_N/\lambda_{sN})} \left[\left(\frac{S_{s1}\lambda_{s1}}{\sigma_1} + \frac{S_{sc1}}{\Sigma_{c1}} \right) (R_2 P_2 + R_{c2} P_{\Sigma 2}) \right. \\ & \left. + \left(\frac{S_{s2}\lambda_{s2}}{\sigma_2} + \frac{S_{sc2}}{\Sigma_{c2}} \right) (R_1 P_1 + R_{c1} P_{\Sigma 1}) \right],\end{aligned}\quad (4.116)$$

where we have expressed the system parameters in terms of the parallel configuration (see Sec. 4.5.1).

For illustration, the temperature profiles of a $\text{Ni}_{81}\text{Fe}_{19}/\text{Cu}/\text{Ni}_{81}\text{Fe}_{19}$ junction at $T = 300$ K with $j_q(x) = 0$, $L_1 = L_2 = 100$ nm, $L_N = 50$ nm, $R_{c1} = R_{c2} = 1 \times 10^{-16} \Omega\text{m}^2$, $S_{c1} = S_{c2} = -1.0 \times 10^{-6}$ V/K, $P_{\Sigma 1} = \pm P_{\Sigma 2} = 0.5$, $S_{sc1} = \pm S_{sc2} = 0.5 S_{c1}$, and $j = 10^{11}$ A/m² are shown in Fig. 4.19 (a) for both, parallel and antiparallel magnetizations in the ferromagnets. While the main (linear) contribution to the temperature drop originates from the charge Peltier effect and is the same for both configurations, the spin accumulation near the interfaces is different for each configuration and accounts for different temperature profiles. Figure 4.19 (b), which depicts the difference between the temperature profiles of the parallel and antiparallel configurations, also shows that this difference in the temperature profiles arises in the F regions near the interfaces and within the spin-diffusion lengths. Outside these regions, the temperature difference remains constant.

4.6. Conclusion

We have generalized the standard model of spin injection as explained in Refs. 8, 9, 101 to describe the coupling between charge, spin, and heat transport in metals. The formalism has then been used to describe the electronic contribution to the spin(-dependent) Seebeck effect in such materials, where we found that only at the boundaries of the ferromagnet is there significant electronic spin accumulation, which, however, decays within the spin-diffusion length and can therefore not be responsible for

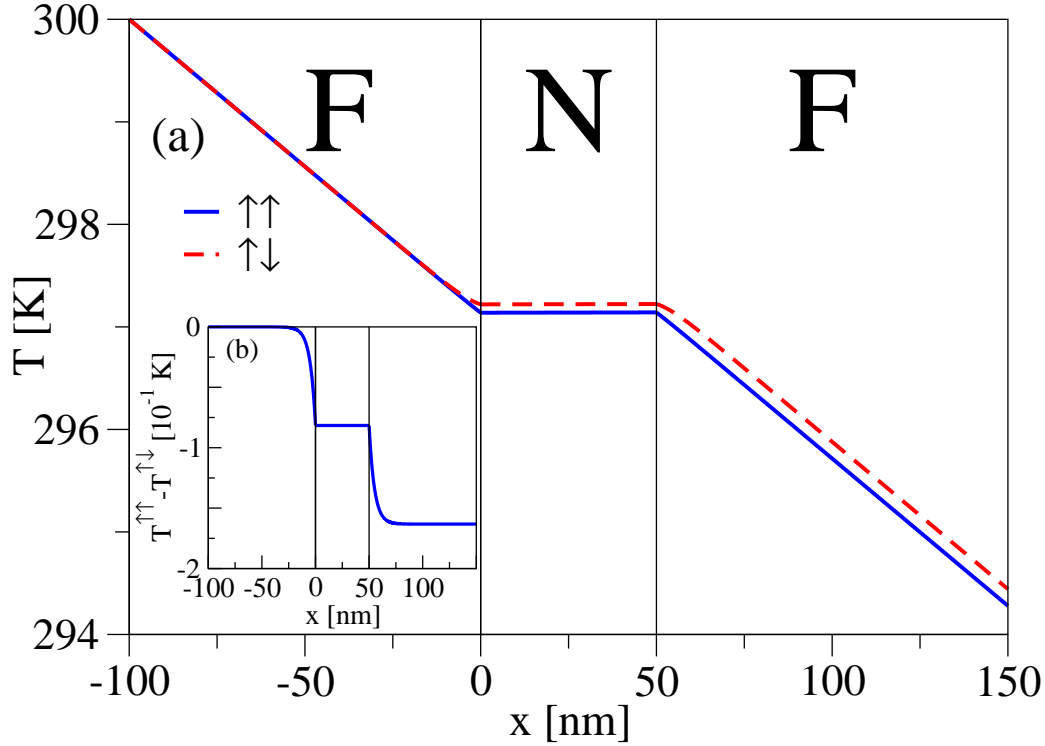


Figure 4.19.: Temperature profile (a) of a $\text{Ni}_{81}\text{Fe}_{19}/\text{Cu}/\text{Ni}_{81}\text{Fe}_{19}$ junction with $j_q(x) = 0$, $T_1 = 300$ K, $L_1 = L_2 = 100$ nm, $L_N = 50$ nm, and $j = 10^{11}$ A/m². The solid line shows the profile for the parallel configuration, the dashed line for the antiparallel configuration. The profile of the temperature difference between the parallel and antiparallel configurations is shown in the inset (b).

the linear inverse spin Hall voltage measured by Uchida *et al.* [123]. Furthermore, we have analyzed F/N and F/N/F junctions. For F/N junctions, we have shown that a temperature difference between both ends of the junction generates pure spin currents, which can be used to extract or inject spin at the interface between the F and N regions. We have also derived a formula to measure the efficiency of the spin injection (extraction). In the case of a F/N/F junction, a temperature difference can also be used to extract or inject spin into the N region if the junction is in a antiparallel configuration. Moreover, a formula has been derived to calculate the difference between the voltage drops across the junction in the parallel and antiparallel configurations. Finally, we have investigated the Peltier and spin-dependent Peltier effects in F/N and F/N/F junctions and derived analytical formulas to describe their respective contributions to the heating or cooling in these systems.

5. Outlook

In this thesis, we have dealt with several different topics. The main results of each topic have already been summarized at the end of the respective chapters, so we restrict ourselves to presenting a brief outlook on how the different topics we have worked on could be extended.

The first part of this thesis has been devoted to HgTe/CdTe-based quantum wells. Using analytical formulas as well as a finite-difference scheme, we have studied the magnetic field dependence of the energy spectra and magnetic edge states of those structures in the presence of perpendicular magnetic fields and hard walls for the band-structure parameters corresponding to the normal ($d < d_c$) and inverted ($d > d_c$) regimes. We have found that up to a certain value of the magnetic field ($B_c \approx 7.4$ T) counterpropagating, spin-polarized states can still be observed in the inverted regime, although these states are then no longer protected by time-reversal symmetry. Furthermore, the bulk magnetization in HgTe quantum wells and their characteristic de Haas-van Alphen oscillations have been studied, as well as the bulk magneto-optical conductivity in such structures.

An obvious next step to extend the results for the magnetization and magneto-optical conductivity (summarized in Sec. 2.5) would be to investigate how the results change when edge states are taken into account. To do so, one can employ either the analytical formalism derived in Sec. 2.2.1 or the finite-difference scheme introduced in Sec. 2.2.2 and calculate the spectrum and states in the presence of hard walls, from which one can then calculate the density of states and the dipole matrix elements for semi-infinite or finite systems. This density of states can then be used to compute the grand potential numerically [see Eqs. (2.40) and (2.41)], which in turn allows one to obtain the magnetization. The dipole matrix elements can—in conjunction with the spectrum—be used to calculate the magneto-optical conductivity in the presence of hard walls via Kubo formulas similar to Eqs. (2.67) and (2.68). Besides this, one could also use the analytical formalism from Sec. 2.2.1 to calculate so-called snake orbits, that is, magnetic edge states induced by a nonhomogeneous magnetic field [152]. Moreover, the finite-difference scheme could be employed to study topological p-n junctions [153] or the effect of (magnetic) impurities in HgTe quantum wells numerically.

In the second part of this thesis, we have investigated the effect that optical phonons and SPPs have on the optical conductivity in graphene and have found that those phonons increase the absorption in the region $0 < \hbar\omega < 2\mu$. As mentioned in Sec. 3.4, one way to refine the present model is by including dynamical screening and energy-

5. Outlook

dependent lifetime broadening (arising, for example, from Coulomb scattering or acoustic phonons). Instead of graphene situated on a substrate, one could also use the formalism introduced in Sec. 3.2 to investigate suspended graphene. While there are no SPPs in this case, flexural phonons might, on the other hand, influence the optical properties of graphene in this case. Moreover, one could also generalize the formalism from Sec. 3.2: It might be useful to investigate the optical conductivity, not only for a uniform system, but also at finite momentum \mathbf{q} . At finite momenta, a study of plasmon modes might of course also be worthwhile. Another possible continuation of this work would be to extend the formalism to include finite magnetic fields, that is, to calculate the magneto-optical conductivity in graphene.

Finally, we have formulated a phenomenological model in the spirit of the standard model of electrical spin injection to describe the electronic mechanism coupling charge, spin, and heat transport and employed this model to analyze several different geometries containing ferromagnetic and nonmagnetic regions: F, F/N, and F/N/F junctions which are subject to thermal gradients. Furthermore, we have studied the Peltier and spin-dependent Peltier effects in F/N and F/N/F junctions and presented analytical formulas for the heat evolution at the interfaces of isothermal junctions. We have presented analytical formulas for the spin accumulation and spin current profiles in those junctions that are valid for both tunnel and transparent (as well as intermediate) contacts. For F/N junctions, we have calculated the thermal spin injection efficiency and the spin accumulation induced nonequilibrium thermopower. We have found conditions for countering thermal spin effects in the N region with electrical spin injection. This compensating effect should be particularly useful for distinguishing electronic from other mechanisms of spin injection by thermal gradients. For F/N/F junctions, we have analyzed the differences in the nonequilibrium thermopower (and chemical potentials) for parallel and antiparallel orientations of the F magnetizations, as evidence and a quantitative measure of the spin accumulation in N.

Just like the standard model of electrical spin injection, the phenomenological model introduced in Chap. 4 can be employed to analyze not only the geometries presented in this work, but also more complex, non-local geometries (which are, for example, used to detect spin accumulation in experiments). Furthermore, one could refine the model by including effects like spin-orbit coupling or the interplay of thermal and spin currents with the magnon and spin-phonon drags in the heterostructures investigated above. To study these effects on a microscopic level, one would, however, have to go beyond the phenomenological model and use procedures such as the Boltzmann or Kubo formalisms.

A. Finite-difference method

The basic idea of any method involving finite differences to solve a system of differential equations is to discretize the space a continuous function $f(\mathbf{r})$ is defined on by creating a grid of points \mathbf{r}_l on this space. While functions of \mathbf{r} are simply evaluated on the grid, derivatives have to be replaced by finite-difference schemes. By substituting the derivatives with a finite-difference scheme, the system of differential equations is reduced to a system of algebraic equations which can then be solved numerically.

In general, there are several different finite-difference formulas commonly used to express derivatives. For our numerical calculations, we have used the central-difference scheme, which will be briefly introduced in the following. Here, we restrict ourselves to the case of a one-dimensional function $f(x)$ for convenience.

Consider the Taylor expansion of the function $f(x)$ at the points $x \pm a$,

$$f(x + a) = f(x) + \frac{df(x)}{dx}a + \frac{1}{2} \frac{d^2f(x)}{dx^2}a^2 + \mathcal{O}(a^3) \quad (\text{A.1})$$

and

$$f(x - a) = f(x) - \frac{df(x)}{dx}a + \frac{1}{2} \frac{d^2f(x)}{dx^2}a^2 + \mathcal{O}(a^3). \quad (\text{A.2})$$

By subtracting Eq. (A.2) from Eq. (A.1), keeping only terms up to a^3 , and solving for $df(x)/dx$, we find

$$\frac{df(x)}{dx} = \frac{f(x + a) - f(x - a)}{2a} + \mathcal{O}(a^2). \quad (\text{A.3})$$

Likewise, we can take the sum of Eqs. (A.1) and (A.2), keep only terms up to a^4 , and solve for $d^2f(x)/dx^2$, which reads as

$$\frac{d^2f(x)}{dx^2} = \frac{f(x + a) - 2f(x) + f(x - a)}{a^2} + \mathcal{O}(a^2). \quad (\text{A.4})$$

If a is chosen as the 'lattice constant' of the grid used to describe the function $f(x)$, Eqs. (A.3) and (A.4) enable us to replace the first and second derivatives of $f(x)$ at $x = x_l = al$ by combinations of $f(x_{l+1}) = f(x_l + a)$, $f(x_{l-1}) = f(x_l - a)$, and $f(x_l)$. Therefore, Eqs. (A.3) and (A.4) connect the derivatives at a grid point x_l to the values of the function at x_l itself and at directly adjacent grid points $x_{l\pm 1}$.

In order to improve the convergence of the scheme introduced above, one can also consider points beyond the nearest grid points. If next-nearest grid points $x_{l\pm 2} =$

A. Finite-difference method

$x_l \pm 2a$ are to be considered, in addition to Eqs. (A.1) and (A.2), we also look at the Taylor expansions

$$f(x + 2a) = f(x) + 2\frac{df(x)}{dx}a + 2\frac{d^2f(x)}{dx^2}a^2 + \mathcal{O}(a^3) \quad (\text{A.5})$$

and

$$f(x - 2a) = f(x) - 2\frac{df(x)}{dx}a + 2\frac{d^2f(x)}{dx^2}a^2 + \mathcal{O}(a^3). \quad (\text{A.6})$$

Equations (A.1), (A.2), (A.5), and (A.6) can then be solved for $df(x)/dx$ and $d^2f(x)/dx^2$ and we obtain

$$\frac{df(x)}{dx} = \frac{-f(x + 2a) + 8f(x + a) - 8f(x - a) + f(x - 2a)}{12a} + \mathcal{O}(a^4) \quad (\text{A.7})$$

and

$$\frac{d^2f(x)}{dx^2} = \frac{-f(x + 2a) + 16f(x + a) - 30f(x) + 16f(x - a) - f(x - 2a)}{12a^2} + \mathcal{O}(a^4). \quad (\text{A.8})$$

Now, the derivatives at x_l are calculated by including also the values of the function at the next-nearest grid points $x_{l\pm 2}$.

The scheme introduced above can be generalized easily to higher-dimensional spaces by using Eqs. (A.7) and (A.8) [or Eqs. (A.3) and (A.4), respectively] to rewrite the derivatives for each coordinate.

A finite-difference Hamiltonian for Eq. (2.4) can be derived from the Schrödinger equation $\hat{H}_0\Psi(x, y) = E\Psi(x, y)$ by discretizing the wave function $\Psi_\alpha(x, y)$, where α refers to the four bands $|E \uparrow\rangle$, $|H \uparrow\rangle$, $|E \downarrow\rangle$, $|H \downarrow\rangle$ and the Hamiltonian for zero magnetic field \hat{H}_0 , given by Eq. (2.1). One can then write down a Hamiltonian for the discrete wave function $\Psi_\alpha(x_l, y_m)$ using the finite-difference formulas (A.7) and (A.8) and including the effect of the magnetic field by introducing the Peierls' phase to describe the vector potential given by Eq. (2.3) and an additional on-site term to describe the Zeeman term.¹ The resulting Hamiltonian is then defined in real space, that is, on a grid (x_l, y_m) . In general, this Hamiltonian has to be used to calculate the energy spectrum and eigenstates of the system.

However, if the gauge (2.3) is used, the momentum k along the x -direction is a good quantum number and we can use the ansatz

$$\Psi_\alpha(x_l, y_m) = (e^{ikla}/\sqrt{L})\psi_\alpha(y_m), \quad (\text{A.9})$$

where a is the distance between two grid points in the x -direction, to reduce this real-space Hamiltonian to the Hamiltonian (2.34) for a given k . Here, we note that in

¹Another way to derive a finite-difference Hamiltonian for Eq. (2.4) would have been to already start with the Schrödinger equation $\hat{H}\Psi(x, y) = E\Psi(x, y)$ instead of $\hat{H}_0\Psi(x, y) = E\Psi(x, y)$ and then discretize the vector potential in \hat{H} instead of including the Peierls' phase.

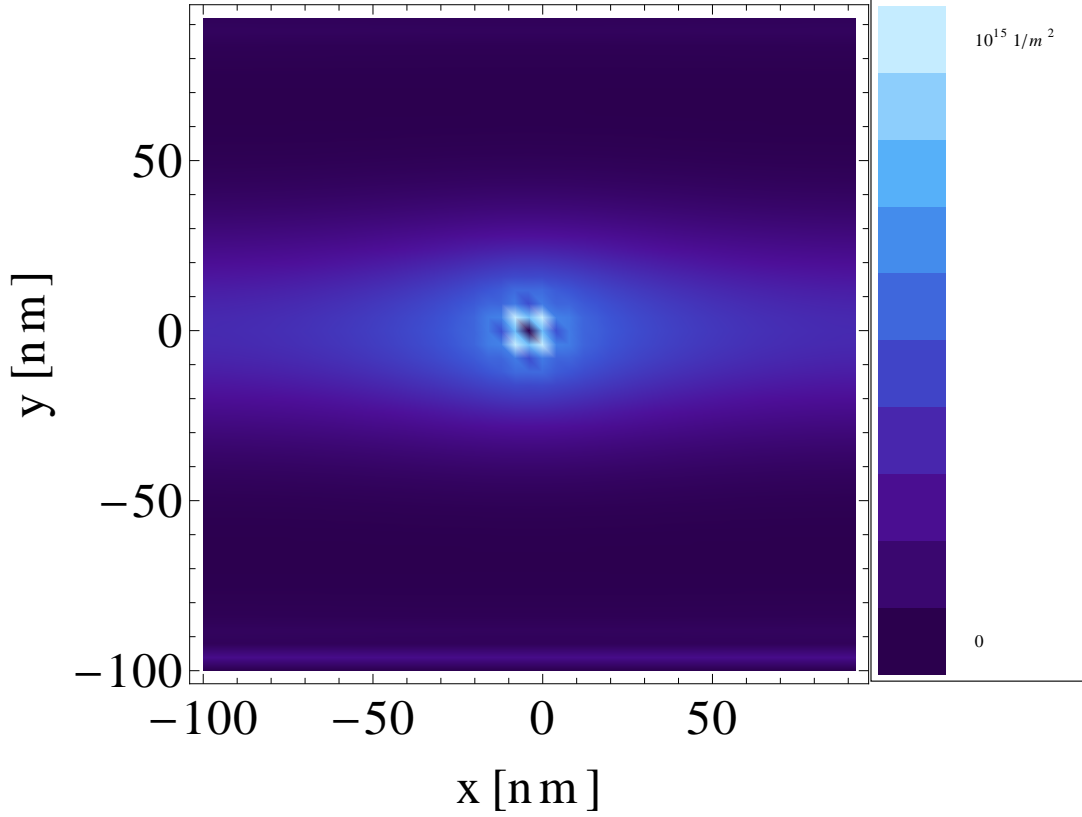


Figure A.1.: Calculated probability density, $\rho(x, y) = |\Psi(x, y)|^2$, of a spin-up bulk state for a HgTe quantum well with width $w = 200$ nm and $L = 200$ nm at $B = 0$ if a single point-like impurity is put in the center of the geometry. The parameters of the quantum well correspond to $d = 7.0$ nm.

writing down the Hamiltonian (2.34), the grid has been chosen such that the distance between two grid points in the y -direction is equal to the distance between two grid points in the x -direction.

If we consider the function $\psi_\alpha(y)$ to be defined on the interval $[-w/2, w/2]$, where w is the width of the interval, we can divide this interval into $N \in \mathbb{N}$ smaller intervals, each of width $a = w/N$. The grid points are then given by $y_l = -w/2 + al$ with $l = 0, 1, \dots, N$ and the discretized wave function by $\psi_\alpha(y_l)$. Since we look for wave function that satisfy the boundary condition $\psi_\alpha(\pm w/2) = 0$, we require $\psi_\alpha(y_0) = \psi_\alpha(y_N) = 0$. Thus, our task is to determine the remaining $4(N - 1)$ of $\psi_\alpha(y_l)$ (for $1 \leq l \leq N - 1$ and the four bands) from the algebraic equations obtained by applying the finite-difference scheme introduced above. However, one should note that Eqs. (A.7) and (A.8) cannot be used to evaluate derivatives at x_1 and x_{N-1} .

A. Finite-difference method

because only the nearest grid points x_0 and x_N , respectively, are known at the edges. Hence, one has to use Eqs. (A.3) and (A.4) to connect x_1 and x_{N-1} only to their nearest neighbors, x_0 and x_2 for x_1 and x_{N-2} and x_N for x_{N-1} .

Finally, as an example for the 2D finite-difference scheme, Fig. A.1 shows the probability density of a spin-up bulk state (in the lowest bulk conduction band) for a HgTe quantum well with width $w = 200$ nm and $L = 200$ nm at $B = 0$, where a single point-like impurity (of strength 10^{13} eV) is put in the center of the geometry. Due to this impurity, translational invariance is broken for the x - and y -directions and one can no longer reduce the problem to a 1D problem as in Sec. 2.2, but has to solve the problem in 2D. As in Sec. 2.2, periodic boundary conditions are applied along the x -direction and hard-wall boundary conditions are invoked for the $y = \pm w/2$. For the computation of the density, 51×51 grid points have been used to discretize the 2D structure. Figure A.1 illustrates how the probability density near the impurity is increased. Finally, we remark that there is also a spin-down state with the same energy and the same probability density and we refer to the Appendix E for an illustration of the current densities associated with the density shown in Fig. A.1.

B. Landau levels

In the absence of any confining potential, we require the wave functions given by Eqs. (2.21) and (2.22) to vanish for $\xi \rightarrow \pm\infty$, which can only be satisfied if the indices of the parabolic cylindrical functions are non-negative integers n . As above, we first consider spin-up electrons. Then, Eqs. (2.13) and (2.19) reduce to the ansatz

$$f_{\uparrow}(\xi) = v_1 \phi_n(\xi/\sqrt{2}) \quad \text{and} \quad g_{\uparrow}(\xi) = v_2 \phi_{n-1}(\xi/\sqrt{2}), \quad (\text{B.1})$$

valid for $n \geq 1$. For convenience, we have expressed the parabolic cylindrical functions $D_n(\xi)$ by the eigenfunctions of the one-dimensional harmonic oscillator,

$$\phi_n(\xi') = D_n(\sqrt{2}\xi')/\sqrt{n!\sqrt{\pi}} = e^{-\xi'^2/2} H_n(\xi')/\sqrt{2^n n! \sqrt{\pi}}, \quad (\text{B.2})$$

where $H_n(\xi')$ is the n -th Hermite polynomial. Inserting Eq. (B.1) into Eq. (2.10) and using the recurrence relations for the parabolic cylindrical functions (2.11) and (2.12) leads to the eigenvalue problem

$$\begin{pmatrix} \left[\mathcal{C} + \mathcal{M} - \frac{(\mathcal{D}+\mathcal{B})(2n+1)}{l_B^2} + \frac{g_e \mu_B B}{2} \right] & -\frac{\sqrt{2n}\mathcal{A}}{l_B} \\ -\frac{\sqrt{2n}\mathcal{A}}{l_B} & \left[\mathcal{C} - \mathcal{M} - \frac{(\mathcal{D}-\mathcal{B})(2n-1)}{l_B^2} + \frac{g_h \mu_B B}{2} \right] \end{pmatrix} \begin{pmatrix} v_1 \\ v_2 \end{pmatrix} = E \begin{pmatrix} v_1 \\ v_2 \end{pmatrix}. \quad (\text{B.3})$$

By determining the eigenvalues of Eq. (B.3) and their corresponding eigenvectors, we find the Landau levels (2.27) and their respective (normalized) eigenstates

$$\begin{aligned} \Psi_{n,k}^{\uparrow,\pm}(x, y) &= \frac{e^{ikx}}{\sqrt{L}} \begin{pmatrix} \frac{v_{n\pm}^{\uparrow}}{\sqrt{l_B}} \phi_n \left(\frac{y - kl_B^2}{l_B} \right) \\ \frac{u_{n\pm}^{\uparrow}}{\sqrt{l_B}} \phi_{n-1} \left(\frac{y - kl_B^2}{l_B} \right) \\ 0 \\ 0 \end{pmatrix} \\ &= \frac{e^{ikx}}{\sqrt{L}} \begin{pmatrix} \frac{(\sqrt{2n}\mathcal{A}/l_B \mp \Delta_{\uparrow,n}/2) - [\mathcal{M} - (2\mathcal{B}n + \mathcal{D})/l_B^2 + (g_e - g_h)\mu_B B/4]}{\sqrt{\Delta_{\uparrow,n}(\Delta_{\uparrow,n} \mp 2\sqrt{2n}\mathcal{A}/l_B)}\sqrt{l_B}} \phi_n \left(\frac{y - kl_B^2}{l_B} \right) \\ \frac{(\sqrt{2n}\mathcal{A}/l_B \mp \Delta_{\uparrow,n}/2) + [\mathcal{M} - (2\mathcal{B}n + \mathcal{D})/l_B^2 + (g_e - g_h)\mu_B B/4]}{\sqrt{\Delta_{\uparrow,n}(\Delta_{\uparrow,n} \mp 2\sqrt{2n}\mathcal{A}/l_B)}\sqrt{l_B}} \phi_{n-1} \left(\frac{y - kl_B^2}{l_B} \right) \\ 0 \\ 0 \end{pmatrix}, \quad (\text{B.4}) \end{aligned}$$

B. Landau levels

where

$$\Delta_{\uparrow,n} = 2\sqrt{\frac{2n\mathcal{A}^2}{l_B^2} + \left(\mathcal{M} - \frac{2\mathcal{B}n + \mathcal{D}}{l_B^2} + \frac{g_e - g_h}{4}\mu_B B\right)^2}. \quad (\text{B.5})$$

Whereas Eqs. (B.1) and (B.4) are valid for $n \geq 1$, one can also choose $n = 0$ to satisfy the boundary conditions. Instead of Eq. (B.1), one then has the ansatz

$$f_{\uparrow}(\xi) = v_1\phi_0(\xi/\sqrt{2}) \quad \text{and} \quad g_{\uparrow}(\xi) = 0, \quad (\text{B.6})$$

which yields the single Landau level given by Eq. (2.28) and its corresponding (normalized) eigenstates

$$\Psi_{0,k}^{\uparrow}(x, y) = \frac{e^{ikx}}{\sqrt{L}} \frac{1}{\sqrt{l_B}} \phi_0\left(\frac{y - kl_B^2}{l_B}\right) \begin{pmatrix} 1 \\ 0 \\ 0 \\ 0 \end{pmatrix}. \quad (\text{B.7})$$

If a similar procedure is applied for the spin-down states, one finds the Landau levels given by Eq. (2.29) with the eigenstates

$$\begin{aligned} \Psi_{n,k}^{\downarrow,\pm}(x, y) &= \frac{e^{ikx}}{\sqrt{L}} \begin{pmatrix} 0 \\ 0 \\ \frac{v_{n\pm}^{\downarrow}}{\sqrt{l_B}} \phi_{n-1}\left(\frac{y - kl_B^2}{l_B}\right) \\ \frac{u_{n\pm}^{\downarrow}}{\sqrt{l_B}} \phi_n\left(\frac{y - kl_B^2}{l_B}\right) \end{pmatrix} \\ &= \frac{e^{ikx}}{\sqrt{L}} \begin{pmatrix} 0 \\ 0 \\ \frac{-(\sqrt{2n}\mathcal{A}/l_B \pm \Delta_{\downarrow,n}/2) - [\mathcal{M} - (2\mathcal{B}n - \mathcal{D})/l_B^2 - (g_e - g_h)\mu_B B/4]}{\sqrt{\Delta_{\downarrow,n}(\Delta_{\downarrow,n} \pm 2\sqrt{2n}\mathcal{A}/l_B)}\sqrt{l_B}} \phi_{n-1}\left(\frac{y - kl_B^2}{l_B}\right) \\ \frac{-(\sqrt{2n}\mathcal{A}/l_B \pm \Delta_{\downarrow,n}/2) + [\mathcal{M} - (2\mathcal{B}n - \mathcal{D})/l_B^2 - (g_e - g_h)\mu_B B/4]}{\sqrt{\Delta_{\downarrow,n}(\Delta_{\downarrow,n} \pm 2\sqrt{2n}\mathcal{A}/l_B)}\sqrt{l_B}} \phi_n\left(\frac{y - kl_B^2}{l_B}\right) \end{pmatrix}, \end{aligned} \quad (\text{B.8})$$

where

$$\Delta_{\downarrow,n} = 2\sqrt{\frac{2n\mathcal{A}^2}{l_B^2} + \left(\mathcal{M} - \frac{2\mathcal{B}n - \mathcal{D}}{l_B^2} - \frac{g_e - g_h}{4}\mu_B B\right)^2}, \quad (\text{B.9})$$

and the single Landau level given by Eq. (2.30) with the eigenstate

$$\Psi_{0,k}^{\downarrow}(x, y) = \frac{e^{ikx}}{\sqrt{L}} \frac{1}{\sqrt{l_B}} \phi_0\left(\frac{y - kl_B^2}{l_B}\right) \begin{pmatrix} 0 \\ 0 \\ 0 \\ 1 \end{pmatrix}. \quad (\text{B.10})$$

C. Ground-state magnetization

As mentioned in Sec. 2.3.1, the ground-state energy (2.52) can be split in a—possibly not continuously differentiable—contribution from the uppermost valence band, that is, $\Omega_{\text{dis}}(B)$ given by Eq. (2.53), and a contribution from the remaining valence bands, $\tilde{\Omega}_0(B)$ given by Eq. (2.54). Likewise, one can divide the magnetization of the ground state into

$$M_{\text{dis}}(B) = -\frac{1}{S} \frac{\partial \Omega_{\text{dis}}(B)}{\partial B} \quad (\text{C.1})$$

and

$$\tilde{M}_0(B) = -\frac{1}{S} \frac{\partial \tilde{\Omega}_0(B)}{\partial B}. \quad (\text{C.2})$$

Figure C.1 (a) shows the contribution to the magnetization from the uppermost valence band, $M_{\text{dis}}(B)$, for parameters corresponding to the quantum-well thickness of $d = 7.0$ nm, that is, the inverted regime. Here, one can clearly see the discontinuity of $M_{\text{dis}}(B)$ at $B = B_c$. Comparing $M_{\text{dis}}(B)$ to the non-vacuum contribution $M(T, \mu, B)$ which is shown in Fig. C.1 (b) for $T = 10$ K and different densities illustrates how the discontinuity of $M(T, \mu, B)$ is canceled by the discontinuity of $M_{\text{dis}}(B)$. The resulting magnetization can be seen in Fig. 2.14 (b) in Sec. 2.3.2.

Apart from the contribution of $M_{\text{dis}}(B) + M(T, \mu, B)$, there is also a contribution arising from the remaining valence bands, $\tilde{M}_0(B)$. When using the effective model for HgTe quantum wells given by Eq. (2.4), the valence band Landau levels are not bounded from below and, thus, the sum over them is divergent. However, the effective model used in this work is only valid for low energies and there should be a lower bound for the valence band Landau levels of the real band structure. To remedy this, we adopt the approach from Refs. 53-55 and introduce a smooth cutoff function $g_{\text{co}}(\epsilon) = E_{\text{co}}^\alpha / (\epsilon^\alpha + E_{\text{co}}^\alpha)$ which we include in the thermodynamical quantities to smoothly cut off the respective summation over the Landau levels. Here, E_{co} and α denote the energy cutoff for the valence band Landau levels and a positive integer, respectively. Figure C.2 shows the contribution from $\tilde{M}_0(B)$ for $\alpha = 10$, several different energy cutoffs E_{co} , and band parameters in the inverted ($d = 7.0$ nm) and normal ($d = 5.5$ nm) regimes. The main feature in these graphs is the decay of the magnetization with increasing magnetic field, indicating a negative susceptibility and therefore diamagnetism.

C. Ground-state magnetization

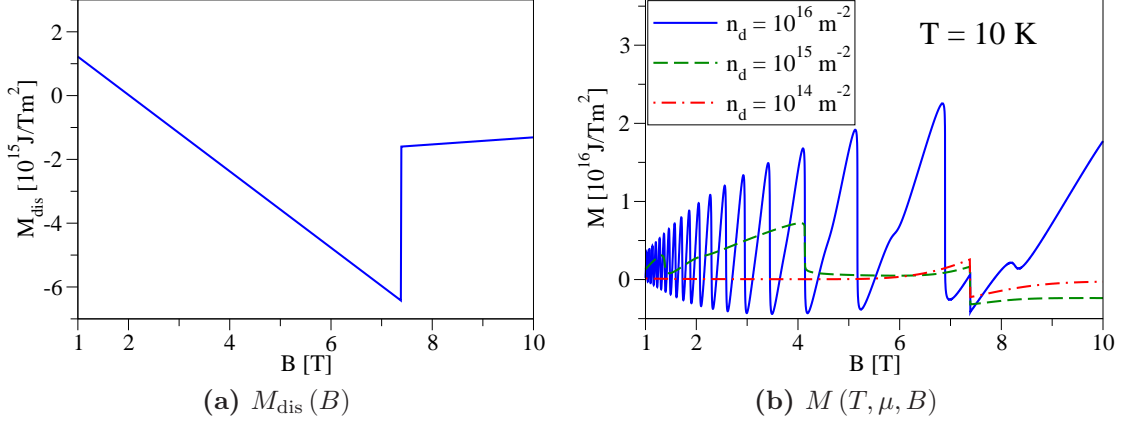


Figure C.1.: Magnetic field dependence of the magnetizations (a) $M_{\text{dis}}(B)$ and (b) $M(T, \mu, B)$ corresponding to a quantum-well thickness of $d = 7.0$ nm. The non-vacuum magnetization $M(T, \mu, B)$ is shown for $T = 10$ K and different densities ($n_d = 10^{14}, 10^{15}, 10^{16} \text{ 1/m}^2$)

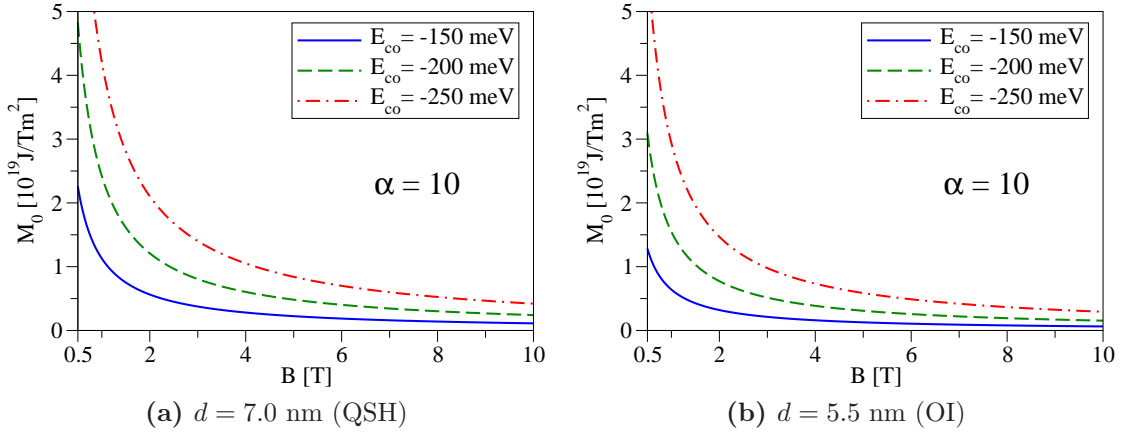


Figure C.2.: Magnetic field dependence of the vacuum magnetization $\tilde{M}_0(B)$ corresponding to quantum-well thicknesses of (a) $d = 7.0$ nm and (b) $d = 5.5$ nm and $\alpha = 10$.

D. Magnetization: Simplified model

In the following, we briefly discuss the magnetization for the special case of the reduced model for Eq. (2.4) mentioned in Sec. 2.1.3. If one chooses $\mathcal{C} = 0$, the bulk Landau levels (2.27)-(2.30) reduce to

$$E^{\uparrow/\downarrow}(0) = \pm \mathcal{M} \quad (\text{D.1})$$

and the degenerate levels

$$E_{\pm}^{\uparrow/\downarrow}(n) = \pm \sqrt{\frac{2n\mathcal{A}^2}{l_B^2} + \mathcal{M}^2} \quad (\text{D.2})$$

in this case.

If the simplified expressions (D.1) and (D.2) are used, the different contributions to the grand potential, $\Omega'(T, \mu, B)$, Eqs. (2.50), (2.51), and (2.52), read as

$$\Omega_e(T, \mu, B) = \frac{1}{2}f(0) + \sum_{n=1}^{\infty} f(n), \quad (\text{D.3})$$

$$\Omega_h(T, \mu, B) = \Omega_e(T, -\mu, B), \quad (\text{D.4})$$

and

$$\Omega_0(B) = \frac{1}{2}g(0) + \sum_{n=1}^{\infty} g(n), \quad (\text{D.5})$$

where

$$f(x) = -\frac{2SB}{\beta\Phi_0} \ln \left[1 + e^{-\beta(\sqrt{2x\mathcal{A}^2/l_B^2 + \mathcal{M}^2} - \mu)} \right] \quad (\text{D.6})$$

and

$$g(x) = -\frac{2SB}{\Phi_0} \sqrt{\frac{2x\mathcal{A}^2}{l_B^2} + \mathcal{M}^2}. \quad (\text{D.7})$$

In the following, we will look at the behavior of the magnetization in the regime of $2(\mathcal{A}\beta/l_B)^2 \ll 1$ as well as the de Haas-van Alphen oscillations within the model given by Eqs. (D.1) and (D.2). For both cases, we assume to be in the degenerate limit, that is, $\beta|\mu| \gg 1$. Since the Landau levels of this reduced model correspond to those of 2D Dirac fermions, most notably those of (monolayer) graphene, one can apply the same procedures as in these cases.

D. Magnetization: Simplified model

'Weak' magnetic fields

For magnetic fields with $2(\mathcal{A}\beta/l_B)^2 \ll 1$, we follow the classic Landau approach [154] and use the Euler-Maclaurin formula to express $\Omega_e(T, \mu, B)$ as

$$\Omega_e(T, \mu, B) \approx \int_0^\infty dx f(x) - \frac{1}{12} \left. \frac{df(x)}{dx} \right|_{x=0}. \quad (\text{D.8})$$

When conducting the transformation $x/l_B^2 \rightarrow x$, one can see that the integral in Eq. (D.8) [denoted as $F(T, \mu)$ in the following] does not depend on the magnetic field and one arrives at

$$\Omega_e(T, \mu, B) \approx F(T, \mu) - \frac{S\mathcal{A}^2}{12\pi l_B^4 |\mathcal{M}|} \frac{1}{e^{\beta(|\mathcal{M}|-\mu)} + 1}. \quad (\text{D.9})$$

By the same procedure [and assuming a cutoff for $g(x)$], we obtain

$$\Omega_0(B) \approx c_0 + \frac{S\mathcal{A}^2}{12\pi l_B^4 |\mathcal{M}|}, \quad (\text{D.10})$$

where c_0 does not depend on the magnetic field. Then, the grand canonical potential can be written as

$$\begin{aligned} \Omega'(T, \mu, B) &= \Omega_0(B) + \Omega_e(T, \mu, B) + \Omega_e(T, -\mu, B) \\ &\approx \tilde{F}(T, \mu) + \frac{S\pi\mathcal{A}^2 B^2}{3\Phi_0^2 |\mathcal{M}|} \frac{\sinh(\beta |\mathcal{M}|)}{\cosh(\beta |\mathcal{M}|) + \cosh(\beta \mu)}, \end{aligned} \quad (\text{D.11})$$

where the different B -independent contributions have been combined in the function $\tilde{F}(T, \mu)$. Note, that the expansion used to arrive at Eq. (D.11) is valid for $2(\mathcal{A}\beta/l_B)^2 \ll 1$.

Consequently, we find for the magnetic susceptibility

$$\chi_{\text{tot}}(T, \mu) = -\frac{2\pi\mathcal{A}^2}{3\Phi_0^2 |\mathcal{M}|} \frac{\sinh(\beta |\mathcal{M}|)}{\cosh(\beta |\mathcal{M}|) + \cosh(\beta \mu)}, \quad (\text{D.12})$$

implying that the system is diamagnetic. This result generalizes the zero-temperature formula of graphene found in Ref. 54, but also the $\mathcal{M} = 0$ model of $\text{Pb}_{1-x}\text{Sn}_x\text{Te}$ interface states found in Ref. 28.

De Haas-van Alphen oscillations

To calculate the de Haas-van Alphen oscillations for $|\mu| > |\mathcal{M}|$, we only need to look at the non-vacuum contributions $\Omega_e(T, \mu, B)$ and $\Omega_h(T, \mu, B)$. We again follow Ref. 154 as well as Ref. 155 and use Poisson's summation formula to write

$$\Omega_e(T, \mu, B) \approx \int_0^\infty dx f(x) + 2\text{Re} \left[\sum_{k=1}^\infty \int_0^\infty dx f(x) e^{2\pi i k x} \right], \quad (\text{D.13})$$

where the first and second terms describe the non-oscillating and oscillating parts of the grand potential, respectively. Here, we are interested in the oscillating part [denoted by $\Omega_{\text{osc}}^e(T, \mu, B)$ in the following]. This part can be rewritten as

$$\Omega_{\text{osc}}^e(T, \mu, B) = -\frac{4SB}{\beta\Phi_0} \text{Re} \left\{ \sum_{k=1}^{\infty} \frac{1}{2\pi i k \xi} \int_{|\mathcal{M}/\mu|}^{\infty} dy \frac{e^{2\pi i k x(y)}}{e^{[y - \text{sgn}(\mu)]/\xi} + 1} \right\}, \quad (\text{D.14})$$

where

$$x(y) = \frac{1}{2} \left(\frac{\mu l_B}{\mathcal{A}} \right)^2 \left(y^2 - \frac{\mathcal{M}^2}{\mu^2} \right) \quad (\text{D.15})$$

and $\xi = 1/(\beta|\mu|)$.

We first consider the case $\mu > |\mathcal{M}|$. In this case, a major contribution to the integral originates from the vicinity of the Fermi level, that is, from $y \sim 1$, whereas the integrand is damped for values $y \gtrsim 1$. Therefore, we expand $x(y)$ around $y = 1$ and replace the lower boundary of the integral by $y \rightarrow -\infty$. Changing the integration variable to $x = (y - 1)/\xi$, we find that the oscillating part of the grand potential is given by

$$\Omega_{\text{osc}}^e(T, \mu, B) = \frac{2SB}{\pi\Phi_0\beta} \text{Re} \left\{ \sum_{k=1}^{\infty} \frac{i e^{i\pi k (l_B/\mathcal{A})^2 (\mu^2 - \mathcal{M}^2)}}{k} \int_{-\infty}^{\infty} dx \frac{e^{2\pi i (\mu l_B/\mathcal{A})^2 \xi k x}}{e^x + 1} \right\}. \quad (\text{D.16})$$

Computing the integral, we can write the oscillating part of the electronic contribution to the grand potential as

$$\Omega_{\text{osc}}^e(T, \mu, B) = \frac{2SB}{\Phi_0\beta} \sum_{k=1}^{\infty} \frac{\cos[\pi k (l_B/\mathcal{A})^2 (\mu^2 - \mathcal{M}^2)]}{k \sinh[2\pi^2 k \xi (\mu l_B/\mathcal{A})^2]}, \quad (\text{D.17})$$

with $\mu > |\mathcal{M}|$. For $\mu < |\mathcal{M}|$, the contribution from the oscillating part of the electrons is much smaller than Eq. (D.17) and in the case of $\mu < -|\mathcal{M}|$, the main contribution arises from the hole contribution given by $\Omega_{\text{osc}}^h(T, \mu, B) = \Omega_{\text{osc}}^e(T, -\mu, B)$. Thus, the total oscillating part of the grand potential is given by Eq. (D.17) for any $|\mu| > |\mathcal{M}|$. By taking the derivative, one obtains the oscillating part of the total magnetization, which is periodic in $1/B$.

Finally, we emphasize that this reduced model discussed here cannot describe a transition between inverted and normal band structures and can thus only be used for magnetic fields well below the crossover point (or for situations where there is no crossover at all).

E. Current densities

For an arbitrary magnetic field, Eq. (2.4) has to be replaced by

$$\begin{aligned}\hat{H} = & \mathcal{C}\mathbf{1} + \mathcal{M}\Gamma_5 + \frac{\mu_B [\nabla \times \mathbf{A}(\mathbf{r})] \Gamma_g}{2} \\ & - \frac{\mathcal{D}\mathbf{1} + \mathcal{B}\Gamma_5}{\hbar^2} \{ [\hat{p}_x - A_x(\mathbf{r})]^2 + [\hat{p}_y - A_y(\mathbf{r})]^2 \} \\ & + \frac{\mathcal{A}\Gamma_1}{\hbar} [\hat{p}_x - A_x(\mathbf{r})] + \frac{\mathcal{A}\Gamma_2}{\hbar} [\hat{p}_y - A_y(\mathbf{r})],\end{aligned}\quad (\text{E.1})$$

where $\Gamma_g = (\Gamma_g^x, \Gamma_g^y, \Gamma_g^z)$ and the additional 4×4 matrices

$$\Gamma_g^x = \begin{pmatrix} 0 & g_{\parallel}\mathbf{1} \\ g_{\parallel}\mathbf{1} & 0 \end{pmatrix}, \Gamma_g^y = \begin{pmatrix} 0 & -ig_{\parallel}\mathbf{1} \\ ig_{\parallel}\mathbf{1} & 0 \end{pmatrix}, \quad (\text{E.2})$$

as well as the effective in-plane g-factor g_{\parallel} have been introduced [17].

For an arbitrary (normalized) state $\Psi(x, y)$, the corresponding energy expectation value as a functional of the vector potential $\mathbf{A}(\mathbf{r})$ is given by

$$E[\mathbf{A}] = \sum_{\alpha\beta} \int d^2r \Psi_{\alpha}^*(x, y) H_{\alpha\beta} \Psi_{\beta}(x, y), \quad (\text{E.3})$$

where the sums over α and β refer to the four bands considered, that is, $|E \uparrow\rangle, |H \uparrow\rangle, |E \downarrow\rangle, |H \downarrow\rangle$. The particle current density $\mathbf{j}(\mathbf{r})$ of this state $\Psi(\mathbf{r})$ can be determined by a variational method:

$$\delta E = E[\mathbf{A} + \delta\mathbf{A}] - E[\mathbf{A}] = e \int d^2r \mathbf{j}(x, y) \delta\mathbf{A}(\mathbf{r}). \quad (\text{E.4})$$

This procedure yields the current density $\mathbf{j}(x, y) = \mathbf{j}_e(x, y) + \mathbf{j}_i(x, y)$ composed of the external current density,

$$\begin{aligned}\mathbf{j}_e(x, y) = & \sum_{\alpha\beta} \left\{ \frac{i}{\hbar} \left[\mathcal{D}(\mathbf{1})_{\alpha\beta} + \mathcal{B}(\Gamma_5)_{\alpha\beta} \right] [\Psi_{\alpha}^* (\nabla \Psi_{\beta}) - (\nabla \Psi_{\alpha}^*) \Psi_{\beta}] \right. \\ & \left. + \frac{\mathcal{A}}{\hbar} (\Gamma)_{\alpha\beta} \Psi_{\alpha}^* \Psi_{\beta} - \frac{2e}{\hbar^2} \left[\mathcal{D}(\mathbf{1})_{\alpha\beta} + \mathcal{B}(\Gamma_5)_{\alpha\beta} \right] \Psi_{\alpha}^* \Psi_{\beta} \mathbf{A} \right\},\end{aligned}\quad (\text{E.5})$$

E. Current densities

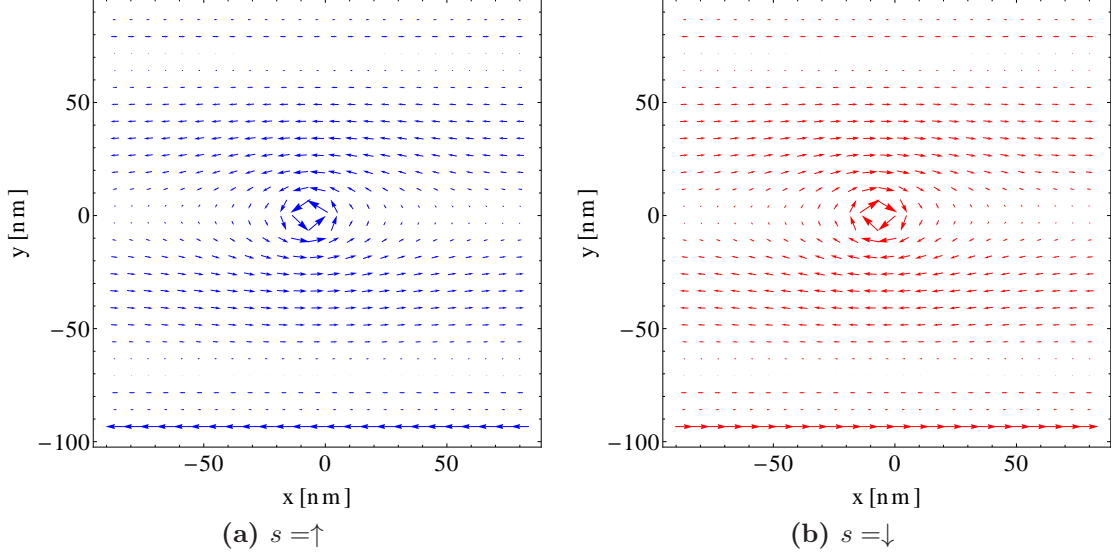


Figure E.1.: Calculated current densities $\mathbf{j}(x, y)$ of the same (a) spin-up and (b) spin-down states as in Fig. A.1.

where $\mathbf{\Gamma} = (\Gamma_1, \Gamma_2, 0)$, and the internal current density,

$$\mathbf{j}_i(x, y) = \frac{\mu_B}{2e} \nabla \times \left[\sum_{\alpha\beta} \Psi_\alpha^* (\mathbf{\Gamma}_g)_{\alpha\beta} \Psi_\beta \right]. \quad (\text{E.6})$$

As we are dealing with a 2D system, Eqs. (E.5) and (E.6) are to be read as applying only to the x - and y -components.

We note that the external current density could also have been obtained by calculating the velocity operator $\hat{\mathbf{v}} = [\hat{\mathbf{r}}, \hat{H}] / i\hbar$ and using $\mathbf{j} = [\Psi^* (\hat{\mathbf{v}} \Psi) + (\hat{\mathbf{v}} \Psi)^* \Psi] / 2$. However, such a procedure would not have taken into account the presence of the internal current.

As an example of the current density, Fig. E.1 shows the current densities for the spin-up bulk state shown in Fig. A.1 and the corresponding spin-down state with the same energy and density. Figure E.1 also illustrates that electrons with opposite spins move in opposite directions. We find that the contribution from the internal current $\mathbf{j}_i(x, y)$ is roughly two orders of magnitudes smaller than $\mathbf{j}_e(x, y)$, which therefore gives the dominant contribution to the total current density.

Bibliography

- [1] A. K. Geim and K. S. Novoselov, *Nat. Mater.* **6**, 183 (2007).
- [2] A. H. Castro Neto, F. Guinea, N. M. R. Peres, K. S. Novoselov, and A. K. Geim, *Rev. Mod. Phys.* **81**, 109 (2009).
- [3] M. Z. Hasan and C. L. Kane, *Rev. Mod. Phys.* **82**, 3045 (2010).
- [4] X.-L. Qi and S.-C. Zhang, *Rev. Mod. Phys.* **83**, 1057 (2011).
- [5] F. Wilczek, *Nature Physics* **5**, 614 (2009).
- [6] M. Franz, *Physics* **3**, 24 (2010).
- [7] G. E. W. Bauer, E. Saitoh, and B. J. van Wees, *Nat. Mater.* **11**, 391 (2012).
- [8] I. Žutić, J. Fabian, and S. Das Sarma, *Rev. Mod. Phys.* **76**, 323 (2004).
- [9] J. Fabian, A. Matos-Abiague, C. Ertler, P. Stano, and I. Žutić, *Acta Phys. Slov.* **57**, 565 (2007).
- [10] C. L. Kane and E. J. Mele, *Phys. Rev. Lett.* **95**, 146802 (2005).
- [11] C. L. Kane and E. J. Mele, *Phys. Rev. Lett.* **95**, 226801 (2005).
- [12] B. A. Bernevig, T. L. Hughes, and S.-C. Zhang, *Science* **314**, 1757 (2006).
- [13] B. A. Bernevig and S.-C. Zhang, *Phys. Rev. Lett.* **96**, 106802 (2006).
- [14] S. Murakami, *Phys. Rev. Lett.* **97**, 236805 (2006).
- [15] C. Liu, T. L. Hughes, X.-L. Qi, K. Wang, and S.-C. Zhang, *Phys. Rev. Lett.* **100**, 236601 (2008).
- [16] M. König, S. Wiedmann, C. Brüne, A. Roth, H. Buhmann, L. W. Molenkamp, X.-L. Qi, and S.-C. Zhang, *Science* **318**, 766 (2007).
- [17] M. König, H. Buhmann, L. W. Molenkamp, T. Hughes, C.-X. Liu, X.-L. Qi, and S.-C. Zhang, *Journal of the Physical Society of Japan* **77**, 031007 (2008).

Bibliography

- [18] B. Büttner, C. X. Liu, G. Tkachov, E. G. Novik, C. Brüne, H. Buhmann, E. M. Hankiewicz, P. Recher, B. Trauzettel, S. C. Zhang, et al., *Nature Physics* **7**, 418 (2011).
- [19] C. Brüne, A. Roth, H. Buhmann, E. M. Hankiewicz, L. W. Molenkamp, J. Maciejko, X.-L. Qi, and S.-C. Zhang, *Nature Physics* **8**, 486 (2012).
- [20] D. J. Thouless, M. Kohmoto, M. P. Nightingale, and M. den Nijs, *Phys. Rev. Lett.* **49**, 405 (1982).
- [21] M. Kohmoto, *Annals of Physics* **160**, 343 (1985).
- [22] C. Wu, B. A. Bernevig, and S.-C. Zhang, *Phys. Rev. Lett.* **96**, 106401 (2006).
- [23] C. Xu and J. E. Moore, *Phys. Rev. B* **73**, 045322 (2006).
- [24] D. J. Chadi, J. P. Walter, M. L. Cohen, Y. Petroff, and M. Balkanski, *Phys. Rev. B* **5**, 3058 (1972).
- [25] Z. Zhu, Y. Cheng, and U. Schwingenschlögl, *Phys. Rev. B* **85**, 235401 (2012).
- [26] L. Fu and C. L. Kane, *Phys. Rev. B* **76**, 045302 (2007).
- [27] M. I. D'yakonov and A. V. Khaetskii, *JETP Letters* **33**, 110 (1981).
- [28] B. A. Volkov and O. A. Pankratov, *JETP Letters* **42**, 178 (1985).
- [29] O. Pankratov, S. Pakhomov, and B. Volkov, *Solid State Communications* **61**, 93 (1987).
- [30] D. G. Rothe, R. W. Reinthaler, C.-X. Liu, L. W. Molenkamp, S.-C. Zhang, and E. M. Hankiewicz, *New Journal of Physics* **12**, 065012 (2010).
- [31] R. W. Reinthaler and E. M. Hankiewicz, *Phys. Rev. B* **85**, 165450 (2012).
- [32] G. Tkachov and E. M. Hankiewicz, *Phys. Rev. Lett.* **104**, 166803 (2010).
- [33] G. Tkachov and E. Hankiewicz, *Physica E: Low-dimensional Systems and Nanostructures* **44**, 900 (2012).
- [34] J.-C. Chen, J. Wang, and Q.-F. Sun, *Phys. Rev. B* **85**, 125401 (2012).
- [35] J. Linder, T. Yokoyama, and A. Sudbø, *Phys. Rev. B* **80**, 205401 (2009).
- [36] C.-X. Liu, H. Zhang, B. Yan, X.-L. Qi, T. Frauenheim, X. Dai, Z. Fang, and S.-C. Zhang, *Phys. Rev. B* **81**, 041307 (2010).

-
- [37] H.-Z. Lu, W.-Y. Shan, W. Yao, Q. Niu, and S.-Q. Shen, Phys. Rev. B **81**, 115407 (2010).
 - [38] B. Zhou, H.-Z. Lu, R.-L. Chu, S.-Q. Shen, and Q. Niu, Phys. Rev. Lett. **101**, 246807 (2008).
 - [39] V. Krueckl and K. Richter, Phys. Rev. Lett. **107**, 086803 (2011).
 - [40] V. L. Grigoryan, A. Matos-Abiague, and S. M. Badalyan, Phys. Rev. B **80**, 165320 (2009).
 - [41] S. M. Badalyan and J. Fabian, Phys. Rev. Lett. **105**, 186601 (2010).
 - [42] Y. Zhou and F.-C. Zhang, Nature Physics **8**, 448 (2012).
 - [43] X.-L. Qi and S.-C. Zhang, Physics Today **63**, 33 (2010).
 - [44] H. C. Manoharan, Nature Nanotechnology **5**, 477 (2010).
 - [45] M. J. Schmidt, E. G. Novik, M. Kindermann, and B. Trauzettel, Phys. Rev. B **79**, 241306 (2009).
 - [46] F. W. J. Olver, D. W. Lozier, R. F. Boisvert, and C. W. Clark, *NIST Handbook of Mathematical Functions* (Cambridge Univ. Press, New York, 2010).
 - [47] S. Datta, *Electronic transport in mesoscopic systems* (Cambridge Univ. Press, Cambridge, 2007).
 - [48] R. Peierls, Zeitschrift für Physik A Hadrons and Nuclei **80**, 763 (1933).
 - [49] J. R. Meyer, R. J. Wagner, F. J. Bartoli, C. A. Hoffman, M. Dobrowolska, T. Wojtowicz, J. K. Furdyna, and L. R. Ram-Mohan, Phys. Rev. B **42**, 9050 (1990).
 - [50] M. von Truchsess, A. Pfeuffer-Jeschke, V. Latussek, C. R. Becker, and E. Batke, in *High Magnetic Fields in the Physics of Semiconductors II*, edited by G. Landwehr and W. Ossau (World Scientific, Singapore, 1997), vol. 2, p. 813.
 - [51] M. Schultz, U. Merkt, A. Sonntag, U. Rössler, R. Winkler, T. Colin, P. Helgesen, T. Skauli, and S. Løvold, Phys. Rev. B **57**, 14772 (1998).
 - [52] S. G. Sharapov, V. P. Gusynin, and H. Beck, Phys. Rev. B **69**, 075104 (2004).
 - [53] M. Koshino and T. Ando, Phys. Rev. B **75**, 235333 (2007).
 - [54] M. Koshino and T. Ando, Phys. Rev. B **81**, 195431 (2010).

Bibliography

- [55] Y. Ominato and M. Koshino, Phys. Rev. B **85**, 165454 (2012).
- [56] G. D. Mahan, *Many-Particle Physics* (Kluwer/Plenum, New York, 2000).
- [57] A. L. Fetter and J. D. Walecka, *Quantum Theory of Many-Particle Systems* (Dover Publ., Mineola, N.Y., 2003).
- [58] H. Bruus and K. Flensberg, *Many Body Quantum Theory in Condensed Matter Physics* (Oxford Univ. Press, Oxford, 2006).
- [59] K. S. Novoselov, A. K. Geim, S. V. Morozov, D. Jiang, Y. Zhang, S. V. Dubonos, I. V. Grigorieva, and A. A. Firsov, Science **306**, 666 (2004).
- [60] P. R. Wallace, Phys. Rev. **71**, 622 (1947).
- [61] J. W. McClure, Phys. Rev. **108**, 612 (1957).
- [62] J. C. Slonczewski and P. R. Weiss, Phys. Rev. **109**, 272 (1958).
- [63] K. S. Novoselov, A. K. Geim, S. V. Morozov, D. Jiang, M. I. Katsnelson, I. V. Grigorieva, S. V. Dubonos, and A. A. Firsov, Nature (London) **438**, 197 (2005).
- [64] R. R. Nair, P. Blake, A. N. Grigorenko, K. S. Novoselov, T. J. Booth, T. Stauber, N. M. R. Peres, and A. K. Geim, Science **320**, 1308 (2008).
- [65] Z. Q. Li, E. A. Henriksen, Z. Jiang, Z. Hao, M. C. Martin, P. Kim, H. L. Stormer, and D. N. Basov, Nat. Phys. **4**, 532 (2008).
- [66] K. F. Mak, M. Y. Sfeir, Y. Wu, C. H. Lui, J. A. Misewich, and T. F. Heinz, Phys. Rev. Lett. **101**, 196405 (2008).
- [67] J. Horng, C.-F. Chen, B. Geng, C. Girit, Y. Zhang, Z. Hao, H. A. Bechtel, M. Martin, A. Zettl, M. F. Crommie, et al., Phys. Rev. B **83**, 165113 (2011).
- [68] N. M. R. Peres, F. Guinea, and A. H. Castro Neto, Phys. Rev. B **73**, 125411 (2006).
- [69] V. P. Gusynin and S. G. Sharapov, Phys. Rev. B **73**, 245411 (2006).
- [70] V. P. Gusynin, S. G. Sharapov, and J. P. Carbotte, Phys. Rev. Lett. **96**, 256802 (2006).
- [71] L. A. Falkovsky and S. S. Pershoguba, Phys. Rev. B **76**, 153410 (2007).
- [72] T. Stauber and N. M. R. Peres, Journal of Physics: Condensed Matter **20**, 055002 (2008).

- [73] T. Stauber, N. M. R. Peres, and A. H. Castro Neto, Phys. Rev. B **78**, 085418 (2008).
- [74] T. Stauber, N. M. R. Peres, and A. K. Geim, Phys. Rev. B **78**, 085432 (2008).
- [75] N. M. R. Peres, T. Stauber, and A. H. C. Neto, EPL (Europhysics Letters) **84**, 38002 (2008).
- [76] L. A. Falkovsky, Physics-Uspekhi **51**, 887 (2008a).
- [77] L. Falkovsky, Journal of Experimental and Theoretical Physics **106**, 575 (2008b).
- [78] J. P. Carbotte, E. J. Nicol, and S. G. Sharapov, Phys. Rev. B **81**, 045419 (2010).
- [79] N. M. R. Peres, R. M. Ribeiro, and A. H. Castro Neto, Phys. Rev. Lett. **105**, 055501 (2010).
- [80] S. H. Abedinpour, G. Vignale, A. Principi, M. Polini, W.-K. Tse, and A. H. MacDonald, Phys. Rev. B **84**, 045429 (2011).
- [81] V. P. Gusynin, S. G. Sharapov, and J. P. Carbotte, Journal of Physics: Condensed Matter **19**, 026222 (2007).
- [82] V. P. Gusynin, S. G. Sharapov, and J. P. Carbotte, Phys. Rev. Lett. **98**, 157402 (2007).
- [83] V. P. Gusynin, S. G. Sharapov, and J. P. Carbotte, Phys. Rev. B **75**, 165407 (2007).
- [84] A. Pound, J. P. Carbotte, and E. J. Nicol, Phys. Rev. B **85**, 125422 (2012).
- [85] V. Perebeinos, J. Tersoff, and P. Avouris, Phys. Rev. Lett. **94**, 027402 (2005).
- [86] V. Perebeinos, J. Tersoff, and P. Avouris, Phys. Rev. Lett. **94**, 086802 (2005).
- [87] V. Perebeinos and P. Avouris, Phys. Rev. B **81**, 195442 (2010).
- [88] R. Kim, V. Perebeinos, and P. Avouris, Phys. Rev. B **84**, 075449 (2011).
- [89] S. Piscanec, M. Lazzeri, F. Mauri, A. C. Ferrari, and J. Robertson, Phys. Rev. Lett. **93**, 185503 (2004).
- [90] M. Lazzeri, S. Piscanec, F. Mauri, A. C. Ferrari, and J. Robertson, Phys. Rev. Lett. **95**, 236802 (2005).
- [91] T. Ando, Journal of the Physical Society of Japan **75**, 124701 (2006).

Bibliography

- [92] K. Ishikawa and T. Ando, Journal of the Physical Society of Japan **75**, 084713 (2006).
- [93] S. Piscanec, M. Lazzeri, J. Robertson, A. C. Ferrari, and F. Mauri, Phys. Rev. B **75**, 035427 (2007).
- [94] S. Fratini and F. Guinea, Phys. Rev. B **77**, 195415 (2008).
- [95] A. Konar, T. Fang, and D. Jena, Phys. Rev. B **82**, 115452 (2010).
- [96] S. Q. Wang and G. D. Mahan, Phys. Rev. B **6**, 4517 (1972).
- [97] B. Wunsch, T. Stauber, F. Sols, and F. Guinea, New Journal of Physics **8**, 318 (2006).
- [98] E. H. Hwang and S. Das Sarma, Phys. Rev. B **75**, 205418 (2007).
- [99] S. D. Sarma, J. Fabian, X. Hu, and I. Žutić, Superlattices and Microstructures **27**, 289 (2000).
- [100] S. D. Sarma, J. Fabian, X. Hu, and I. Žutić, Solid State Commun. **119**, 207 (2001).
- [101] J. Fabian and I. Žutić, in *From GMR to Quantum Information*, edited by S. Blügel *et al.* (Forschungszentrum Jülich 2009).
- [102] M. J. Stevens, A. L. Smirl, R. D. R. Bhat, A. Najmaie, J. E. Sipe, and H. M. van Driel, Phys. Rev. Lett. **90**, 136603 (2003).
- [103] T. Kimura, Y. Otani, T. Sato, S. Takahashi, and S. Maekawa, Phys. Rev. Lett. **98**, 156601 (2007).
- [104] I. Žutić and H. Dery, Nat. Mater. **10**, 646 (2011).
- [105] K. Ando, S. Takahashi, J. Ieda, H. Kurebayashi, T. Trypiniotis, C. H. W. Barnes, S. Maekawa, and E. Saitoh, Nat. Mater. **10**, 655 (2011).
- [106] H. Kurebayashi, O. Dzyapko, V. E. Demidov, D. Fang, A. J. Ferguson, and S. O. Demokritov, Nat. Mater. **10**, 660 (2011).
- [107] A. G. Aronov, JETP Lett. **24**, 32 (1976).
- [108] M. Johnson and R. H. Silsbee, Phys. Rev. Lett. **55**, 1790 (1985).
- [109] M. Johnson and R. H. Silsbee, Phys. Rev. B **35**, 4959 (1987).
- [110] M. Johnson and R. H. Silsbee, Phys. Rev. B **37**, 5312 (1988).

- [111] E. Rashba, Eur. Phys. J. B **29**, 513 (2002).
- [112] D. Kochan, M. Gmitra, and J. Fabian, Phys. Rev. Lett. **107**, 176604 (2011).
- [113] J.-E. Wegrowe, Phys. Rev. B **62**, 1067 (2000).
- [114] G. E. Bauer, A. H. MacDonald, and S. Maekawa, Solid State Commun. **150**, 459 (2010).
- [115] M. Johnson, Solid State Commun. **150**, 543 (2010).
- [116] H. B. Callen, *Thermodynamics* (Wiley, New York, 1960).
- [117] N. W. Ashcroft and N. D. Mermin, *Solid State Physics* (Brooks/Cole Thomson Learning, Singapore, 2006).
- [118] A. Fukushima, K. Yagami, A. A. Tulapurkar, Y. Suzuki, H. Kubota, A. Yamamoto, and S. Yuasa, Jap. J. Appl. Phys. **44**, L12 (2005).
- [119] A. Fukushima, H. Kubota, A. Yamamoto, Y. Suzuki, and S. Yuasa, IEEE Trans. Magn. **41**, 2571 (2005).
- [120] L. Gravier, S. Serrano-Guisan, F. Reuse, and J.-P. Ansermet, Phys. Rev. B **73**, 024419 (2006).
- [121] L. Gravier, S. Serrano-Guisan, F. Reuse, and J.-P. Ansermet, Phys. Rev. B **73**, 052410 (2006).
- [122] M. V. Costache, G. Bridoux, I. Neumann, and S. O. Valenzuela, Nat. Mater. **11**, 199 (2012).
- [123] K. Uchida, S. Takahashi, K. Harii, J. Ieda, W. Koshibae, K. Ando, S. Maekawa, and E. Saitoh, Nature (London) **455**, 778 (2008).
- [124] K. Uchida, T. Ota, K. Harii, K. Ando, H. Nakayama, and E. Saitoh, J. Appl. Phys. **107**, 09A951 (2010).
- [125] K. Uchida, J. Xiao, H. Adachi, J. Ohe, S. Takahashi, J. Ieda, T. Ota, Y. Kajiwara, H. Umezawa, H. Kawai, et al., Nat. Mater. **9**, 894 (2010).
- [126] K. Uchida, S. Takahashi, J. Ieda, K. Harii, K. Ikeda, W. Koshibae, S. Maekawa, and E. Saitoh, J. Appl. Phys. **105**, 07C908 (2009).
- [127] S. D. Bader and S. S. P. Parkin, Annu. Rev. Condens. Matter Phys. **1**, 71 (2010).
- [128] C. M. Jaworski, J. Yang, S. Mack, D. D. Awschalom, J. P. Heremans, and R. C. Myers, Nat. Mater. **9**, 898 (2010).

Bibliography

- [129] S. O. Valenzuela and M. Tinkham, *Nature (London)* **442**, 176 (2006).
- [130] E. Saitoh, M. Ueda, H. Miyajima, and G. Tatara, *Appl. Phys. Lett.* **88**, 182509 (2006).
- [131] J. Xiao, G. E. W. Bauer, K.-C. Uchida, E. Saitoh, and S. Maekawa, *Phys. Rev. B* **81**, 214418 (2010).
- [132] H. Adachi, K. ichi Uchida, E. Saitoh, J. ichiro Ohe, S. Takahashi, and S. Maekawa, *Appl. Phys. Lett.* **97**, 252506 (2010).
- [133] C. M. Jaworski, J. Yang, S. Mack, D. D. Awschalom, R. C. Myers, and J. P. Heremans, *Phys. Rev. Lett.* **106**, 186601 (2011).
- [134] A. Slachter, F. L. Bakker, and B. J. van Wees, *Phys. Rev. B* **84**, 174408 (2011).
- [135] J. Flipse, F. L. Bakker, A. Slachter, F. K. Dejene, and B. J. van Wees, *Nature Nanotechnology* **7**, 166 (2012).
- [136] A. Slachter, F. L. Bakker, J.-P. Adam, and B. J. van Wees, *Nat. Phys.* **6**, 879 (2010).
- [137] F. L. Bakker, A. Slachter, J.-P. Adam, and B. J. van Wees, *Phys. Rev. Lett.* **105**, 136601 (2010).
- [138] J.-C. Le Breton, S. Sharma, H. Saito, S. Yuasa, and R. Jansen, *Nature (London)* **475**, 82 (2011).
- [139] M. Hatami, G. E. W. Bauer, Q. Zhang, and P. J. Kelly, *Phys. Rev. B* **79**, 174426 (2009).
- [140] J. M. Ziman, *Electrons and phonons* (Clarendon Press, Oxford, 2007).
- [141] I. Žutić, J. Fabian, and S. Das Sarma, *Phys. Rev. Lett.* **88**, 066603 (2002).
- [142] J. Fabian, I. Žutić, and S. Das Sarma, *Phys. Rev. B* **66**, 165301 (2002).
- [143] I. Žutić, J. Fabian, and S. Das Sarma, *Appl. Phys. Lett.* **82**, 221 (2003).
- [144] P. C. van Son, H. van Kempen, and P. Wyder, *Phys. Rev. Lett.* **58**, 2271 (1987).
- [145] T. Valet and A. Fert, *Phys. Rev. B* **48**, 7099 (1993).
- [146] M. Hatami, G. E. W. Bauer, S. Takahashi, and S. Maekawa, *Solid State Commun.* **150**, 480 (2010).
- [147] A. Fert and H. Jaffrès, *Phys. Rev. B* **64**, 184420 (2001).

- [148] G. Schmidt, D. Ferrand, L. W. Molenkamp, A. T. Filip, and B. J. van Wees, Phys. Rev. B **62**, R4790 (2000).
- [149] E. I. Rashba, Phys. Rev. B **62**, R16267 (2000).
- [150] R. Jansen, A. M. Deac, H. Saito, and S. Yuasa, Phys. Rev. B **85**, 094401 (2012).
- [151] R. H. Silsbee, Bull. Magn. Reson. **2**, 284 (1980).
- [152] S. M. Badalyan and F. M. Peeters, Phys. Rev. B **64**, 155303 (2001).
- [153] J. Wang, X. Chen, B.-F. Zhu, and S.-C. Zhang, Phys. Rev. B **85**, 235131 (2012).
- [154] L. D. Landau and E. M. Lifshitz, *Statistical Physics (3rd Edition Part 1)* (Butterworth-Heinemann, Oxford, 1999).
- [155] M. V. Cheremisin, ArXiv e-prints (2011), 1110.5778.

Acknowledgments

I am extremely grateful to Jaroslav Fabian and Alex Matos-Abiague for their guidance and advice during the past few years. For their support, which has proven to be invaluable in every research project I have ever worked on, I owe a great deal of debt to them. If it were not for them, I am sure that I could have never put anything down on paper for this thesis. Special thanks are also due to Vasili Perebeinos and Igor Žutić for their hospitality when I was visiting them at Yorktown Heights and Buffalo, respectively. During my stay there, I had the chance to learn quite a lot from them, not only about electron-phonon coupling or electrical spin injection.

Of course, I have to extend my gratitude to the other members of Prof. Fabian's group: Sebastian Putz, Martin Raith, our former colleague Sergej Konschuh, Martin Gmitra, Denis Kochan, Carlos Lopez-Monis, Florian Hummel, and Christopher Eltschka as well as the former members Samvel Badalyan, Fabio Baruffa, and Christian Ertler. Not only were they excellent contact persons for any problem concerning physics, but they really made me enjoy my time in Prof. Fabian's group.

For proofreading major parts of this thesis and suggesting various improvements, both in substance and expression, I would also like to thank Jaroslav Fabian, Alex Matos-Abiague, and Florian Hummel. Any remaining errors are, of course, my own.

I am also very thankful to Angela Reißer, Ulla Franzke, and Claudia Rahm, who shouldered almost all of the bureaucratic burdens I faced during my PhD studies.

Finally, I gladly acknowledge the DFG, which provided financial support via GRK 638, GRK 1570, and SFB 689.

Curriculum Vitae

Personal Data

Name	Benedikt Scharf
Date of birth	10.11.1982
Place of birth	Oberviechtach
Nationality	German

Positions

2009-	Universität Regensburg Research and Teaching Assistant
-------	--

Education

1989-1993	Volksschule Schwarzhofen
1993-2002	Ortenburg-Gymnasium Oberviechtach
06/2002	Abitur

2003-2008	Universität Regensburg
11/2008	Diploma in Physics <ul style="list-style-type: none">• Thesis title: Charge and Spin Current Relaxation Times in Disordered Conductors and Collective Modes in Conducting Nanotubes• Thesis advisor: Jaroslav Fabian

2009-	Universität Regensburg Postgraduate Studies in Physics
-------	--

Alternative Civilian Service

2002-2003	Marienheim Neunburg vorm Wald
-----------	-------------------------------

List of Publications

- [1] B. Scharf, J. Fabian, and A. Matos-Abiague, *Theory of pseudospin excitations in coaxial nanotubes*, Phys. Rev. B 81, 125428 (2010)
- [2] B. Scharf, A. Matos-Abiague, I. Žutić, and J. Fabian, *Theory of thermal spin-charge coupling in electronic systems*, Phys. Rev. B 85, 085208 (2012)
- [3] B. Scharf, A. Matos-Abiague, and J. Fabian, *Magnetic properties of HgTe quantum wells*, Phys. Rev. B 86, 075418 (2012)
- [4] B. Scharf and A. Matos-Abiague, *Coulomb drag between massless and massive fermions*, Phys. Rev. B 86, 115425 (2012)